PIEZOELECTRIC VIBRATIONAL ENERGY HARVESTERS: DESIGNS, LIMITS, AND APPLICATIONS TO AVIAN BIO-LOGGING

A Dissertation

Presented to the Faculty of the Graduate School

of Cornell University

in Partial Fulfillment of the Requirements for the Degree of

Doctor of Philosophy

by

Michael William Shafer

August 2013

PIEZOELECTRIC VIBRATIONAL ENERGY HARVESTERS:
DESIGNS, LIMITS, AND APPLICATIONS TO AVIAN BIO-LOGGING

Michael William Shafer, Ph.D.
Cornell University 2013

Discrete animal-mounted sensors and tags have a wide range of potential applications for researching wild animals and their environments. These "bio-loggers" could be used to monitor the animal's location, metabolic output, or used as environmental monitoring sentinels. Such applications are made possible by recent decreases in the size, mass, and power consumption of modern microelectronics. Despite these performance increases, bio-logging systems need to generate power in-situ for extended deployments, and piezoelectric vibrational energy harvesters are a potential power source. In the past these devices have not been generally characterized, resulting in a lack of clarity as to their capabilities.

In this dissertation, the design and limits of piezoelectric energy harvesting devices are explored. Given a set of design goals, these devices require careful consideration of the piezoelectric element thickness in order to maximize power output. Additionally, harvested power can be related to the material strength, providing a limit for the technology that spans device mass and the frequency of the harvested vibration. As efficiency is an important parameter for any device harvesting energy from an animal, this work explores how it is defined for these devices, proposes an alternative definition, and shows how conventional definitions can over predict efficiency.

With an understanding of the capabilities of piezoelectric energy harvesting,

the case for its viability as a power source for avian bio-logging applications is then presented. A method of estimating the harvestable energy available from a variety of bird species is shown to predict sufficient power available for the electronics typically used in bio-loggers. These results led to testing of piezoelectric devices on pigeons in flight. The results of the pigeon flight experiments show significant power production, with respect to bio-logger power requirements, and limited effects on the acceleration of the bird.

BIOGRAPHICAL SKETCH

Michael William Shafer was born in Takoma Park, Maryland in 1983 to Michael Stephen and Margaret Rosaria. His family settled in Tucson, Arizona in 1990, where he spent the majority of his childhood. In 2001, he graduated from Canyon del Oro High School, earned his Eagle Scout award, started his undergraduate career at Northern Arizona University (NAU), and fell in love with his future wife, Kristin. Majoring in mechanical engineering at NAU, Michael was active in the department working as a research assistant for various professors and participating as an ambassador for the college of engineering.

In 2004, Michael took a semester off from NAU to work as a co-op at NASA's Jet Propulsion Laboratory (JPL) in Pasadena, California. There he worked on various proposals and designs for the Mars Science Laboratory rover. After returning to NAU for one more year, he spent another summer at JPL developing test equipment for Mars Science Laboratory. In his final year at NAU, Michael participated in the SAE Aerodesign Competition as his senior design project, helping to design and build a large R/C aircraft. After marrying Kristin and graduating from NAU in 2006, Michael accepted a job at JPL as a cognizant engineer.

At JPL, Michael designed and coordinated the development, testing, and assembly of hardware used during the landing of the Mars Science Laboratory rover (Curiosity) in 2012. His hardware acted as the connection for the rover to the vehicle that placed it on the surface of Mars. While at JPL, Michael spent many long weekends backpacking the Sierra Nevada mountain range. After the integration of his hardware in the spacecraft in 2009, Michael spent three weeks hiking the John Muir Trail with his wife, and then left California for graduate school at Cornell University in Ithaca, New York.

As a graduate student of mechanical engineering at Cornell, Michael focused on dynamics and controls, working under the advisement of Professor Ephrahim Garcia. In 2010, he began his work on the avian piezoelectric energy harvesting concept that would become this dissertation. Also in 2010, he and his wife also had their first son, Michael Casey. In 2011, Michael received a graduate research fellowship from the National Science Foundation. In 2013, he and his wife had their second son, William Agassiz.

This dissertation is dedicated to my family, especially my wife, whose unyielding love and support is my foundation.

ACKNOWLEDGEMENTS

I would first like to acknowledge my wife Kristin, who has given me everything from two beautiful children, to unwavering support in all my endeavors. I would also like to acknowledge my parents, for everything they've done and continue to do for me. They are forever my role models. Professor Garcia has been more than an advisor throughout my graduate program. As needed, he has been my mentor, my critic, and my friend. I learned a lot from him over coffee about engineering, philosophy, family, and food. I would like to thank Robert MacCurdy and Matthew Byrant who often served as sounding boards for many of the ideas in this dissertation. Rob also served an extensive role in the development of the electronics for the bird flight tests. His contributions were invaluable. Finally, I would like to acknowledge the National Science Foundation and its Graduate Research Fellowship Program, which funded me through the majority of my graduate studies. This material is based upon work supported by the National Science Foundation Graduate Research Fellowship Program under Grant No. DGE0707428 and NSF grant No. CMMI- 1014891.

TABLE OF CONTENTS

LIST OF TABLES

LIST OF FIGURES

CHAPTER 1

DESIGNING MAXIMUM POWER OUTPUT INTO PIEZOELECTRIC ENERGY HARVESTERS [1]

1.1 Introduction

Piezoelectric energy harvesters have become the subject of much research over the last decade, yet fundamental questions remain concerning their design and performance. In this work, we present a method of system design that meets requirements such as mass, volume, and frequency limitations, while simultaneously maximizing the harvested power output. Specifically, we will arrive at a method for determining the ideal thickness ratio for fully covered bimorph piezoelectric energy harvesters. Finally, we apply our power maximization design method to an example case, and demonstrate improvements in power and the required amount of piezoelectric material when compared to an alternate method [88].

Typical piezoelectric vibrational energy harvesters use the first resonant frequency of a beam to induce large strains, which are converted to electric charge by way of the piezoelectric electromechanical coupling. Such a system can be seen in figure 1.1. The system consists of a substrate laminated with piezoelectric material. A tip mass is typically added to affect the resonant frequency and increase root strain. While the length and mass of the beam may be limited by design requirements, the thicknesses of the piezoelectric material and the substrate need to be specified such that power is maximized. Additionally,

[1] This chapter was originally published as an article in *Smart Materials and Structures* [74]. Reproduced here with permission.

the beam's first resonant frequency needs to match that of the harmonic base motion, such that vibration amplitude is maximized. This work focuses on a method of determining the beam parameters in terms of the ratio of piezoelectric thickness to total beam thickness; Section 1.3 presents a method of selecting the thickness ratio which maximizes power.

A large amount of effort has been placed on optimization of resistive loads [12, 34] and switching techniques [25, 81, 39, 89]. As we are interested in the mechanical design, and a wide variety of beam designs must be considered, we require a power model that is widely valid and applicable. As such, we consider the standard rectifier circuit shown in figure 1.2. Here the piezoelectric source is modeled as a current source in parallel with a capacitor. Given the proper filtering capacitor (C_f) value, this circuit provides a nearly constant output voltage which is dissipated across the resistive load.

While many papers have focused on power increases through circuit design, the mechanical design optimization has languished. Some studies have investigated optimization of patch size and placement for piezoelectric materials used in actuators [43, 18]. The results cannot be directly applied to energy harvesters because the work focused on maximizing output moment and no harvesting circuit dynamics are considered. Dietl and Garcia investigated the optimized

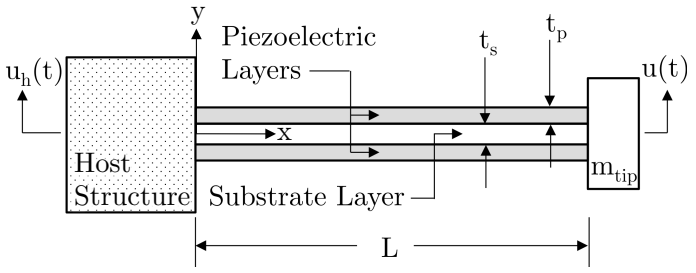

Figure 1.1: Typical layout of fully laminated piezoelectric energy harvester with base excitation.

width profile of a fully covered piezoelectric harvester and found power increases for a fixed total mass are expected if the beam is properly designed [17]. Yoon et al. modeled curved unimorphs for energy harvesting, but investigated impact loading rather than harmonic vibration [91]. While the paper presented a general "rule of thumb," no explicit procedure for optimization was presented. Rupp et al. developed a computational method for piezoelectric and substrate layout optimization for a wide variety of problems [72]. In their paper, they show that the thickness ratio affects the ideal distribution of piezoelectric material over the surface of a square substrate, but their numerical approach makes development of general results or analytical design guidelines difficult.

A number of works have investigated maximizing the harvester's electromechanical coupling coefficient. Cho et al. found a thickness ratio that maximized the coupling coefficient of a unimorph membrane harvester [14]. Similar work has been done for unimorphs under impact loading, across a wide range of piezoelectric to substrate stiffness ratios [68]. More recently, Wickenheiser developed an analytic solution for the thickness ratio which maximizes coupling coefficient of a harmonically excited beam [88]. This solution though, requires modal mass to be held constant. None of these provide a method for thickness ratio optimization while holding the system mass constant. Moreover, general guidelines for proper energy harvester beam design do not exist. Often, a beam

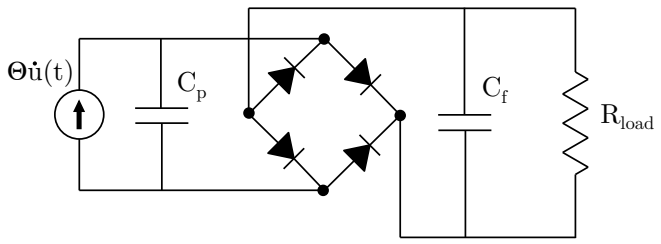

Figure 1.2: Circuit diagram for the standard piezoelectric harvester signal rectification and dissipation.

is fabricated and tip mass added until the system is tuned to a given natural frequency. Other times, numerical methods are used to optimize beam parameters for a given set of constraints [71, chap. 4.6], and as such, the results are limited to a specific design. These methods of design are neither mass, nor cost efficient. What is needed is a design method that is capable of creating the correct system parameters given specific system requirements.

Here we develop a method for the design of a piezoelectric bimorph energy harvester. Given an allowable system mass, material properties, a target natural frequency, and a beam size limitation, our method finds the required total beam thickness, tip mass, and piezoelectric/total beam thickness ratio. The required variables are all parameters that would be known on the outset of a design process. Not only does this method reduce the need for design iteration, but it provides a thickness of piezoelectric material that maximizes power generation.

Our technique uses composite beam analysis, along with approximations for beam natural frequency and mode shape, to develop expressions for all terms necessary for the prediction of harvester power output. These expressions are put in terms of the fixed system level variables (mass, frequency, length, etc.) and the two unknown variables, thickness ratio and mechanical damping. While the resulting power expression is not solvable for thickness ratio, it does allow for a simple sweep of the variable. The resulting power vs. thickness ratio curve contains a clear maximum, and thus a determination of the proper thickness ratio. Using the first mode shape and natural frequency approximations allows for a closed form solution for various modal beam parameters, and only biases the predicted natural frequency on the order of 0.1%.

1.2 Beam parameter derivation for targeted natural frequency

There are two major cases that must be considered when developing the dimensions of a harvester to match a specific resonant frequency. We first consider the case when the piezoelectric material can take on any thickness between zero and some upper bound. This would be the case if, for example, a material lot was being specifically manufactured for a given design. We then consider the more practical case when there are discrete values for piezoelectric material thickness, as would be specified by a material vendor. In the first case, we fix width and allow for changes in total beam thickness. In the second case, we fix piezoelectric material thickness and allow for changes in substrate thickness and beam width. The known and unknown variables that are needed to define the system for these cases are summarized in table 1.1. The unknown variables are given in approximate order of calculation and thus this table serves as a basic roadmap for harvester system design. In Sections 1.2.2 and 1.2.3, we develop equations for these dependent variables in terms of the fixed variables and the thickness ratio κ_p. For both cases, we must first develop an equation for natural frequency in terms of the variables under investigation.

Table 1.1: Known and unknown beam parameters for the design scenarios of continuous and discrete piezoelectric thickness

Continuous Piezoelectric Thickness			Discrete Piezoelectric Thickness		
Known	Unknown	(Eqn No.)	Known	Unknown	(Eqn No.)
resonant frequency	thickness ratio	sweep of (1.22)	resonant frequency	thickness ratio	sweep of (1.22)
system total mass	total beam thickness	(1.12)	system total mass	beam width	(1.13)
beam length	piezoelectric thickness	(1.4)	beam length	substrate thickness	(1.4 and 1.5)
beam width	substrate thickness	(1.5)	piezoelectric thickness	tip mass	(1.7b)
material properties	tip mass	(1.7b)	material properties		

1.2.1 First Mode Frequency Equation

In both the continuous and discrete piezoelectric thickness cases, we define four major system level parameters that would likely be known to an engineer designing an energy harvesting system. We assumed the following parameters are predetermined: maximum system mass (M_{sys}), beam length (L), the material properties for piezoelectric and substrate, and depending on the case, the beam width (w) or the piezoelectric material thickness (t_p). In either case, we must determine the unknown parameter (total beam thickness or width), in terms of thickness ratio, necessary to develop the specified resonance. We begin with a closed form approximation for the first natural frequency (in rad/s) of a homogenous beam [10].

$$\omega_1 = \sqrt{\frac{3EI}{L^3(m_t + 0.24m_b)}} \tag{1.1}$$

Here m_t, E, I,L, and m_b are the tip mass, beam modulus of elasticity, moment of inertia, length, and mass, respectively. We denote the frequency here as ω_1 to distinguish it from the natural frequency calculated later from modal parameters (ω_n). As this equation deals solely with the mechanical dynamics, it predicts the short circuit natural frequency of the beam where no charge accumulates on the piezoelectric portion of the beam. It is based on a curve fit of the exact solution for the first mode of vibration across a wide range of tip mass ratios (m_t/m_b). Figure 1.3 shows the error in the fundamental frequency prediction as a function of mass ratio. In this figure we can see that the maximum error magnitude occurs for a beam with no tip mass, but is only -0.559%. Above mass ratios of about 0.5, the error remains less than 0.15%. These small error values validate the use of this approximation for the natural frequency over all values of mass ratio.

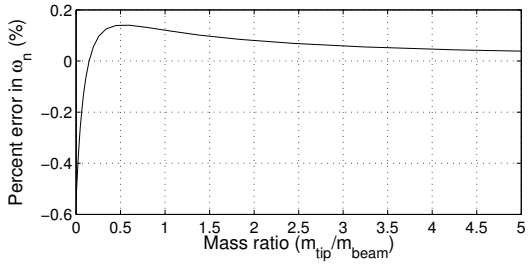

Figure 1.3: Error in first natural frequency as a function of mass ratio comparing approximate solution to modal solution using first five modes. Note that largest error occurs for no tip mass.

Note that equation (1.1) is shown in a form for a simple prismatic, homogenous beam. But because we have a composite beam, we must derive the equation for the effective moment of inertia of the composite beam given the piezoelectric material modulus relative to that of the substrate. To do so, we make the following definitions:

$$\eta \equiv \frac{E_p}{E_s} \tag{1.2}$$

$$\kappa_p \equiv \frac{2t_p}{t} \tag{1.3}$$

Here, η is the ratio of Young's modulus along the beam axial direction and κ_p is the piezoelectric material thickness ratio. In these definitions, E_p and E_s are the piezoelectric and substrate moduli. The modulus E_p depends on the orientation of the piezoelectric layer. For typical beams which use the d_{31} coupling mode, E_p corresponds to c_{11}^E for the piezoelectric material. We ignore the contribution to stiffness provided by the bonding medium used to adhere the layers of the beam. These bonding layers are assumed to be thin and have relatively low modulus relative to the other layers of the beam. The term t is the total beam thickness and t_p is the thickness of an individual piezoelectric layer, of which two exist on the beam. Given the definition for thickness ratio, we can define the substrate thickness (t_s) and total beam thickness (t) in terms of the thickness

ratio and piezoelectric thickness.

$$t = \frac{2t_p}{\kappa_p} \tag{1.4}$$

$$t_s = t - 2t_p = t(1 - \kappa_p) \tag{1.5}$$

With these definitions we can determine an effective moment of inertia for the composite beam given the modulus ratio η, as would be done in any elementary mechanics of materials text (see for instance [9, p. 230-233]). This effective moment of inertia can be substituted in for I in equation (1.1), and can be expressed as follows.

$$I_{eff} = \frac{wt^3}{12}\hat{I}_{eff} \tag{1.6a}$$

$$\hat{I}_{eff} = (\eta - 1)\kappa_p^3 - 3(\eta - 1)\kappa_p^2 + 3(\eta - 1)\kappa_p + 1 \tag{1.6b}$$

Equation (1.6), gives an effective moment of inertia for a beam fully comprised of the substrate material, but with the same stiffness as our composite beam. It thus allows, with the use of E_s, the direct use of equation (1.1) to predict the fundamental frequency of our composite beam. Here in equation (1.6), w is the beam width and $\hat{I}_{eff}$ is the non-dimensional composite inertia scaling factor. Notice that I_{eff} collapses to $wt^3/12$, the common equation for rectangular moment of inertia, when the piezoelectric stiffness equals that of the substrate. Now that we have an expression for the effective moment of inertia, we could solve for total beam thickness if both the tip mass and beam mass were known. But as previously mentioned, an engineer is likely to have a system level mass requirement, M_{sys}. As such, the mass terms of the denominator within the radical in equation (1.1) should be put in terms of the known variables (density,

length, width, thickness, system mass), and the unknown thickness ratio, κ_p.

$$M_{sys} = m_t + m_b \tag{1.7a}$$

$$m_t = M_{sys} - m_b \tag{1.7b}$$

Substituting equation (1.7b) into the denominator of equation (1.1) gives:

$$m_t + 0.24m_b = M_{sys} - 0.76m_b \tag{1.8}$$

and given that:

$$m_b = Lw(2t_p\rho_p + t_s\rho_s) = Lwt[\kappa_p\rho_p + (1-\kappa_p)\rho_s] \tag{1.9}$$

The denominator thus becomes:

$$(m_t + 0.24m_b) = M_{sys} - 0.76Lwt[\kappa_p\rho_p + (1-\kappa_p)\rho_s] \tag{1.10}$$

Substituting equations (1.6) and (1.10) into equation (1.1) results in:

$$\omega_1 = \sqrt{\frac{E_s w t^3(\eta-1)\kappa_p^3 - 3(\eta-1)\kappa_p^2 + 3(\eta-1)\kappa_p + 1]}{4L^3(M_{sys} - 0.76Lwt[\kappa_p\rho_p + (1-\kappa_p)\rho_s])}} \tag{1.11}$$

This equation for the short circuit fundamental frequency of a piezoelectric energy harvesting beam can then be solved for the unknown parameters of the system. For continuously available piezoelectric thicknesses, this is total beam thickness. For piezoelectric material available only in discrete thicknesses, the unknown beam parameter is width.

1.2.2 Continuous Piezoelectric Material Thickness

Recalling the fixed and dependent variables for the continuous piezoelectric material thickness case of table 1.1, we need here to find the thickness of the

beam in terms of the fixed parameters. Using equation (1.11), the total beam thickness can be solved for in terms of the natural frequency and other beam parameters. In this case, where piezoelectric material thickness is variable, we fix the beam width and solve for the overall beam thickness. The fixed and dependent variables for this case are summarized in table 1.1. As equation (1.11) is cubic in t, there are three solutions, only one of which is real. The resulting equation for the total beam thickness is:

$$t = \mu^{\frac{1}{3}} - \frac{\lambda}{3\,\gamma\,\mu^{\frac{1}{3}}} \tag{1.12}$$

where

$$\begin{aligned}
\gamma =& 25\,\mathrm{E_s}\,w + 75\,\mathrm{E_s}\,{\kappa_\mathrm{p}}^2\,w - 25\,\mathrm{E_s}\,{\kappa_\mathrm{p}}^3\,w - 75\,\mathrm{E_s}\,\kappa_\mathrm{p}\,w \ldots \\
&+ 75\,\mathrm{E_s}\,\kappa_\mathrm{p}\,\eta\,w - 75\,\mathrm{E_s}\,{\kappa_\mathrm{p}}^2\,\eta\,w + 25\,\mathrm{E_s}\,{\kappa_\mathrm{p}}^3\,\eta\,w \\
\lambda =& 76\,L^4\,\rho_\mathrm{s}\,w\,{\omega_1}^2 + 76\,L^4\,\kappa_\mathrm{p}\,\rho_\mathrm{p}\,w\,{\omega_1}^2 - 76\,L^4\,\kappa_\mathrm{p}\,\rho_\mathrm{s}\,w\,{\omega_1}^2 \\
\mu =& \left(\sqrt{\frac{\lambda^3}{27\,\gamma^3} + \frac{2500\,L^6\,M_{sys}^2\,{\omega_1}^4}{\gamma^2}} + \frac{50\,L^3\,M_{sys}\,{\omega_1}^2}{\gamma} \right)
\end{aligned}$$

Equation (1.12) provides a way of designing a beam, given a set of constraints on the beam planform, mass, and material properties.

1.2.3 Fixed Piezoelectric Material Thickness

In the case when the piezoelectric material must be selected from a discrete set of values, it too must be added to the list of fixed variables. In the previous case we fixed beam length, width, mass, material properties, thickness ratio, and solved for the necessary overall beam thickness. In fixing piezoelectric material thickness, we add an additional constraint to this system and in doing so, must

release a different parameter. Here we allow the beam width to change as a function of the aforementioned variables. The fixed and dependent variables for this case are summarized in table 1.1. Once again, we base the solution on equation (1.11). Here we substitute the total beam thickness, $t = 2t_p/\kappa_p$, as predetermined from equation (1.4) into equation (1.11) and solve for the beam width.

$$w = \frac{L^3 M_{sys} \kappa_p^3 \omega_1^2}{2t_p \left(\frac{19}{25} L^4 k_p^2 \omega_1^2 (\kappa_p \rho_p + \rho_s (1 - \kappa_p)) + \hat{I}_{eff} E_s t_p^2 \right)} \tag{1.13}$$

With equation 1.3 and 1.13, the beam is now fully defined in terms of mass, material properties, length, and thickness ratio. Although the width is specified here, if the system mass or length are not sized properly, the results of this equation may be a beam which is wider than it is long. Because the natural frequency equation, on which equation (1.13) is based, applies to only Euler-Bernoulli beams, we must ensure that the resulting beam is sufficiently long with respect to its width and thickness. As such, the dimensions of the designs produced via this method should be checked prior to fabrication. Occasionally, depending on the thickness of piezoelectric material available and the targeted natural frequency and mass, a sub-optimal design may have to be selected to ensure that the fabricated beam can still be considered Euler-Bernoulli.

1.3 Designing for peak power

Section 1.2 provides a method for determining the unknown beam variables in terms of fixed variables and the thickness ratio, κ_p. These beam parameters can now be used to determine the power from the harvester, in terms of thickness ratio. A wide variety of power models exist for piezoelectric harvesters ranging

in complexity and fidelity. Erturk and Inman present a range of known problems with specific power models, and discuss the importance of including the electrical coupling in the mechanical domain [21]. As such, we focus on power models that include this "backward coupling."

Both Guyomar et al. [25] and Lefeuvre et al. [39] present a power model based on a single mode approximation for a harvester attached to a rectifier circuit with a filtering capacitor. Using the assumption that the tip mass velocity and the forcing function are in-phase, Guyomar et al. presents a model for the optimum resistance and maximum power for a system where electromechanical coupling is weak [25]. Lefeuvre et al. finds the optimum resistance and maximum power for a system with strong electromechanical coupling, while still making the in-phase assumption [39]. Shu and Lien show that this in-phase assumption may not be accurate for beams with high coupling, as the coupling can induce phase shifts between velocity and excitation force [81]. They present an alternate method, while maintaining the single mode approximation, for the determination of the ideal resistance and power. This less restrictive model is what we use to predict power developed in the harvester. Although Shu and Lien suggest that the non-dimenstional power ($\bar{P}$) can be used to optimize the dimensions of the beam, this inherently requires that modal mass be held constant; Modal mass depends on the beam dimensions. Since we are interested in the more general case where system mass is constant, we must use the dimensionalized power equation.

While the majority of the derivation of the model can be found in the reference, we re-define terms here for use in this work. We begin with the governing

equations for a piezoelectric harvester [26, 83, 81, 19].

$$M\ddot{u}(t) + C\,\dot{u}(t) + K\,u(t) - \Theta V(t) = F(t) \tag{1.14}$$

$$-\Theta\dot{u}(t) + C_p\,\dot{V}(t) = -I(t) \tag{1.15}$$

where M, C, K, and Θ are the modal mass, damping, stiffnesses, and piezoelectric coefficients, respectively and C_p is the piezoelectric capacitance. The distance along the beam is x, with the root being defined as the origin (see figure 1.1). External forces and currents are included as F and I. In the first mode approximation, these parameters are defined as:

$$M_* = \int_{v_*} \rho_* \phi(x)^2 \,\mathrm{d}v_* \tag{1.16}$$

$$K_* = \int_{v_*} y^2 E_* \phi''(x)^2 \,\mathrm{d}v_* \tag{1.17}$$

$$\Theta_* = -\int_{v_p} y\,\phi''\,e\,\psi(y)\,\mathrm{d}v_p \tag{1.18}$$

$$C_{p*} = \int_{v_p} \epsilon^s\,\psi(y)^2\,\mathrm{d}v_p \tag{1.19}$$

Here ρ, v, and y are the density, volume, and distance from the neutral axis for the portion of the beam for which the parameter is being calculated, respectively. Additionally, e and ϵ^s are the piezoelectric stress and permittivity constants. The variable $\phi(x)$ is the mode shape of the first mode of vibration, and $\psi(y)$ defines the electric field over the piezoelectric thickness [83]. The "$_*$" indicates a that the parameter is computed for a specific portion of the beam, either piezoelectric, substrate, or tip mass. For example, a beam may have two layers of piezoelectric material whose modal mass terms would be M_{p1} and M_{p2}. Note that Θ and C_p for non-piezoelectric materials are taken to be zero. For beams of multiple materials, the total modal terms (M,K,Θ,C_p) are simply the sum of the individual modal terms (M_*,K_*,Θ_*,C_{p*}).

The above modal parameters depend on the mode shape of the fundamental

mode of vibration. Because this shape depends on the ratio of the tip mass to that of the beam, and we are interested in an analytic solution to this problem which circumvents the transcendental nature of the modal solution, we use an approximate solution for the mode shape [10], modified here such that L is the beam length and $x = 0$ corresponds to the root of the beam and the tip magnitude is that of unity.

$$\phi(x) = \frac{(L-x)^3}{2L^3} - \frac{3(L-x)}{2L} + 1 \tag{1.20a}$$

$$\phi'(x) = -\frac{3(L-x)^2}{2L^3} + \frac{3}{2L} \tag{1.20b}$$

$$\phi''(x) = \frac{3(L-x)}{L^3} \tag{1.20c}$$

While this is an approximation, as noted by Blevins [10], it is generally within 1% of the exact result. However, because the definitions of the modal mass, stiffness, and piezoelectric coefficient require the integration of the mode shape or curvature (ϕ''), this error source needs to be considered. We have computed this error for the various modal parameters as a function of the ratio of tip mass to beam mass. As is shown in figure 1.4, the mode shape approximation does not contribute to substantial errors in the modal mass, stiffness, nor piezoelectric coefficient when the mass ratio is large. Errors become substantial (greater than 2%) near a mass ratio of unity. Because all of these terms contribute to the power prediction for the harvester, the final mass ratio of a beam designed using this method should be compared to this plot so that the validity of the prediction can be assessed. For this reason, we will restrict our analysis to beams who's mass ratios are greater than unity, a result that is typical for many applications.

Continuing the presentation of the power model, the following non-

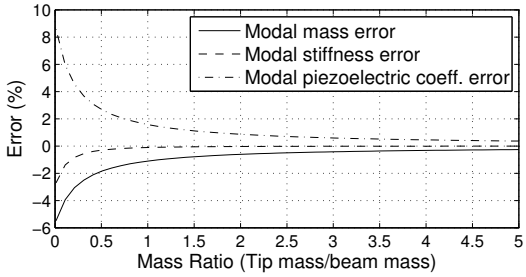

Figure 1.4: Errors in various modal parameters as a result of the use of the Blevins approximation for mode shape of a cantilevered beam with a tip mass.

dimensional parameters are used to fully describe the beam [81].

$$\omega_n = \sqrt{\frac{K}{M}} \qquad k_e^2 = \frac{\Theta^2}{K\,C_p} \qquad \zeta = \frac{C}{2\sqrt{K\,M}}$$

$$\Omega = \frac{\omega}{\omega_n} \qquad r = C_p\,\omega_n\,R \tag{1.21}$$

where, ω_n is the short circuit natural frequency of the harvester, k_e^2 is the non-dimensional coupling coefficient, ζ is the mechanical damping ratio, Ω is the normalized frequency, and r is the normalized resistance. The variable ω is the driving frequency such that when driven at the short circuit frequency, $\Omega = 1$, and when driven at the open circuit resonance, $\Omega = \sqrt{1 + k_e^2}$. For small levels of coupling (when k_e^2/ζ is small), the optimum driving frequency would be at $\omega_{n_{sc}}$. For larger coupling values ($k_e^2 \gtrapprox 8.5$–10) [89] [81], the optimal driving frequencies for maximal power output occur at approximately $\omega_{n_{sc}}$ and $\omega_{n_{oc}}$ [81].

Based on the aforementioned definitions, the power dissipated through the resistive load would be [81]:

$$P = \frac{MA^2}{\omega_n} \frac{1}{\left(r\,\Omega + \frac{\pi}{2}\right)^2} \times \frac{k_e^2\,\Omega^2\,r}{\left(2\zeta + \frac{2k_e^2 r}{\left(r\Omega + \frac{\pi}{2}\right)^2}\right)^2 \Omega^2 + \left(1 - \Omega^2 + \frac{\Omega\,k_e^2 r}{r\Omega + \frac{\pi}{2}}\right)^2} \tag{1.22}$$

The variable A in this equation is the magnitude of base acceleration. When optimizing the beam dimension for maximum power, it is important to note that maximizing the nondimensionalized power, $\bar{P} = P/\left[F_0^2/(\omega_n M)\right]$ [81], will not produce the same optimal parameters as its dimensionalized counterpart, P. This is due to modal mass' dependance on thickness ratio. This dependence requires that modal mass be included in any optimization of thickness ratio or other geometric design parameter of the beam. As such, we use the dimensional form of the power equation here.

Equation (1.22) shows that power is dependent on base acceleration, short circuit natural frequency, modal mass, piezoelectric coupling coefficient, load resistance, mechanical damping, and input driving frequency. In our analysis, we make the following assumptions concerning these parameters.

- The base acceleration is not affected by harvester dynamics.
- The beam designs used have tip mass ratios high enough such that the errors in modal mass, modal stiffness, and coupling coefficient presented in figure 1.4, resulting from mode shape approximations are sufficiently low as not to affect the results of the power prediction.
- The tip mass can be taken to be a point mass at the end of the beam.
- Load resistance used is ideal. The derivation for the ideal resistance for uncoupled and highly coupled beams is succinctly presented in other works [81] and summarized here in equation (1.29).

With these assumptions, we can now develop the non-dimensional variables from equation (1.22) as functions of the system level requirements, material properties, thickness ratio, and damping ratio. This is done by substituting the

mode shape approximations (1.20) into equations (1.16–1.19). The resulting expressions can then be substituted into equation (1.22) to provide an algebraic expression for power in terms of the system requirements, material properties, thickness ratio, and damping ratio.

- **Modal Mass, M:** Using equations (1.16) and (1.20a), the modal mass can be derived as:

$$M = M_{sys} - 0.76Ltw\left(\kappa_p \rho_p + (1-\kappa_p)\rho_s\right) \tag{1.23}$$

  Note that the dependence on t can be expressed as a dependence on material properties, short circuit natural frequency, and beam length and width, as defined in equation (1.12).

- **Piezoelectric Coupling Coefficient, k_e^2:** We will now show that piezoelectric coupling coefficient, k_e^2, is independent of all beam properties other than thickness ratio and material properties. Using equations (1.16-1.19), along with the mode shape equations (1.20a-1.20c), we can derive the terms needed for piezoelectric coupling coefficient, k_e^2.

$$\Theta^2 = w^2 t^2 e^2 \left(1 - \frac{\kappa_p}{2}\right)^2 \left(\frac{3}{2L}\right)^2 \tag{1.24}$$

$$C_p = \frac{4\epsilon^s w L}{\kappa_p t} \tag{1.25}$$

$$K = \frac{E_p w t^3}{4L^3}\left(\kappa_p^3 - 3\kappa_p^2 + 3\kappa_p\right) + \frac{E_s w t^3}{4L^3}\left(1-\kappa_p\right)^3 \tag{1.26}$$

  Plugging these terms into the equation for k_e^2 from equation set (1.21) and simplifying results in the following equation for piezoelectric coupling coefficient.

$$k_e^2 = \frac{9e^2}{4\epsilon^s E_s} \times \frac{\kappa_p\left(\frac{\kappa_p}{2} - 1\right)^2}{\eta\left(\kappa_p^3 - 3\kappa_p^2 + 3\kappa_p\right) + \left(1-\kappa_p\right)^3} \tag{1.27}$$

This result shows that the piezoelectric coupling coefficient depends only on the material properties e, η, E_s, E_p, and the thickness ratio, κ_p. These dependancies match the results of Wickenheiser's alternate approach [88].

- **Load Resistance, r:** As assumed, the load resistance is always selected to be the optimum, resulting in a dependance on coupling. For low values of k_e^2, when the in-phase assumption holds, the optimum resistance can be shown to be [25]:

$$r = \frac{\pi}{2\Omega} \tag{1.28}$$

When coupling becomes so large that two distinct resonances appear, the optimum resistances in each case are [81]:

$$r_{sc} \approx \left(\frac{\pi^2}{\sqrt{16+\pi^2}}\right)\frac{1}{\frac{k_e^2}{\zeta}} \tag{1.29a}$$

$$r_{oc} \approx \frac{\sqrt{16+\pi^2}}{4}\frac{\frac{k_e^2}{\zeta}}{1+k_e^2} \tag{1.29b}$$

- **Input Frequency, Ω:** We will assume that the harvester is operated at the ideal input frequency. For both the low coupling beam and the high coupling beam operated at the short circuit natural frequency, this non-dimensionalized frequency is:

$$\Omega = 1 \tag{1.30}$$

Whereas, for a high coupling beam operated at open circuit natural frequency, the non-dimensionalized frequency is:

$$\Omega = \sqrt{1+k_e^2} \tag{1.31}$$

With these assumptions, we can see that the output power depends on the material properties, thickness ratio, mechanical damping, beam length and

width, base acceleration amplitude, and system mass. Substituting these parameters into equation (1.22), taking the derivative with respect to κ_p, setting to zero, and solving for the ideal thickness ratio is not possible due to the complexity of the power equation. Wickenheiser developed the following equation for thickness ratio which maximizes the coupling term k_e^2 [88].

$$(\kappa_p)_{k_e^2 max} = \left[\frac{1}{2}\left(J^{-1/3} + J^{1/3} + 1\right)\right]^{-1} \tag{1.32}$$

$$J = \left(\sqrt{(2\eta - 1)^2 - 1} + 2\eta - 1\right) \tag{1.33}$$

While this equation is convenient in its simplicity, it produces results that only maximize power if modal mass is held constant. But because modal mass and thickness ratio are interrelated, as we have shown in equation (1.23), they cannot be determined independently. This fact requires that the modal mass term of equation (1.22) be included when maximizing power through thickness ratio changes. Later it will be shown that peak power does not necessarily occur at peak coupling coefficient for constant system mass and frequency. This result requires an improved method of thickness ratio optimization.

To truly maximize power output from the beam, we simply sweep the thickness ratio in the power equation (1.22) after substituting the non-dimensional terms. We have derived all terms of this equation in terms of the system level requirement (mass, ω_n, etc.) and thickness ratio. Base acceleration is a constant in the power equation, and therefore will have no effect on the location of the optimum thickness ratio. Additionally, the unknown mechanical damping ratio ζ would need to be estimated, but as we will show, it has little effect on the ideal thickness ratio over its typical range. Material properties would be fixed for a given substrate and piezoelectric material choice. System mass, beam width, and length would be limited by the desired size of the device. Given knowl-

edge of such parameters, determination of the ideal thickness ratio could be calculated through a sweep of the only unknown parameter in equation (1.22): thickness ratio. This design methodology is used in Section 1.4 to show the results for an example set of beam constraints.

1.4 Design case studies

Given the results of Section 1.3, we are able to design many different beams, all of which target a particular short circuit fundamental frequency, and are of the same length and mass. Given that these designs are all "normalized" by these system level parameters, the question then becomes, which of these designs produces the most power? Specifically, we want to know which thickness ratio produces the most power. Determining the ideal thickness ratio analytically may not be practical given the complexity of equation (1.22) (after all variables on which it depends have been fully substituted). A more pragmatic approach is to sweep a range of thickness ratios while holding the other system level parameters constant. We do this for both the continuously variable and fixed piezoelectric thickness cases described in Sections 1.2.2 and 1.2.3. The various parameters that were held constant in this analysis are presented in table 1.2. Along with fixed parameters, we have also presented those parameters that, once thickness ratio is selected, can be uniquely determine. These are listed as *dependent* parameters.

Table 1.2: List of beam constants constraining example beam

	Continuous t_p	Discrete t_p		
	Value	Value	Unit	Name
ω_1	20	20	Hz	Natural Frequency
M_{sys}	0.0139	0.0139	kg	System Mass
L	0.056	0.056	m	Beam Length
t_p	dependent	0.267	mm	Piezoelectric Layer Thickness
w	0.01	dependent	mm	Beam Width
ρ_s	7916.5	7916.5	kg/m^3	Substrate Density
ρ_p	7800	7800	kg/m^3	Piezoelectric Material Density
E_{s11}	212	212	GPa	Substrate Modulus
E_{p11}	67	67	GPa	Piezoelectric Material Modulus
e	-12.73	-12.73	C/m^2	Piezoelectric Stress Constant
ϵ^s	1.593e-08	1.593e-08	C/m^2	Piezoelectric Permittivity
t_s	dependent	dependent	m	Substrate Thickness
m_t	dependen	dependent	kg	Tip Mass
κ_p	variable	variable	()/()	Thickness Ratio
ζ	variable	variable	%	Mechanical Damping

In order to visualize the effects of changes in thickness ratio over a range of mechanical damping ratios, we must normalize for the effects of damping ratio. Here we describe why this normalization is needed. We see in equation (1.22), that the output power depends heavily on mechanical damping ζ. If, for example, the thickness ratio is held constant at 50% and mechanical damping ratio values from 0.1% to 5% are used, the power output of an example beam can be seen in figure 1.5(a). Alternately, if damping ratio is held constant (3.5%), and thickness ratio is allowed to vary, we see changes in output power with a distinct maximum shown in figure 1.5(b). When comparing the scales of figures, 1.5(a) and 1.5(b), it becomes apparent that in order to visualize the peak that results from of thickness ratio optimization in a plot that also includes variable damping ratio, we must normalize the effect of the damping ratio. In order to do this, we first predict power for each combination of thickness ratio and damping ratio. We then individually select the power curve at each damping ratio and normalize it by its maximum. The resulting normalized curves are then recombined to produce a single normalized contour that shows how thickness ratio affects the location for maximum power output. We call the power resulting from this method of normalization, ζ-normalized power. The solid line in the resulting contours is to highlight the peak.

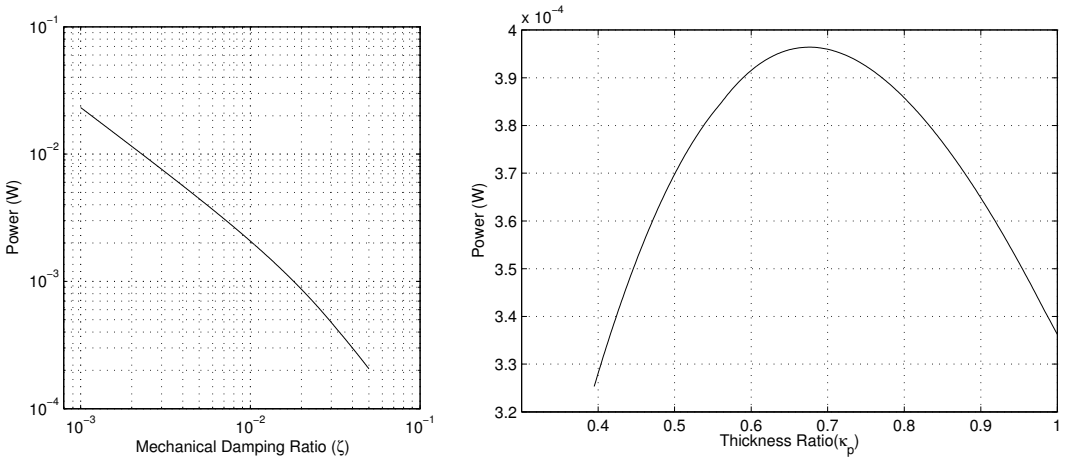

(a) (b)

Figure 1.5: (a)Power versus mechanical damping ratio at 1 m s^{-2} base acceleration. Notice that an order of magnitude drop in damping causes nearly an order of magnitude increase in power. (b) Power versus thickness ratio at 1 m s^{-2} base acceleration with distinct maximum near $\kappa_p = 0.68\%$.

1.4.1 Continuous Piezoelectric Thickness

We first consider beam designs where piezoelectric material thickness is continuously variable. For this case, given the design methodology presented in Section 1.2.2, beam length and width are held constant. We develop beams matching the criteria of table 1.2, while allowing thickness ratio and mechanical damping ratio to vary. To investigate any differences that might occur from ideal resistance changes, for each beam design, the method calculates the power expected when using the low coupling ideal resistance and the high coupling ideal resistance. We look separately at the open and short circuit ideal resistances as different cases in order to investigate any benefit that may occur from choosing one over the other. In either case, the algorithm calculates the powers for each beam design using both the low and high coupling ideal resistances, and selects that which produces more power as the proper resistance for that particular beam. The transition between the use of high and low coupling ideal

resistances can be seen as a dotted line in figures 1.6 and 1.7.

The resulting ζ-normalized power contours (figures 1.6(a) and 1.6(b)) show that peak power and peak coupling occur concurrently for the majority of damping ratios. This is mainly due to the fact that we hold beam width and length constant. As a result, the modal mass is nearly constant across the range of damping ratios. Since a constant modal mass is the assumption used to find the thickness ratio that maximized coupling [88], it is not surprising here that the ideal thickness ratio for power corresponds to the ideal for coupling.

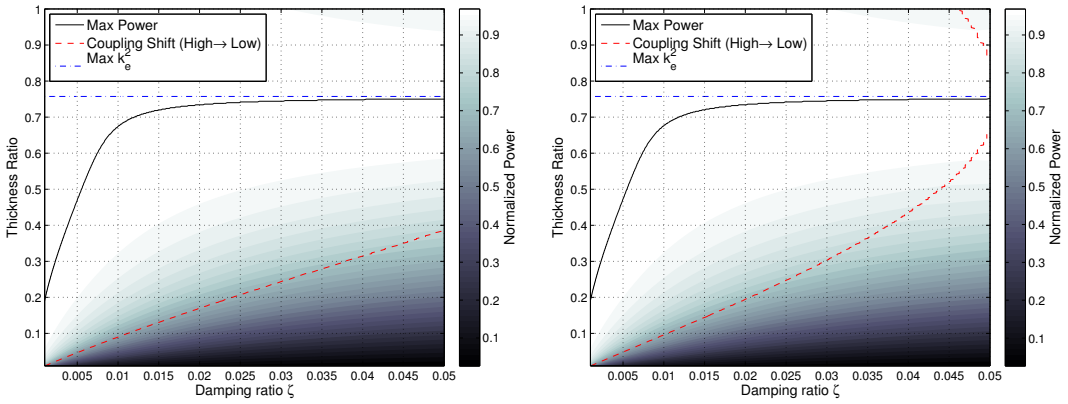

Figure 1.6: Contour plots of ζ-normalized power over a range of thickness ratios and damping ratios for a continuously variable piezoelectric material. The solid black line indicates thickness ratio for maximum power. The dashed line delineates transitions from high to low coupling. (a) Results when short circuit ideal resistance is used when in high coupling region. (b) Results when open circuit ideal resistance is used when in high coupling region.

Figures 1.6(a) and 1.6(b) show that the system is fairly insensitive to changes in thickness ratio for damping ratios greater than approximately 1%. For both cases, in the ranges of typical mechanical damping (0.02 to 0.05), decreasing the thickness ratio by nearly 20% only decreases power by less than 5%. Additionally, in this case of constant beam width and length, piezoelectric material volume is linearly related to thickness ratio. This means that decreasing the

thickness ratio reduces the required volume of piezoelectric material. As such, the device cost could be greatly reduced for a relatively small penalty in power output.

There appears to be very little difference between figures 1.6(a) and 1.6(b), but this is an important fact. While in both plots, the analysis of the low coupling beams is the same, the ideal resistance for the high coupling beams is different. These results show that using the open or short circuit ideal resistance has almost no effect on the ideal beam design, although it can affect the open circuit natural frequency. This is an important result, in that the decision of which resistance to use can be dictated solely based on circuit requirements and electrical considerations, and has little coupling back to the thickness ratio. The only difference that can be seen is between figures 1.6(a) and 1.6(b) is the shift from high to low coupling ideal resistance. These plots show that as damping increases, the transition from high to low coupling is slightly delayed when using the short circuit resistance as compared with the open circuit resistance, for the high coupling cases.

1.4.2 Discrete Piezoelectric Thickness

A more practical case for piezoelectric beam design is to consider beams that must be built when there is not a continuous range of piezoelectric material thicknesses available. When beams matching the discrete t_p criteria of table 1.2 are developed, while allowing thickness ratio and mechanical damping ratio to vary, ζ-normalized power contours (figures 1.7(a) and 1.7(b)) show that peak power and peak coupling do not occur concurrently. Once again in these

contour plots, the dotted line represents the transition in use of the high and low coupling ideal resistances. In these figures we are able to see the effect of changes in thickness ratio over a range of damping ratios. The thickness ratios shown do not extend to zero because, given the constraints of table 1.2, reduced ratios would require beams whose widths are less than 50% of their thickness. These very tall, skinny beams were ignored due to practical concerns of reduced transverse stiffness causing the out of plane fundamental mode to approach the planar mode.

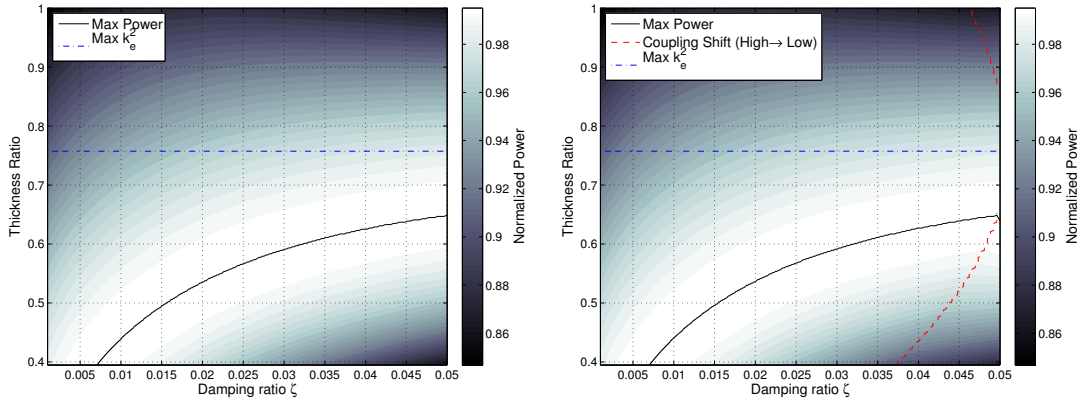

(a) (b)

Figure 1.7: Contour plots of ζ-normalized power over a range of thickness ratios and damping ratios for a fixed piezoelectric material thickness, system mass, and natural frequency. The solid line indicates thickness ratio for maximum power. The dashed line delineates transitions from high to low coupling. (a) Contour plot using short circuit ideal resistance when in high coupling region. (b) Contour plot using open circuit ideal resistance when in high coupling region.

Figure 1.7 shows that at each damping ratio, there is a distinct thickness ratio that produces a maximum power. Moreover, these maximums approach an asymptote as damping ratio increases. The critical fact that can be observed in this figure is that, for normal ranges of mechanical damping ratio ($> 2\%$), there are relatively small changes ($< 10\%$) in the ideal thickness ratio. While a lower mechanical damping ratio will drastically increase power output (as

shown in figure 1.5(a)), figure 1.7 shows that it will not drastically affect the ideal thickness ratio for normal ranges of mechanical damping ($> 2\%$). As such, it is sufficient to make an initial estimate of damping ratio when designing a harvester. This estimate can be used in the power calculations to reduce the problem to a simple search of various κ_p values, rather than a sweep of both κ_p and ζ as was done here.

Also seen in figure 1.7 is a delineation between the used of high and low coupling ideal resistances. The discontinuity in the predicted power across this line should be expected due to the approximate nature [81] of the high coupling resistances. Like the result for the continuous piezoelectric thickness case, these plots show that choosing the ideal high coupling resistance (short or open circuit) can be done with little consideration to beam design, as the ideal thickness ratio in either case is the same.

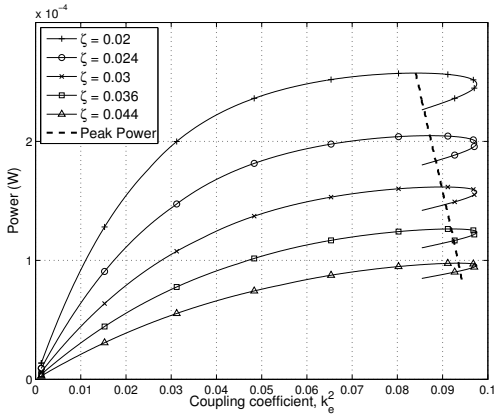

Figure 1.8: Plot of power versus coupling coefficients for mechanical damping ratios from 0.02 to 0.044. Notice that peak power and peak coupling do not coincide. Each curve represents a range of thickness ratios (κ_p) ranging from 0 to 1.

Also plotted in figure 1.7 is the thickness ratio predicted by Wickenheiser's analysis (labeled as Max k_e^2). This prediction is based on the maximization of the

coupling coefficient k_e^2 and as such, is independent of mechanical damping ratio. As noted by Wickenheiser, maximizing k_e^2 maximizes power for constant modal mass. But because modal mass is dependent on thickness ratio, it cannot be considered a constant and left out of the calculations for optimum thickness ratio. We can see in figure 1.8 that when modal mass is included, peak power and peak coupling coefficient do not coincide. This difference results in a prediction of thickness ratio that is higher than that determined by our method. While the thickness ratio provided by maximization of k_e^2 produces power within $\sim 4\%$ of our method (as seen in figure 1.7), the volume of piezoelectric material is significantly increased. If, for example, the beam with the parameters shown in table 1.2 had a damping ratio of 0.035, our method would require 49% less piezoelectric material than would be required using Wickenheiser's maximum k_e^2 method.

Figure 1.9(a) shows the power output, normalized by the power output for the ideal thickness ratio, for a variety of thickness ratios. Note that due to the normalization, all beams of ideal thickness ratio in this plot with have a value of unity. We can see that straying from the ideal can have significant effects on the power output for typical values of damping ratio ($0.02 - 0.05$). This is especially true at higher damping ratios. For example, at $\zeta = 0.05$, both the $\kappa_p = 1$ and $\kappa_p = 0.4$ would produce approximately 13% less power than the ideal thickness ratio beam where $\kappa_p = 0.65$. This plot also shows that the thickness ratio which maximizes coupling coefficient also results in less power than the ideal, although it is within 4% for damping ratios above 0.02. The same is not true for the power per unit volume of piezoelectric material

It is important to remember that the ideal thickness ratios presented in fig-

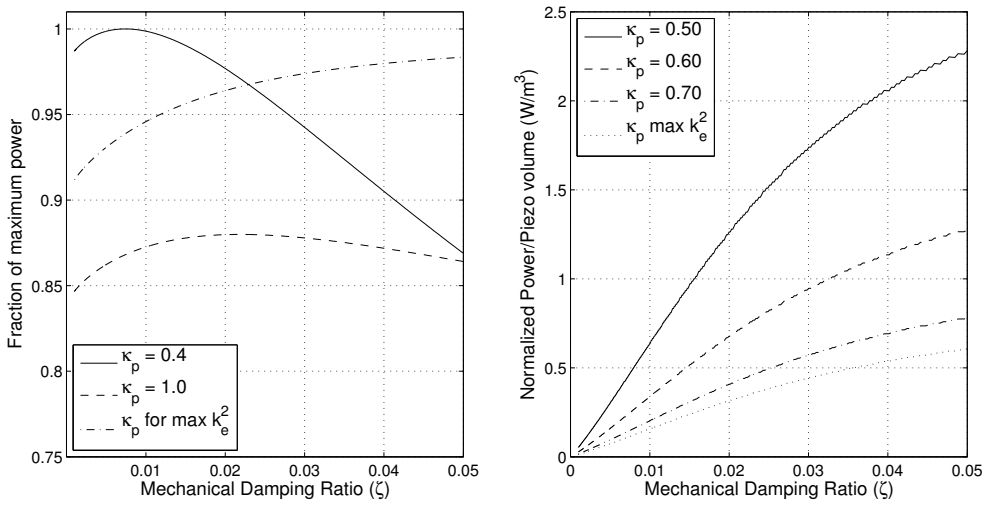

(a) (b)

Figure 1.9: (a) (a) The power output normalized by the power output of a beam using the ideal thickness ratio. Thickness ratios that above $\zeta = 0.2$ represent a shift of approximately $\pm 30\%$ from the ideal thickness ratio are shown. The normalized power output from beams with thickness ratios that maximize the coupling is also shown. (b) Normalized power per unit volume of piezoelectric material for thickness ratios below and above ideal. Note that in both plots, the ideal beam (power output) across the range of damping ratios has a value of unity.

ure 1.7 are those which maximize power, and not power per unit volume of piezoelectric material. If the cost of the device is also a design driver, as it may be during large scale fabrication of harvester beams, then the amount of power produced relative to the volume of piezoelectric material would be critical. Figure 1.9(b) shows the power per unit volume of piezoelectric material for a variety of thickness ratios, all normalized by the value calculated for the ideal thickness ratio. We can see here that as thickness ratio increases, the power per unit volume decreases. The $\kappa_p = 0.60$ curve in this plot shows that beams with thickness ratios less than that which is ideal can sometimes exceed the power per unit piezoelectric volume of the ideal harvester. The $\kappa_p = 0.60$ curve crosses unity, at a $\zeta = 0.32$. This represents the damping ratio where a beam of $\kappa_p = 0.60$

produces maximum power. Above this damping ratio, beams of this thickness ratio would produce more power per unit volume of piezoelectric material, but would do so while producing less total power than a beam designed for maximum power output.

1.5 Conclusions

Prior to this work, the design of piezoelectric energy harvesters subject to base excitation was a problem in multi-objective optimization, requiring maximization of power and minimization of natural frequency error [71]. We reduce this problem to a simple sweep of piezoelectric material thickness ratio. While recent work has been able to show beam designs that maximize the piezoelectric coupling coefficient [88], we provide a way of maximizing power output while holding system mass, not modal mass constant. This is significant because the design requirements almost always have a limit on the physical mass of the system. Requiring that modal mass be held constant results in a design space that varies in physical mass. Our method simultaneously meets desired natural frequency and system mass requirements, while maximizing power output and reducing the amount of piezoelectric material when compared with other methods.

We have shown that the errors as a result of using approximate natural frequency and mode shape equations are small and can be ignored, so long as the tip mass to beam mass ratio is greater than unity. Given system mass, volume, and frequency requirements, we formulate the beam design problem in terms of the only unknown variables: thickness ratio and mechanical damping ratio. We

have shown that the design method is relatively insensitive to errors in mechanical damping ratio estimates, so long as the actual and estimated ratio is above 2%. The remaining unknown parameter in the power equation is thickness ratio (κ_p). Sweeping this parameter through its range of possible values allows for the selection of the ratio which produces peak power. We have shown that using this method, we can produce power above that which would be produced if coupling had been maximized. Additionally, we show significant reductions, on the order of 50%, in the amount of piezoelectric material required to achieve a given amount of power. This method of design simplifies the process of ideal beam design and increases power output while decreasing the required amount of piezoelectric material.

CHAPTER 2

THE POWER AND EFFICIENCY LIMITS OF PIEZOELECTRIC ENERGY HARVESTING [1]

2.1 Introduction

While the field of piezoelectric energy harvesting has become relatively mature in terms of modeling, fundamental questions remain concerning the limits of the technology. Cantilevered resonator type devices are pervasive in the field, yet the power and efficiency limits of these devices have not been explored. This is primarily a result of the complications that arise when relating design parameters to output power. Such complexities have resulted in various concepts on ideal designs for specific applications, but almost no work has been done in understanding the general fundamental limits of the technology. Here we present the limits of efficiency, both at and off resonance, as well as a method for determining the maximum possible power output based on the ultimate strength of the piezoelectric element.

The power limits of energy harvesters were initially theorized by considering a simple piezoelectric stack. Roundy showed that for a stack harvester, the maximum power output would be [70]:

$$P_{max} = \frac{k^2 m A^2}{4\zeta^2 \omega^2} \tag{2.1}$$

Here k is the coupling coefficient, m is the proof mass, A is the base acceleration magnitude, ζ is the mechanical damping ratio, and ω is the natural frequency of the system. This equation serves as a starting point for understanding the

[1] This chapter has been submitted for publication to the *Journal of Vibrations and Acoustics* [76].

available power from a harvester, giving us intuition as to how we might expect acceleration or system natural frequency to affect the power output. But as Roundy correctly notes, stack type piezoelectric harvesters are not practical due to their high resonant frequencies. Additionally, this equation does not provide the detailed insight we need for the cantilevered harvesters typically employed in low force and vibration level environments [7] . Furthermore, this power model is proportional to the square of the acceleration magnitude, A. Because the material would eventually fail if A was sufficiently large, this equation does not inform us as to the absolute power limits of the technology.

Other piezoelectric power models have been proposed that capture, to varying degrees of accuracy, the amount of power that one might capture from a given harvester design [25] [81] [19]. Some studies have investigated piezoelectric actuator design in regards to force/moment output [43, 18]. The results from actuator design optimizations are not directly applicable to energy harvesters, because of the differences in the attached driving or harvesting circuits. Optimized energy harvesting beam planforms have been developed [17], but results are not generalized. Computational and heuristic methods have been used to optimize piezoelectric patch placement and harvester design [91, 71], but they too lack in generality. More recently, Shafer et al. presented a method for developing ideal beam designs based on general system requirements like mass, natural frequency, and length [74, 75]. All of these design methods assume that the base acceleration magnitude is sufficiently low as to not damage the piezoelectric element within the beam. In order to understand the full potential of the technology, the effects of piezoelectric ultimate strength on design must be quantified. In this study we develop expressions for power based on material strength and use the model to predict power capabilities for the technology.

Although many are interested in the maximum possible power output of these devices, efficiency may become an additional driving parameter when harvesting from biological systems. In such cases, the harvesting system could be capable of tiring the host and thus efficiency would become an important parameter. Applications of such energy harvesting abound. Backpacks and shoes have been fitted with smart materials to harvest energy from human ambulation [22] [38] [80]. Other applications include the use of piezoelectrics to harvest energy from moths, beetles, and birds [67] [6] [79]. It is important that the efficiencies of these devices be well understood because of the existing and ever increasing multitude of applications for biologically based energy harvesting [7]. Others have provided an expression for piezoelectric based energy harvester efficiency [82]. We will investigate the results of this expression and show the efficiency limits predicted at resonance. We will also derive an expression for efficiency when the excitation source is incapable of energy recovery. The oscillatory nature of these devices results in energy being transferred back and forth between the harvester and excitation source over each cycle. For many biological systems, the energy transferred back to the excitation source during portions of the cycle cannot be recovered. We will present an alternate expression for efficiency that accounts for the fact that biological systems often cannot recover negative work [42]. The results of this alternate case will be contrasted with the existing expression and we will show the limits of efficiency in both cases.

In this paper we seek to answer the fundamental questions concerning power and efficiency. We will show that the existing expression for energy efficiency for these devices may be misleading for biological excitation sources. We will present a supplementary expression, and present the upper limits for efficiency. Additionally, the maximum possible harvestable power will be de-

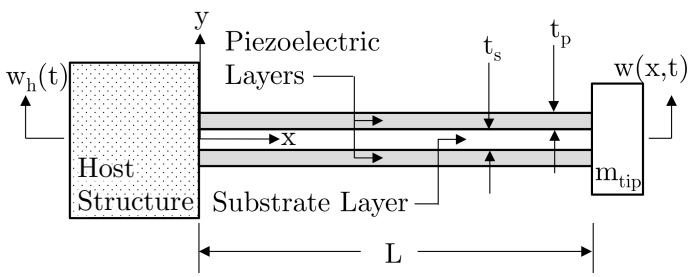

Figure 2.1: Fully laminated bimorph piezoelectric energy harvester.

veloped on the basis of the ultimate strength of the material, in conjunction with existing models of output power. We will develop an expression for the maximum possible power output for a given harvester design, and through the use of design methodologies, present the maximum harvestable power for devices spanning a large range of masses and resonant frequencies.

2.2 The piezoelectric energy harvesting system

In this paper we focus on cantilevered resonator type harvesters under base excitation (Fig. 2.1). These devices consist of a substrate material, laminated on one (unimorph), or both (bimorph) sides with piezoelectric material. A bimorph type device is depicted in figure 2.1. The root of the beam in both cases is considered the local origin of the coordinate system used to describe the geometry and dynamics of the beam. This origin is located vertically by the neutral axis of the beam, as seen in figure 2.1.

The energy harvesting circuit associated with this type of harvester typically consist of a simple resistive load, or a full bridge rectifier with filtering capacitor and resistive load. We consider the latter (see figure 2.2), as a DC source is usually necessary for integration with other circuits. Unlike other circuit con-

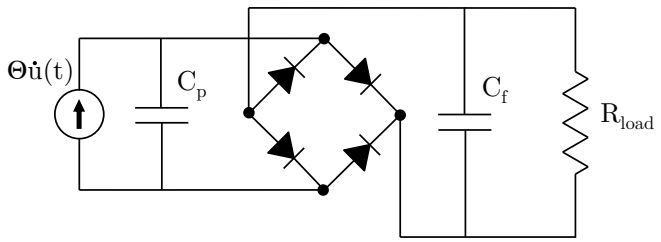

Figure 2.2: Circuit diagram for the standard piezoelectric harvester signal rectification and dissipation.

cepts that have been shown to harvest more power through active switching [25, 39, 89], the rectified-resistive case is more widely adopted and serves as a logical benchmark for comparing current and future concepts.

In order to investigate the capabilities of these devices we begin with the fundamental dynamic equations for these devices [81] [19] [26] [83].

$$M\ddot{u}(t) + C\,\dot{u}(t) + K\,u(t) - \Theta V_p(t) = F(t) \tag{2.2}$$

$$-\Theta\dot{u}(t) + C_p\,\dot{V_p}(t) = -I(t) \tag{2.3}$$

M, C, K, and Θ are the modal mass, damping, stiffness, and piezoelectric coupling coefficients, respectively. C_p is the piezoelectric capacitance. V_p is the voltage over the piezoelectric element. The variable $u(t)$ is the modal displacement in the single mode approximation, where $w(x,t) = u(t)\phi(x)$ and $\phi(x)$ is the mode shape. The variable x is the distance along the beam, with the root being defined as the origin (see figure 2.1). $F(t)$ and $I(t)$ are applied forces and

currents. In the first mode approximation, these parameters are defined as:

$$M_i = \int_{v_i} \rho_i \phi(x)^2 \, \mathrm{d}v_i \tag{2.4}$$

$$K_i = \int_{v_i} y^2 E_i \phi''(x)^2 \, \mathrm{d}v_i \tag{2.5}$$

$$\Theta = -\int_{v_p} y \, \phi'' \, e \, \mathrm{E}_y^f(y) \, \mathrm{d}v_p \tag{2.6}$$

$$C_p = \int_{v_p} \epsilon^s \, \mathrm{E}_y^f(y)^2 \, \mathrm{d}v_p \tag{2.7}$$

In these equations, the "$_i$" indicates the parameter is computed for a specific portion of the beam: piezoelectric, substrate, or tip mass. The total parameter would then be the sum of the individual contributions from each portion of the beam. Variables e and ϵ^s are the piezoelectric stress and permittivity constants. The ρ, v, and y terms are the density, volume, and distance from the neutral axis, respectively. We distinguish electric field $\mathrm{E}_y^f(y)$ though the piezoelectric material from the material elastic modulus E_*.

These terms can be combined to develop the following nondimensional parameters useful in describing and modeling these devices [81]:

$$\omega_n = \sqrt{\frac{K}{M}} \qquad k_e^2 = \frac{\Theta^2}{K \, C_p} \qquad \zeta = \frac{C}{2\sqrt{K \, M}}$$

$$\Omega = \frac{\omega}{\omega_n} \qquad r = C_p \, \omega_n \, R \tag{2.8}$$

In these expressions, ω and ω_n are the driving and natural frequencies. Thus, Ω is the nondimensional frequency ratio. The nondimensional coupling coefficient k_e^2 and mechanical damping ratio ζ are helpful in understanding the relative amount of energy lost to harvesting and mechanical damping. The load resistance R is nondimensionalized as r.

It is important to realize that these systems can exhibit two distinct reso-

nances depending on the resistance of the applied load [25] [81] [39][89]. This phenomenon occurs when the ratio of electromechanical coupling to mechanical damping grows to a sufficiently large value, ($k_e^2/\zeta > \ 8.5$–10) and resistance is selected to maximize power [81] [89]. In these "high-coupling" cases, a circuit with a lower load resistance will exhibit a resonance at $\Omega = 1$, while higher resistances exhibit resonance at $\Omega = \sqrt{1 + k_e^2}$. These cases are called the short and open circuit resonances. For low coupling values, the mechanical system dynamics appear uncoupled from those of the harvesting circuit, and the resonance occurs at $\Omega = 1$.

2.3 Limits of Energy Harvester Efficiency

2.3.1 Harvester input power and efficiency definition

The efficiency of any system is defined as the ratio of the output work to input energy. In the case of piezoelectric energy harvesters, the output power is simply the harvested power (power transferred to load), while the input power is a function of the damping, the energy harvested, and the proximity of the harvester to resonance. While Liao and Sodano suggest that loss factor[1] should be used as a metric for judging the power output differences between energy harvester designs [41], the efficiency is still an important metric in its own right. The efficiencies of piezoelectric energy harvesters are sometimes considered an afterthought, because the objects to which they are attached are considered as "infinite" power sources relative to the amount of harvested power. This is not

[1]Loss factor is defined as the energy lost per radian divided by the peak strain energy. See [31] section 2.7.

the case when the host structure is biological in nature. In such cases, it is important to understand the device efficiency in relation to the limits of the transducer technology.

To understand the efficiency limitation in these devices, we begin with the following definition of efficiency in relation to power input and output:

$$eff = \frac{P_h}{P_{input}} \tag{2.9}$$

where P_h is the harvested electrical power. At steady state, the input power into the system would be the sum of the rate of heat lost from the system and the rate of work done on/by the system. As previously mentioned, the two cases of efficiency under consideration are when the excitation source is capable (see figure 2.3(a)) and incapable (see figure 2.3(b)) of recovering the work done on it by the harvester. The input energy depends on the definition of the system boundary for which we are computing efficiency. Figure 2.3 shows the boundary considered here. We include the excitation source in the system boundary because we are interested in the efficiency when energy transferred to the source from the harvester cannot be recovered (Fig. 2.3(b)). Shu and Lien developed the efficiency result for a boundary only around the harvester [82] and we will show that their result is equivalent to the harvester-source system when the source is capable of energy recovery from the harvester (Fig. 2.3(a)).

The net work done by the excitation source is equal to the sum of the energy lost to damping on the harvester and the harvested energy. In order to develop an expression for excitation output power, the following energy balance is evaluated over a single period to develop expressions for the average energy harvested and energy lost to mechanical damping.

$$\int_{t_i}^{t_f} F(t)\dot{u}(t)\,\mathrm{d}t = \int_{t_i}^{t_f} C\dot{u}^2(t)\,\mathrm{d}t + \int_{t_i}^{t_f} V_p(t)I(t)\,\mathrm{d}t \tag{2.10}$$

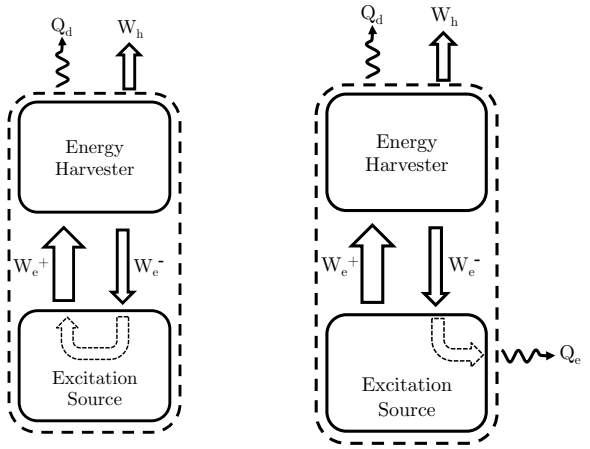

(a) Conserved case (b) Nonconserved case

Figure 2.3: Boundaries and energy flow in the energy harvesting system for the two assumptions surrounding energy transferred to the excitation source.

Here $F(t)$ is the modal input force function from the excitation source, $u(t)$ is the modal displacement, C is the mechanical damping constant, $V_p(t)$ is the piezoelectric element voltage, and $I(t)$ is the electric current. Here t_i and t_f represent the time at the beginning and end of one vibration cycle. In this expression, the left side of the equation represents the energy input from the excitation source, while the right is that output by the harvester. The rate of work done by the excitation source is thus:

$$P_e = F(t)\dot{u}(t). \tag{2.11}$$

If the input force and modal displacement are assumed to take on the following form:

$$F(t) = F_0 \sin(\omega t) \tag{2.12}$$

$$u(t) = u_0 \sin(\omega t - \theta), \tag{2.13}$$

the resulting expression for input power would thus be:

$$P_e(t) = F_0 u_0 \omega \sin(\omega t)\cos(\omega t - \theta). \tag{2.14}$$

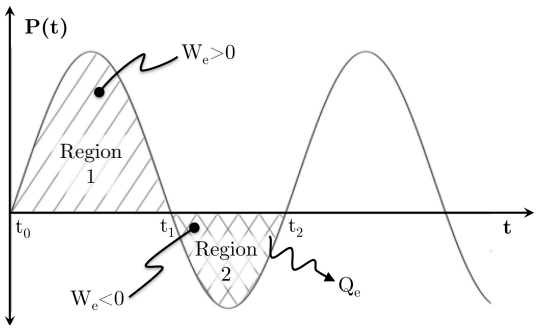

Figure 2.4: Waveform of input power from base excitation.

The time dependent terms in this equation ($\sin(\omega t)\cos(\omega t - \theta)$) are plotted in figure 2.4. In this figure we can see that during portions of the cycle, there is energy input to the harvester (region 1, where $W_e > 0$) and during other parts of the cycle energy is removed from the harvester (region 2, where $W_e < 0$). The asymmetry in these two regions is a result of the phase angle θ, caused by proximity to resonance and damping (mechanical and electrical) in the system. In a system far from resonance, the energy in these two sections of the cycle would cancel, suggesting that no average power would be required to maintain the motion of the harvester. The extreme example of this case is the excitation of a simple mass with no spring or damper. In such a case, this definition of input power suggests that no power would be required to maintain the sinusoidal motion of the mass. This is only true if the work done on the excitation source by the harvester in region 2 is conserved by the source so that it may be reapplied in the next half cycle. We call this the *conservative case* assumption. If the excitation source is incapable of energy recovery, then it must dissipate the work done on it from t_1 to t_2 as heat, shown in figures 2.4 and 2.3(b). We designate this case as the *nonconservative case*.

When we view the harvester and excitation source together from a thermodynamics perspective, the system can be conceptualized in terms of the bound-

aries shown in figure 2.3. In this figure we show the two cases under consideration. Recall the thermodynamic sign convention that work done on a system is negative, and heat transferred from the system is negative. As such, the waveform shown in figure 2.4 can be thought of as the rate of change of work done by the excitation source. In figure 2.3(a), the excitation source is capable of recovering energy as work is done on it by the energy harvester during region 2 of the power cycle. In the nonconservative case, figure 2.3(b), the source is not capable of energy recovery, and the work done on it by the harvester (when W_e is negative) must be dissipated. This negative work, or eccentric work as it is known, is the subject of much research in physiology. It has been claimed that the all of negative work is dissipated as heat [29]. While there is evidence that some energy can be stored elastically muscles and tendons, this storage depends heavily on the time scales of the forcing [42] [35]. Furthermore, there is significant evidence that the efficiency of positive and negative work from a muscle are drastically different, and that positive work requires significantly more energy from the host than does negative work [5] [8] [16]. Based on this, when performing positive work, the waste heat from a biological excitation source would appear mainly from inefficiencies in muscle actuation. When performing negative work, in addition to heat from inefficiency, additional heat would result from the dissipation of this negative work.

Although there is heat lost due to inefficiencies of muscle actuation, both for positive and negative work, these inefficiencies depending on the test conditions. At a minimum though, as Hill suggests, the heat dissipated to the environment is equal to the work done on the biological entity (region 2 of Fig: 2.4) [29]. We designate this heat loss as Q_e. When this additional heat term is accounted for, the overall energy output of the host increases, thus lowering the

system cycle efficiency.

In either of the two excitation cases, the efficiency can be calculated by dividing the harvested energy (W_h) by the change of energy state of the system ΔE. Over a cycle:

$$\Delta E = Q - W \tag{2.15}$$

$$W = W_h \tag{2.16}$$

$$Q = Q_e + Q_d \tag{2.17}$$

where Q_e would be zero in the conservative case and Q_d is the energy lost to damping in the harvester. The efficiency is thus,

$$\mathit{eff} = \frac{W_h}{W_h - Q_d - Q_e} \tag{2.18}$$

We know from equations 2.10 and 2.11 that

$$W_h - Q_d = W_e = \int_{t_i}^{t_f} P_e(t)\,\mathrm{d}t \tag{2.19}$$

If we are interested in average efficiency at steady-state, it is sufficient to investigate the average input power over one cycle from t_0 to t_2. Thus the average efficiency would be.

$$\mathit{eff} = \frac{\overline{P_h}}{\frac{1}{t_2 - t_0}\left[\int_{t_0}^{t_1} P_e(t)\,\mathrm{d}t + \int_{t_1}^{t_2} P_e(t)\,\mathrm{d}t - \int_{t_0}^{t_2} \dot{Q}_e(t)\,\mathrm{d}t\right]} \tag{2.20}$$

If the excitation source is capable of energy recovery from the harvester, the integral of the $\dot{Q}_e(t)$ term would be zero (assuming no other sources of loss). The resulting expression for average efficiency would be:

$$\mathit{eff}_c = \frac{\overline{P_h}}{\frac{1}{t_2 - t_0}\left[\int_{t_0}^{t_2} P_e(t)\,\mathrm{d}t\right]} \tag{2.21}$$

We use the subscript 'c' here to distinguish the conservative case assumption. The evaluation of this expression would result in the efficiency expression developed by Shu [82], and presented later in this work (equation 2.32) to compare

with the case when the source is not capable of energy recovery. If the excitation source is not capable of recovering work done on it by the harvester, and must dissipate this energy, the energy of region 2 in figure 2.4 would be equivalent to the energy lost through Q_e, resulting in the efficiency expression

$$\mathit{eff}_{nc} = \frac{\overline{P_h}}{\frac{1}{t_2 - t_0}\left[\int_{t_0}^{t_1} P_e(t)\,\mathrm{d}t\right]} \tag{2.22}$$

Note that the limits of the integral in the denominator are taken to be over the portions of the harvester input power function that are greater than zero. Thus, the denominator of equation 2.22 can be thought of as the average of the power transferred to (but not from) the harvester over one cycle. We develop an expression for this and the resulting efficiency equation in the following section.

2.3.2 Efficiency expression development

To find the efficiency when the excitation source is incapable of energy recovery, we begin by developing an expression of the average of the positive portions of the power output of the excitation source (P_e). This would be the denominator of equation 2.22.

$$\overline{P_{e+}(t)} = \frac{1}{t_2 - t_0}\int_{t_0}^{t_1} P_e(t)\,dt \tag{2.23}$$

We can see the time dependent portion of equation 2.14 is $\sin(\omega t)\cos(\omega t - \theta)$. The limits of integration and time period over which the average is taken (t_0, t_1, t_2) can be seen in figure 2.4. As we are interested in only those portions of the function that are greater than zero, our limits of integration correspond the zero

crossings at:

$$t_0 = \begin{cases} 0 & 0 < \theta \leq \pi/2 \\ (-\pi/2 + \theta)/\omega & \pi/2 < \theta \leq \pi \end{cases} \tag{2.24}$$

$$t_1 = \begin{cases} (\pi/2 + \theta)/\omega & 0 < \theta \leq \pi/2 \\ \pi/\omega & \pi/2 < \theta \leq \pi \end{cases} \tag{2.25}$$

$$t_2 = \begin{cases} \pi/\omega & 0 < \theta \leq \pi/2 \\ (\pi/2 + \theta)/\omega & \pi/2 < \theta \leq \pi \end{cases} \tag{2.26}$$

Using these limits of integration, the average of the positive excitation source power (denominator of 2.22) can be shown to be:

$$\overline{P_{e+}(t)} = F_0 u_0 \omega \xi(\theta) \tag{2.27}$$

$$\xi(\theta) = \begin{cases} \frac{(\pi/2+\theta)\sin\theta + \cos\theta}{2\pi} & 0 < \theta \leq \pi/2 \\ \frac{(3\pi/2-\theta)\sin\theta - \cos\theta}{2\pi} & \pi/2 < \theta \leq \pi \end{cases} \tag{2.28}$$

The magnitude of the modal displacement, u_0, can be expressed as [81]:

$$u_0 = \frac{F_0}{K\sqrt{\psi}} \tag{2.29}$$

$$\psi = \left(2\zeta + \frac{2k_e^2 r}{\left(r\Omega + \frac{\pi}{2}\right)^2}\right)^2 \Omega^2 + \left(1 - \Omega^2 + \frac{\Omega\, k_e^2 r}{r\Omega + \frac{\pi}{2}}\right)^2 \tag{2.30}$$

Using this expression, in conjunction with equation 2.28, we can develop an expression of the average of the positive portions of the power curve.

$$\overline{P_{e+}(t)} = \frac{F_0^2 \omega \xi(\theta)}{K\sqrt{\psi}} \tag{2.31}$$

We now have an expression for average total input power, but to calculate efficiency we need an expression for the harvested power. This has been shown to be [81]

$$\overline{P_h} = \frac{F_0^2}{\omega_n M} \frac{k_e^2\, \Omega^2\, r}{\left(r\,\Omega + \frac{\pi}{2}\right)^2} \frac{1}{\psi} \tag{2.32}$$

for the harvesting circuit considered here. Dividing equations 2.31 and 2.32 allows for the efficiency to be expressed as:

$$\mathit{eff}_{nc} = \frac{k_e^2 \Omega r}{\left(r\Omega + \frac{\pi}{2}\right)^2} \frac{1}{\sqrt{\psi}} \frac{1}{\xi(\theta)} \tag{2.33}$$

The only remaining unknown term in this expression is the phase angle θ. This can be determined by first carrying out the integration of equation 2.10 over a half cycle between displacement extremes to create the energy balance expression for the system [82]. Additionally, an expression for the magnitude of the applied force F_0 [81] is needed. These two expressions are:

$$\frac{\pi}{2} F_0 u_0 \sin\theta = \frac{\pi}{2} C\omega u_0^2 + \frac{\pi}{\omega} \frac{V_c^2}{R} \tag{2.34}$$

$$F_0 \cos\theta = \left(K - M\omega^2 + \frac{\Theta^2}{C_p}\right) u_0 - \frac{\pi\Theta}{2C_p\omega R} \tag{2.35}$$

Where V_c is the voltage over the filtering capacitor. Solving equation 2.35 for F_0 and substituting into equation 2.34, allows us to solve for the phase angle θ.

$$\theta = \tan^{-1}\left[\frac{\pi C\omega u_0^2 + \frac{\pi}{\omega}\frac{V_c^2}{R}}{\frac{\pi}{2}u_0\left[\left(K - M\omega^2 + \frac{\Theta^2}{C_p}\right)u_0 - \frac{\pi\Theta}{2C_p\omega R}V_c\right]}\right] \tag{2.36}$$

This expression can be rewritten in terms of non-dimensional parameters.

$$\theta = \tan^{-1}\lambda \tag{2.37}$$

$$\lambda = \left[\frac{2\Omega\zeta + \frac{2k_e^2\Omega r}{\left(r\Omega+\frac{\pi}{2}\right)^2}}{1 - \Omega^2 + k_e^2 - \frac{\pi}{2}\frac{k_e^2}{\left(r\Omega+\frac{\pi}{2}\right)}}\right] \tag{2.38}$$

Notice that this collapses to the phase angle for a mass, spring, damper when either coupling (k_e^2) or resistance (r) are set to zero[2]. Substituting this expression into equation 2.33 gives the efficiency for the nonconservative case when the excitation source is incapable of energy recovery. Alternatively, the efficiency

[2]See [31], section 2.6

for a conservative case is [82]:

$$\mathit{eff}_c = \frac{r\frac{k_e^2}{\zeta}}{(r\Omega + \frac{\pi}{2})^2 + r\frac{k_e^2}{\zeta}} \tag{2.39}$$

In either case, the efficiency of these harvesters depends only in the non-dimensional coupling coefficient (k_e^2), mechanical damping ratio (ζ), non-dimensional resistance (r), and frequency ratio (Ω). Although closed form expressions for the exact ideal resistance (from a power maximization perspective) have not been developed in a general sense, their values can nonetheless be found by sweeping resistance values in the power equation (equation 2.32 [81]). This sweep can be done at each coupling coefficient, frequency ratio, and damping ratio under consideration. The resulting ideal resistances allow for efficiency to be expressed graphically as a function of the three variables k_e^2, ζ, and Ω.

2.3.3 Efficiency results and limits

In figures 2.5, 2.6, and 2.7 we plot the efficiency for the conservative and non-conservative cases as a function of k_e^2 and Ω for damping ratios of 0.01, 0.03, and 0.05, respectively. Note that each figure represents the efficiency at a different damping ratio. We plot dotted lines in these contours to highlight the two resonances at $\Omega = 1$ and $\Omega = \sqrt{1 + k_e^2}$. When comparing the conservative and nonconservative cases of each of these figures we immediately notice some striking differences and similarities. The primary difference is that when operating above the open circuit natural frequency or below the short circuit natural frequency, the conservative analysis predicts much higher efficiencies. This is to be expected, as the excitation source in the conservative case is able

to recover power when the harvester is operated off resonance. The differences in these regions illuminates the fundamental importance of this analysis. Many systems that need to consider efficiency, such as biological systems, will not have a purely harmonic excitation frequency. These sources are likely to operate at a variety of excitation frequencies and thus the harvester will be operating above and below resonance. In such cases, use of the conservative assumption of excitation could lead to drastic over predictions of the effectiveness of energy conversion to harvester power.

Despite the difference in efficiency in off resonance cases, there are a variety of similarities between the conservative and nonconservative assumption cases that allow for general conclusions to be drawn about harvester efficiency. An interesting result of figures 2.5, 2.6, and 2.7 is that in both cases, and for all damping ratios, efficiency is high when the system is operated between the open and closed circuit resonances. This result is explored further in figure 2.8. The efficiencies plotted here can be though of as a vertical slices of figures 2.6(a) and 2.6(b) at $k_e^2 = 0.6$ ($\zeta = 0.03$). We also plot the normalize nondimensional power and modal displacement of the harvester for discussion. In this figure we see the same peak in efficiency between the two resonances. We can see that the peak in efficiency corresponds to a drop in both power and displacement. The reason for the increase in efficiency here despite a decrease in power is a result of the relationship between damping and harvested power, along with the way in which resistance is chosen.

The nondimensional expressions for average harvester power [81] and

damped power, are shown below (with '*' denoting nondimensionality).

$$\overline{P_h^*} = \frac{\overline{P_h}}{\frac{F_0^2\omega_n}{K}} = k_e^2\Omega^2 u_0^{*2}\frac{r}{(r\Omega+\pi/2)^2} \tag{2.40}$$

$$\overline{P_d^*} = \frac{\overline{P_d}}{\frac{F_0^2\omega_n}{K}} = \zeta\Omega^2 u_0^{*2} \tag{2.41}$$

Here the nondimensional modal displacement is $u_0^* = u_0/(F_0/K)$. When presented in this way, it becomes apparent that for fixed k_e^2 and ζ, the only difference between these two expressions is the $r/(r\Omega+\pi/2)^2$ term. This term allows the power to change independent of damping for various values of Ω. We can see in figure 2.8 that as Ω increases beyond the short circuit natural frequency (unity), the nondimensional modal displacement decreases. Without the $r/(r\Omega+\pi/2)^2$ term, we would expect this decrease in displacement to not affect efficiency, because harvested and damped power would be equally affected. With this term though, the resistance takes on a value such that power can be positively affected when displacement is not dominating the power output. This helps to explain the interesting result that efficiency is typically improved by operating off resonance and why a maximum appears when operating halfway between the closed and open circuit resonances:

$$\Omega_{\text{max efficiency}} = \frac{1+\sqrt{1+k_e^2}}{2}. \tag{2.42}$$

At either resonance, we can see in figure 2.8 that the high displacement would tend to dominate the power expressions 2.40 and 2.41. When off resonance, displacement decreases and the $r/(r\Omega+\pi/2)^2$ term allows for an increase in power production and thus efficiency improvements. We should note that this result is an artifact of resistance being selected to maximize power. We concentrate on the power maximization case, as it is nearly exclusively used for these devices.

Beyond these results, we can also see in figures 2.5, 2.6, and 2.7 that in both

the conservative and nonconservative cases, the efficiency at the highlighted resonant frequencies of $\Omega = 1$ and $\Omega = \sqrt{1 + k_e^2}$ tends to be limited as the coupling increases. Furthermore, in these contours we can see that the plateau in the resonant efficiency appears to be independent of mechanical damping ratio and the resonances ($\Omega = 1$ or $\Omega = \sqrt{1 + k_e^2}$). We explore this fact further in figures 2.9(a) and 2.9(b). In these figures, we plot the efficiency specifically at the resonant frequencies, because they represent the peak for power production [89, 25, 81] and thus represent the typical operating points. The data is plotted as a function of k_e^2/ζ rather than k_e^2 to reduce the dependency on damping. Figure 2.9(a) is the efficiency for $\Omega = 1$ plotted for all three damping ratios. Note that all three damping ratios collapse onto a single curve. In figure 2.9(b) we plot the deviation the $\Omega = \sqrt{1 + k_e^2}$ results from those of the $\Omega = 1$ case because the differences between the two cases are quite small. These two plots show that efficiency at resonance is effectively independent of damping ratio for a given value of k_e^2/ζ. This stands to reason given equations 2.40 and 2.41. For constant k_e^2/ζ and Ω, the only term that can affect the ratio of the harvested and damped power comes from differences in the resistance used. In the limiting cases of extremely high and low coupling, approximations of these resistances are independent of ζ for a fixed k_e^2/ζ [81], and thus we should expect little to no dependence of efficiency on damping.

The most interesting result that can be see in figure 2.9(a) is the limit in efficiency. We can see that in both frequency ratio cases, as well as both excitation cases (conservative and nonconservative), there appears to be a plateau in the efficiency and that the value of this plateau is nearly the same in both cases. Figure 2.9(a) is plotted with a maximum k_e^2/ζ value of 20 to illuminate the shape of the curve for lower k_e^2/ζ values. We can see that between $k_e^2/\zeta = 0$ and $k_e^2/\zeta = 4$,

the efficiency varies nearly linearly between 0 and 34%. At higher coupling values, the efficiency appears to approach a limit of slightly more than 43%. The value of this limit can be calculated analytically for the conservative case at resonance by allowing $k_e^2/\zeta \to \infty$ in efficiency equation 2.39. If we assume $k_e^2/\zeta >> 1$, concentrate on resonant frequencies, and use the approximate ideal resistances presented in table 2.1, equation 2.39 reduces to the following:

$$\mathit{eff}_{c-max} = \frac{4}{4 + \sqrt{\pi^2 + 16}} \approx 0.44 \tag{2.43}$$

This maximum efficiency of 44% results from both resonances at $\Omega = 1$ and $\Omega = \sqrt{1 + k_e^2}$. Intuitively, this limits can be understood by realizing the power lost to damping increases as $\zeta \to 0$. Conversely, harvested power increases as coupling coefficient (k_e^2) increases. Thus, we would expect a balance as the ratio of these terms approaches zero.

The analytic prediction of 44% is for the conservative assumption case and we can see in figure 2.9(a) that the nonconservative case has a limit which is only slightly lower. The reason for this difference is that at resonance, only a small amount of work is done on the excitation source by the harvester. This work is due to the slight deviation of the phase angle from $\pi/2$ caused by the electromechanical coupling (see equation 2.38). Since this system is lightly damped, this phase deviation is relatively small and only a small amount of work is done by the harvester on the excitation source. The resulting energy lost to heat is therefore small at resonance.

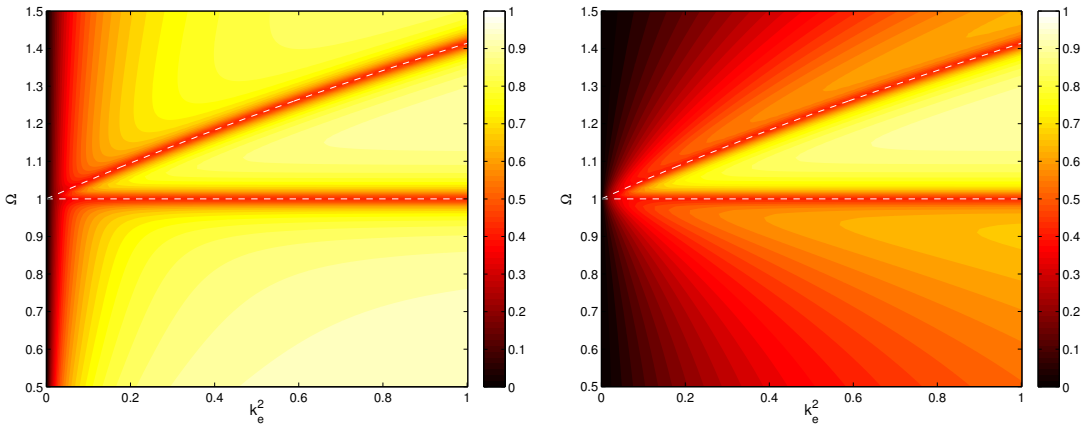

(a) Conservative assupmtion (b) Nonconservative assumption

Figure 2.5: Efficiency for $\zeta = 0.01$ for both conservative and nonconservative cases. Resonances at $\Omega = 1$ and $\Omega = \sqrt{1 + k_e^2}$ highlighted with dashed line.

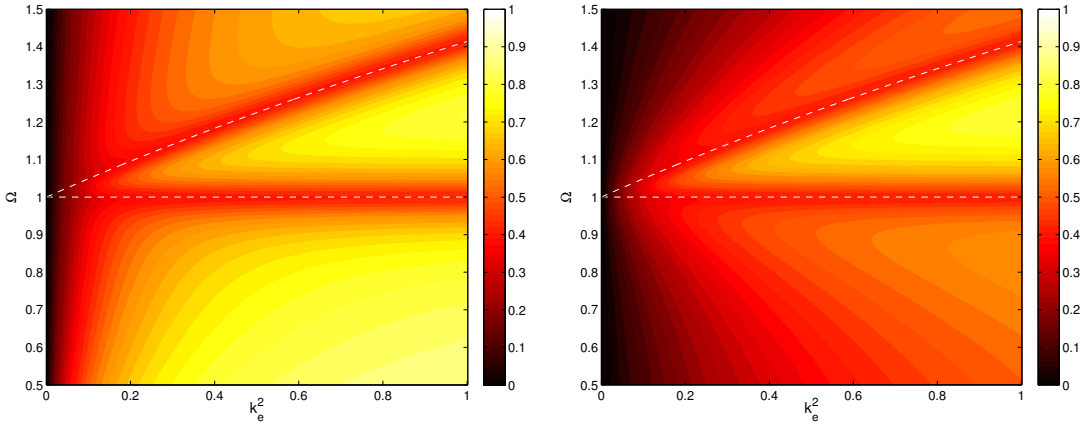

(a) Conservative assumption (b) Nonconservative assumption

Figure 2.6: Efficiency for $\zeta = 0.03$ for both conservative and nonconservative cases. Resonances at $\Omega = 1$ and $\Omega = \sqrt{1 + k_e^2}$ highlighted with dashed line.

Table 2.1: Resistances for maximum power for energy harvesters operated at resonance and high values of k_e^2/ζ [25] [81] .

Ω	$r_{\text{max power}}$
1	$\frac{\pi^2}{\sqrt{16+\pi^2}} \frac{1}{\frac{k_e^2}{\zeta}}$
$\sqrt{1+k_e^2}$	$\frac{\sqrt{16+\pi^2}}{4} \frac{\frac{k_e^2}{\zeta}}{1+k_e^2}$

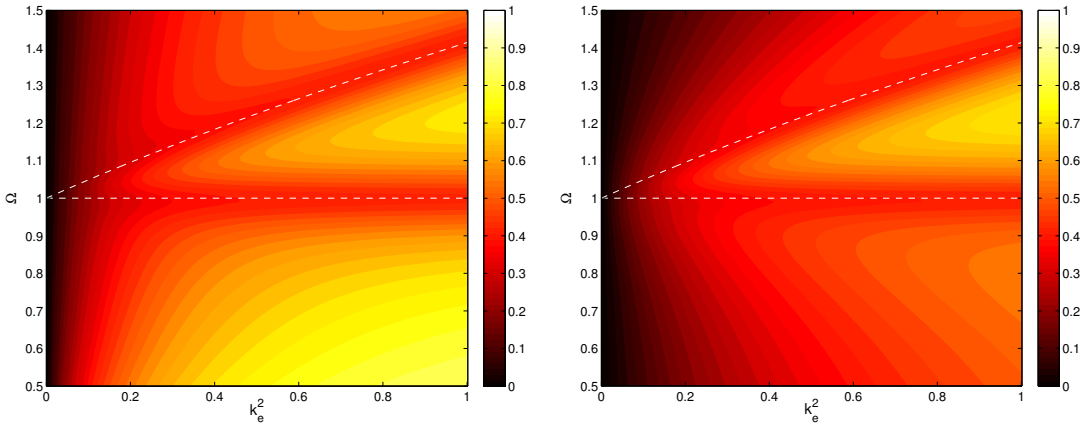

(a) Conconservative assumption (b) Nonconservative assumption

Figure 2.7: Efficiency for $\zeta = 0.05$ for both conservative and nonconservative cases. Resonances at $\Omega = 1$ and $\Omega = \sqrt{1 + k_e^2}$ highlighted with dashed line.

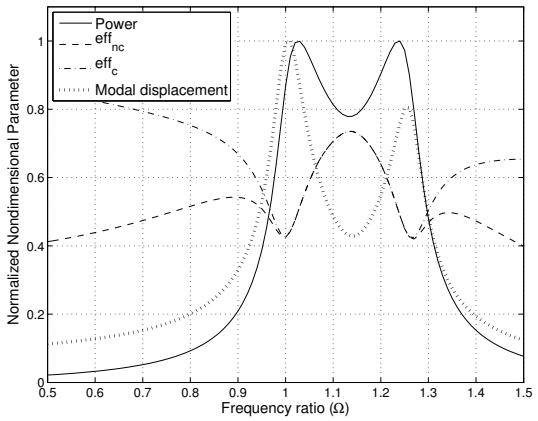

Figure 2.8: Normalized nondimensional power and efficiency as a function of frequency ratio for $k_e^2 = 0.6$ at $\zeta = 0.03$. Efficiency shown for both cases when excitation source is capable and is not capable of energy recovery.

2.4 Maximum Stress, Allowable Acceleration, and Maximum Power from Piezoelectric Energy Harvesters

2.4.1 Equation development

The power available from a piezoelectric energy harvester is fundamentally limited by the maximum allowable stress of the material. Increasing the stress in a

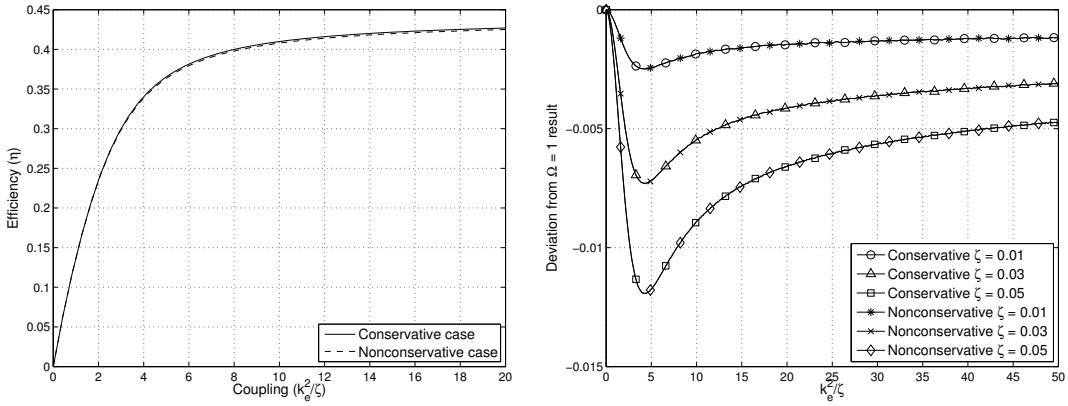

(a) (b)

Figure 2.9: (a) Efficiency as a function of k_e^2/ζ for $\Omega = 1$, both for the conservative and nonconservative cases for all three damping ratios under consideration. (b) Deviations of the efficiencies for $\Omega = \sqrt{1 + k_e^2}$ from the $\Omega = 1$ result for the three damping ratios under consideration.

piezoelectric material will increase the electric field across as prescribed by the constitutive equation for a piezoelectric material [1]:

$$\begin{bmatrix} T \\ D \end{bmatrix} = \begin{bmatrix} c^e & -e^T \\ e & \epsilon^s \end{bmatrix} \begin{bmatrix} S \\ \mathrm{E}^f \end{bmatrix} \tag{2.44}$$

Note that here, the typical notation is used where S is the strain, D is the electrical displacement, c^e is the modulus of elasticity, e is the piezoelectric stress coefficient, ϵ^s is the dielectric constant, T is the stress, and E^f is the electric field. Changes in the electric field increase the current flow in a harvester circuit, and as such it is typically advantageous to increase the stress in the material. This increase in stress can only be taken to the point at which the material fails, and the harvester no longer produces power. We are interested in how much power can be harvested prior to this rupture event. We concentrate our efforts in this regard to the typical cantilevered harvester operated at the first resonant frequency.

As cantilever piezoelectric energy harvesters typically employ 1-3 coupling

[26], we can extract the equation for stress in the 1-direction of the piezoelectric material as:

$$\sigma_x = E_x \epsilon_x - e\mathrm{E}_y^f \tag{2.45}$$

Here we have used σ_x for stress along the length of the beam, E_x as the piezoelectric modulus in the 1-direction, ϵ_x as strain along the length, and E_y^f as the the electric field in the y direction. This expression can be put in terms of the radius of curvature (ρ) through the use of the following relationship.

$$\epsilon_x = \frac{-y}{\rho} \tag{2.46}$$

Here y represents the distance from the neutral axis to the outermost surface of the outermost piezoelectric layer. We choose this layer in order to determine the maximum stress on the most minimum strength layer of the laminate, and assume this weakest layer is the piezoelectric element. For example, in figure 2.10, y_{i+1} would represent the most extreme y value of the piezoelectric layers of that particular laminate. Note that y can be positive or negative and its sign should match the convention used in figure 2.1. Also note that the negative sign in equation 2.46 represents a concave up curvature in the beam subjected to a positive moment.

The radius of curvature in equation 2.46 can be related to the curvature in the beam (w'') through the following expression

$$\rho = \frac{(1 + w'^2)}{w''} \approx \frac{1}{w''}. \tag{2.47}$$

For beams with relatively small slopes, the curvature is inversely related to the radius of curvature. Using equations 2.46 and 2.47, equation 2.45 thus becomes

$$\sigma_x = -E_x y w'' - e\mathrm{E}_y^f \tag{2.48}$$

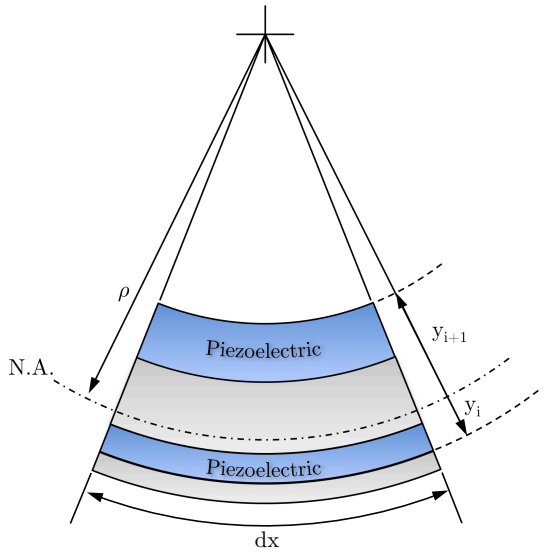

Figure 2.10: General diagram of harvester beam cross section

The curvature in equation 2.48 can be related to the beam deflection through the separation of the temporal and spacial components.

$$w(x,t) = u(t)\phi(x)$$
$$w''(x,t) = u(t)\phi''(x) \tag{2.49}$$

Where $u(t)$ is the beam modal displacement and $\phi(x)$ is the mode shape. As we are interested in the limiting case in this single mode approximation, we will look to the peak stress in the beam occurring at maximum modal displacement (assuming $u(t) = u_0 \sin(\omega t - \theta)$). Thus

$$w''_{peak} = u_0\phi''(x) \tag{2.50}$$

The maximum modal deflection is given in equation 2.29, restated here in terms of modal mass and acceleration amplitude.

$$u_0 = \frac{MA}{K}\frac{1}{\psi^{\frac{1}{2}}} \tag{2.51}$$

In this equation, A is the magnitude of base acceleration, and ψ is defined by equation 2.30.

Now with an expression for the modal displacement of the beam (equation 2.51), along with equations 2.50 and 2.48, we come to the following expression for stress in the piezoelectric material

$$\sigma = \frac{-MAE_x y}{K\psi^{\frac{1}{2}}}\phi''(x) - e\mathrm{E}_y^f \tag{2.52}$$

Although $\phi''(x)$ would typically be evaluated at $x = 0$, to determine the stress at the root of the beam, it is left here in terms of x for generality. We must now determine an expression for the electric field E_y^f in the piezoelectric material. The electric field in a piezoelectric layer can be approximated by $-\operatorname{sgn}(y)v/t_p$ [83], where v is the voltage of the piezoelectric element. Like w'', voltage v is a function of time, but the peak value is equivalent to the rectified voltage across the filtering capacitor which is given as [81]:

$$v = \frac{MA}{\Theta}\frac{r\Omega}{\left(r\,\Omega + \frac{\pi}{2}\right)}\frac{k_e^2}{\psi^{\frac{1}{2}}} \tag{2.53}$$

Given the results of equations 2.48 and 2.53, we can develop a general expression for the stress developed in the laminated piezoelectric layer.

$$\sigma_x = \frac{MA}{\psi^{\frac{1}{2}}}\left[\frac{-E_x y\phi''(x)}{K} + \frac{\operatorname{sgn}(y)ek_e^2}{t_p\Theta}\frac{r\Omega}{\left(r\,\Omega + \frac{\pi}{2}\right)}\right] \tag{2.54}$$

This equation can be solved for the amplitude A, which if the allowable stress in the piezoelectric material is used (σ_{max}), provides the maximum allowable peak base acceleration.

$$A_{max} = \sigma_{max}\psi^{\frac{1}{2}}\left[\frac{-E_x y\phi''(x)}{\omega_n^2} + \frac{\operatorname{sgn}(y)eM}{t_p\Theta}\frac{r\Omega k_e^2}{\left(r\,\Omega + \frac{\pi}{2}\right)}\right]^{-1} \tag{2.55}$$

This general expression provides a limit of input acceleration into a piezoelectric energy harvester. The proper sign on σ_{max} should be used, positive for tensile and negative for compressive. We should note that we have not made

assumptions as to the shape of the beam, other than the fact that it is symmetric about the x-y plane. The only other assumptions are that electric field is constant through the piezoelectric material and only the first mode of vibration is excited. The term in brackets in equation 2.55 can be thought of as having two contributions: the first term being the contribution from the mechanical strain in the beam, and the second coming from the charge related strain caused by the piezoelectric effect. Note that if zero resistance is used (short circuit condition) the charge strain term is eliminated.

This expression for the maximum allowable acceleration is useful in providing the information necessary to assess the viability of a design in relation to the acceleration environment. It can also be used determine the maximum possible power that could be developed by a given harvester design. To do this we begin with the average harvester power equation (2.32), restated here in terms of modal mass and excitation amplitude.

$$P = \frac{MA^2}{\omega_n} \frac{k_e^2 \, \Omega^2 \, r}{\left(r \, \Omega + \frac{\pi}{2}\right)^2} \frac{1}{\psi} \tag{2.56}$$

Here we drop the overbar denoting average power, as we no longer need to distinguish average and peak power. This equation depends on the previously mentioned ψ function (equation 2.30), as well as modal mass M, base acceleration magnitude A, and system natural frequency ω_n. Plugging equation 2.55 into this power equation gives the maximum limit for power from a piezoelectric energy harvester.

$$P_{max} = \frac{M\sigma_{max}^2}{\omega_n} \frac{k_e^2 \, \Omega^2 \, r}{\left(r \, \Omega + \frac{\pi}{2}\right)^2} \times \left[\frac{-E_x y \phi''(x)}{\omega_n^2} + \frac{\mathrm{sgn}(y) e M}{t_p \Theta} \frac{r \Omega k_e^2}{\left(r \, \Omega + \frac{\pi}{2}\right)} \right]^{-2} \tag{2.57}$$

Notice the cancellation of the ψ term, and thus the elimination of mechanical damping ratio from the expression. This is to be expected. Changes in damping

would result in changes in displacement and stress in the material. Because we use the maximum allowable acceleration, systems with higher damping would simply have larger allowable acceleration magnitudes. We can see this relationship between ζ and A_{max} in equation 2.55.

The second group of terms with in the brackets of equation 2.57 is a result of the piezoelectric coupling and charge flow through the resistive load. This term is typically small with respect to the mechanical term $E_x y \phi''(x)/\omega_n^2$ for most energy harvesting systems. Thus a more compact, yet slightly less conservative estimate for the maximum power available from the harvester can be simply stated as:

$$P_{max} = \frac{M\omega_n^3 \sigma_{max}^2}{E_x^2 y^2 \phi''(x)^2} \frac{k_e^2\, \Omega^2\, r}{\left(r\,\Omega + \frac{\pi}{2}\right)^2}. \tag{2.58}$$

Although more simple to compute, it is important to remember that this expression will slightly over estimate the available power, as it neglects stress in the piezoelectric material due to charge accumulation. We can develop expressions for the maximum possible power for systems of low coupling and high coupling, operated at both short and open circuit resonance by using the ideal resistances in the three cases [81]. The ideal resistance for the uncoupled case is simply $\pi/(2\Omega)$. The high coupling ideal resistances are listed in table 2.1. In order to be concise, we use the following variables to represent the constants associated with each of these ideal resistances.

$$C_{sc} = \frac{\pi^2}{\sqrt{16+\pi^2}} \tag{2.59}$$

$$C_{oc} = \frac{\sqrt{16+\pi^2}}{4} \tag{2.60}$$

Substituting these ideal resistances into equation 2.58 for the three coupling cases (uncoupled, high coupling with short circuit ideal resistance, and high

coupling with open circuit ideal resistance), the maximum power equation can be reduced to

$$P_{max-UC} = \frac{M\omega_n^3\sigma_{max}^2}{E_x^2 y^2 \phi''(x)^2}\frac{k_e^2}{2\pi} \tag{2.61}$$

$$P_{max-HCsc} = \frac{M\omega_n^3\sigma_{max}^2}{E_x^2 y^2 \phi''(x)^2}\frac{4C_{sc}k_e^2\zeta}{\left(\pi k_e^2 + 2C_{sc}\zeta\right)^2} \tag{2.62}$$

$$P_{max-HCoc} = \frac{M\omega_n^3\sigma_{max}^2}{E_x^2 y^2 \phi''(x)^2}\frac{C_{oc}k_e^2}{\left(\frac{\pi}{2} + \frac{C_{oc}k_e^2}{\zeta(k_e^2+1)^{\frac{1}{2}}}\right)^2}\frac{k_e^2}{\zeta} \tag{2.63}$$

These expressions can be used to quickly estimate the maximum output power for a given design. If the design is determined to be high coupling ($k_e^2/\zeta > 10$), equations 2.62 or 2.63 would be used, depending on the planned frequency ratio operating point. For lower values of coupling, equation 2.61 would suffice.

Although equations 2.61, 2.62, and 2.63 are convenient for power estimates given their simplicity, for thorough analysis we use the more general expression for maximum power presented in equation 2.57. Given this expression, we are in a position to assess the available power from a variety of piezoelectric energy harvester designs. Specifically, we would like to understand the maximum power available for systems across a range of masses and resonant frequencies. We focus here on the standard bimorph harvester shown in figure 2.1 as an example paradigm to investigate. The equation for harvested power (equation 2.56) depends on specific variables of the harvester design, such as piezoelectric material distance from the neutral axis, and piezoelectric material thickness. For this reason, we must develop specific designs for each mass and natural frequency under consideration.

2.4.2 Maximum power across mass and frequency

In order to develop a large number of ideal designs, we turn to a design methodology that uses system level requirements, and develops a design that maximizes the power output through optimization of the piezoelectric material thickness ratio [74]. Two analyses were presented in this work, one for fixed piezoelectric material thickness, and one for fixed width. We select the latter of the two cases to use here in order to constrain the aspect ratio (length/width) of the beams under consideration and use the following inputs for design constraints: system mass, excitation frequency, beam length, beam width, material properties (piezoelectric and substrate).

As we will be sweeping natural frequency and varying system mass in this analysis, we need to scale the dimensions (length and width) of the beams relative to their mass. We have selected to have the cube of the length of the beams be proportional to the system mass.

$$M_{sys} \propto L^3 \tag{2.64}$$

$$c_{ML} = \frac{M_{sys}}{L^3} \tag{2.65}$$

$$L = \left(\frac{M_{sys}}{c_{ML}}\right)^{1/3} \tag{2.66}$$

Here c_{ML} is a mass scaling constant. It has dimensions of density and can be thought of as how heavy the system is relative to its size.The total physical mass of the system, M_{sys} should be distinguished from the previously mention modal mass, M. Additionally, we use c_{Lw} to specify the aspect ratio of the beam, L/w. For this investigation, we select the substrate material to be stainless steel, and the piezoelectric material to be Navy Type II PZT. The piezoelectric and substrate material properties are listed in table 2.2.

Table 2.2: List of material properties

	Value	Unit	Name
ρ_s	7916.5	kg/m^3	Substrate Density
ρ_p	7800	kg/m^3	Piezoelectric Material Density
E_{sx}	212	GPa	Substrate Modulus
E_{px}	67	GPa	Piezoelectric Material Modulus
e	-12.73	C/m^2	Piezoelectric Stress Constant
ϵ^s	1.59e-8	C/m^2	Piezoelectric Permittivity
σ_{max}	76	MPa	Piezoelectric Ultimate Strength

The material properties for Navy Type II PZT can be found in various manufactures catalogs [4] [2] [3]. Channel Industries, Inc. lists ultimate tensile strength. Their value of 76 MPa is similar to the 88 MPa presented by Fu and Zhang for PZT-841[23]. Additionally, Makino and Kamiya suggest a value of approximately 85 MPa for a custom sintered PZT specimens, although no type was specified [44]. In their paper, they show the relationship between ultimate strength and load cycles. They predict a 55 MPa fatigue stress at 32×10^6 cycles, representing an approximately 30% reduction in allowable stress. Depending on the excitation frequency and planned operational period, a further reduction may be needed in order to prevent premature failure. We provide these numbers here as a reference, and will use an allowable strength of 76 MPa for our analysis to understand the absolute limits of power production.

When using the previously mentioned relationships between mass and the size of the beam, as well as the material properties listed in table 2.2, we are able to develop bimorph beam designs across a wide range of masses and natural frequencies. To do this, we first use the previously mentioned design methodology [74] to develop a range of harvester designs that all have the same length, width, mass, natural frequency, and only vary in thickness ratio ($2t_p/t$). We

then use equation 2.57, while sweeping thickness ratio and resistance to determine the optimal design and resistance for that particular mass and natural frequency. This is done at each natural frequency and system mass to determine the maximum power available for the technology, given the specified c_{ML} and c_{Lw} values.

The original Shafer et al. design method optimized the thickness ratio using equation 2.56, assuming that the acceleration magnitude (A) was not limited by beam design [74]. This is true for environments where the magnitude of acceleration will not result in a failure of the beam as predicted by equation 2.54, an assumptions almost universally made by energy harvesting researchers. In this analysis, we apply the maximum allowable acceleration of equation 2.55. As previously mentioned, this results in a power expression that is independent of damping ratio. As such, the following results do not depend on mechanical damping ratio.

This maximum power study was performed across a range of system masses of 1 to 100g. Additionally, frequency was swept from 10 to 200 Hz. The resulting maximum possible power is plotted for a variety of c_{Lw} and c_{ML} values. We first present results across a range of three beam aspect ratios, while holding the c_{ML} value constant at 45.6 kg/m^3. Figures 2.11, 2.12, and 2.13, present the maximum power results for beam planform aspect ratios of 1, 5 and 10, respectively. Note that the second plot in each of these figures shows the result for low mass and natural frequency systems that aren't resolved in the graduations of the first plot. We can see in these three figures that the maximum power tends to increase as the aspect ratio is decreased. This trend is to be expected. As the aspect ratio is decreased, the width increases in relation to the mass of the beam. To target

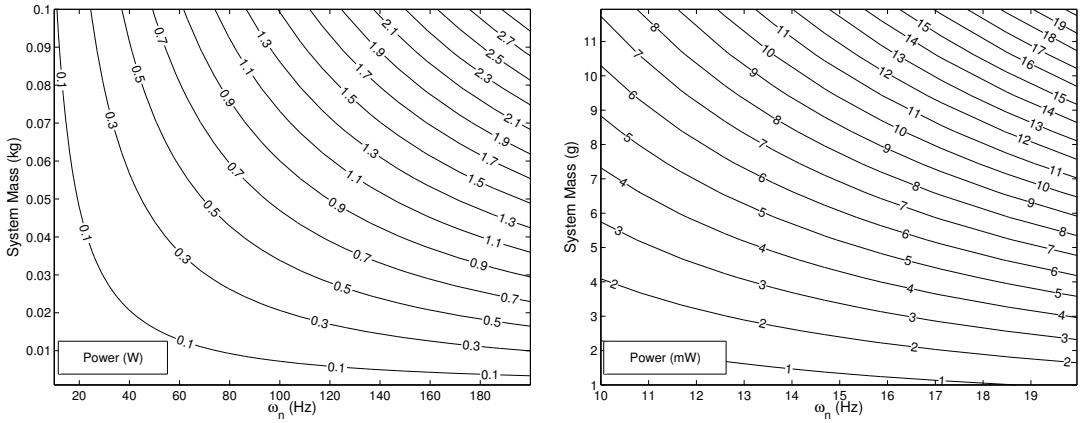

(a) (b)

Figure 2.11: Maximum power for $L/w = 1$ and $c_{ML} = 45.6$ kg/m^3. Low mass and natural frequency shown in (b) shows the results for systems of low mass and natural frequency.

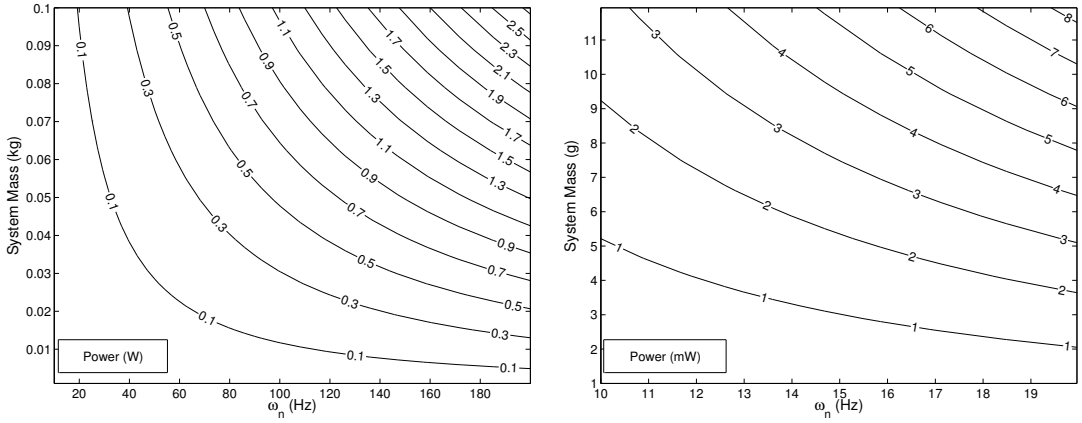

(a) (b)

Figure 2.12: Maximum power for $L/w = 5$ and $c_{ML} = 45.6$ kg/m^3. Low mass and natural frequency shown in (b) shows the results for systems of low mass and natural frequency.

the same frequency, these wider beams must therefore reduce their thickness. We can see in equation 2.57, power is nearly proportional to the inverse of the square of the distance of the piezoelectric layer from the neutral axis. As such, for these wider and therefore thinner beams, this distance from the neutral axis decreases, and we should expect the power to increase.

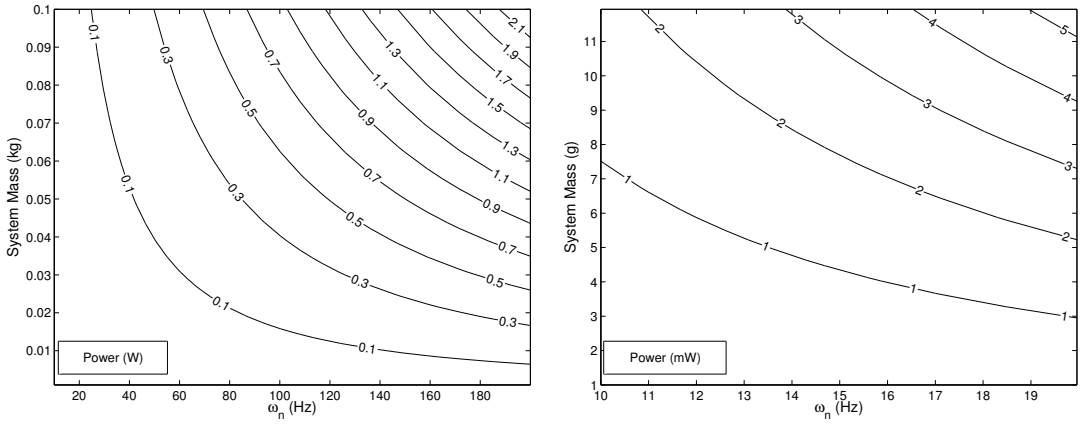

(a) (b)

Figure 2.13: Maximum power for $L/w = 10$ and $c_{ML} = 45.6$ kg/m^3. Low mass and natural frequency shown in(b) shows the results for systems of low mass and natural frequency.

The other variable that we can investigate is the proportionality constant, that relates the mass to the length of the beam (c_{ML}). As a note, a value of 45.6 kg/m^3 for this constant results in a 60 mm length beam for a 10 g harvester, and a 130 mm beam for a 100 g harvester. Larger and smaller values result in beams that are shorter and longer, respectively, in relation to their mass. In the investigation of this parameter, we hold c_{Lw} constant at a value of 5. The result for a c_{ML} value of 46.5 kg/m^3 can be seen in figure 2.12. Figures 2.14 and 2.15 show the results for $c_{ML} = 364$ kg/m^3 and $c_{ML} = 5.69$ kg/m^3, respectively. We can see in these plots that generally, the power is increased as the c_{ML} value decreases. This result can be explained by investigating equation 2.58. With constrained frequency and system mass, as c_{ML} decrease, the thickness term (y) and curvature at the root (ϕ'') decrease. Their position in the denominator of 2.58 results in a net increase in the power output that, because of their squared nature, dominates the decrease caused by reduced modal mass. The net result being that beams which are long with respect to their mass will tend to have higher maximum possible power.

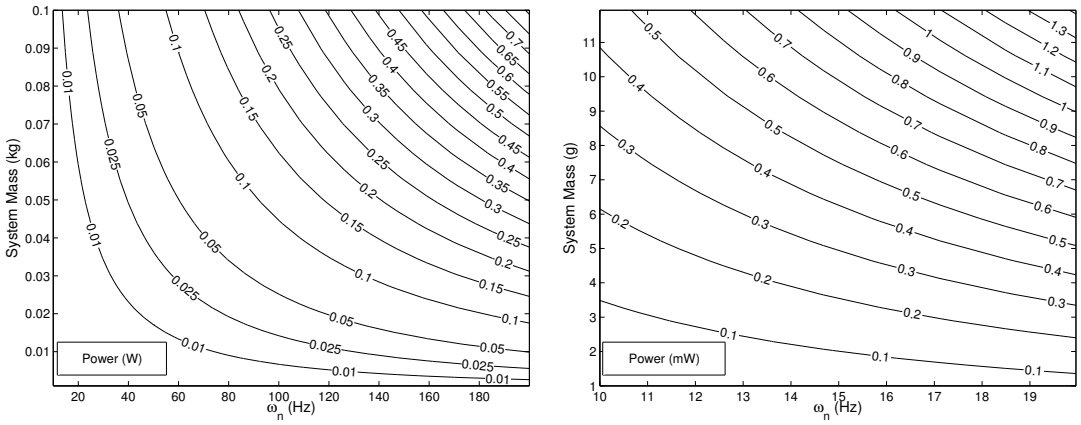

(a) (b)

Figure 2.14: Maximum power for $L/w = 5$ and $c_{ML} = 364$ kg/m^3. Beams that are shorter relative their the mass. (b) shows the results for systems of low mass and natural frequency.

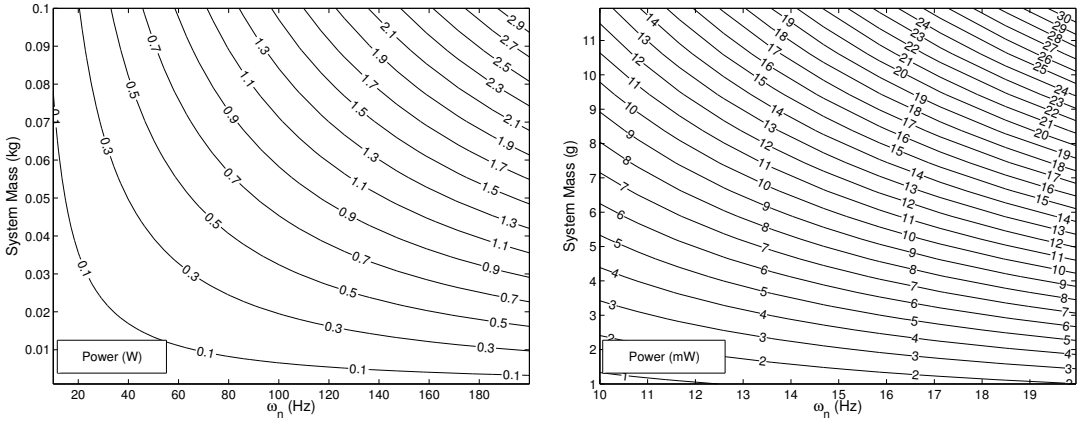

(a) (b)

Figure 2.15: Maximum power for $L/w = 5$ and $c_{ML} = 5.69$ kg/m^3. Beams that are longer relative their the mass. (b) shows the results for systems of low mass and natural frequency.

In order to validate the method of power prediction, we can compare the power predictions, normalized by peak input acceleration, to results existing in the literature. Erturk presents an experimentally validated power model for a bi-morph harvester with a simple resistive load (unrectified)[20]. He shows that for a beam with $c_{ML} = 158$ kg/m^3 and $c_{Lw} = 1.6$, the peak power output normalized by the acceleration input would be 23.9 mW/g^2 at the short circuit resonance. Note that no upper limit is presented for the acceleration amplitude, highlighting the importance of equation 2.55. As noted by Erturk, the RMS-based average power would be half of this peak value. In order to compare this result with our predictions, we must account for differences in power resulting from the rectifier in our model. To do this, we turn to two expressions developed by Guyomar for the average power of rectified and unrectified harvesting circuits [25]. The analysis in this work shows that when the ideal resistance is used, the ratio of maximum average power is:

$$\frac{P_{\text{rectified}}}{P_{\text{unrectifed}}} = \frac{2}{\pi} \tag{2.67}$$

Although the equation on which this is based may result in some error at high coupling due to the inphase assumption used in its derivation [81], the result is sufficient to make a comparison between our results. If our model is run using the same c_{ML} and c_{Lw} values, we obtain an average power output of 8.9 mW/g^2. When accounting for the rectifier and average power differences, Erturk's result would be 7.6 mW/g^2, a close match considering the estimate used to relate the rectified and unrectified systems.

2.5 Conclusions

Piezoelectric energy harvesting has seen continual modeling refinement over the previous decade of research. Despite this modeling, fundamental issues concerning the limits of the technology continue to limit our understanding of their capabilities. The maximum efficiency and power capabilities of any energy generation technology are needed to assess proposed designs in relation to what is possible. In this work, we present expressions for both the maximum possible power and efficiency for piezoelectric transducers.

We have shown that distinct differences exist in the predicted efficiency depending on the assumption used when considering work done on the excitation source by the harvester. This system level view of efficiency is critical in applications of energy harvesting where resonance cannot always be guaranteed, or where the host structure is unable to recover mechanical energy. There are however, important efficiency similarities between the open and short circuit resonances. The conservative and nonconservative analyses produced results with only slight differences in this range and in both cases the upper limit of efficiency is approximately 44% at resonance. In addition to presenting this limit, we have revealed an important distinction in the definition of efficiency depending on the nature of the excitation source. We developed an expression for this nonconservative case efficiency, and showed clear differences in the results when compared to a previously developed efficiency expression. We have also shown that in either case, peak efficiency occurs when the system is operated off resonance, halfway between the open and closed circuit natural frequencies.

While many models exist that predict power from an energy harvester, they

all depend on the magnitude of the excitation acceleration. Using the constitutive equations, we were able to relate this acceleration magnitude to the stress in the piezoelectric elements of a harvester. The primary result of this analysis was an equation that provided a limit on base acceleration magnitude for safe operation. Using this equation, we developed an expression for the maximum possible harvester power for a given harvester design. We then used this expression to develop the maximum possibly harvested power across a wide range of excitation frequencies and system masses. We showed that generally, beams should be designed with low length to width ratio, and a high ratio of length to cubed root of mass.

With the expressions and results presented in this paper, we have given engineers a benchmark on which current and future concepts may be compared. Additionally, the maximum power plots of this paper can be used as a reference to quickly estimate the absolute maximum power one might achieve for a given system mass and input frequency.

CHAPTER 3

THE CASE FOR AVIAN WILDLIFE ENERGY HARVESTING

3.1 Introduction

Energy storage and battery life have always been a major issue for wildlife tracking and bio-logging devices. For long deployments, even modern devices have a large portion of their mass dedicated to batteries. This need for in-situ energy generation was recognized as far back as 1973 [54] and has seen continued development with solar powered bird tags with masses low as 5g [48]. While solar power can supplement the energy budget, there are various applications where solar power is not an option. For instance, Microwave Telemetry Inc, a wildlife tag manufacturer has a number of solar powered avian bio-logging tags available, yet their website notes that solar powered tags are not suitable for many species because of preening habits or time spent in areas without sunlight [46]. Additionally, tags used in the marine environment or on nocturnal animals often do not have sufficient solar exposure to make photovoltaics viable and must be battery powered [47][90][32]. It is clear that alternate types of ambient energy harvesting need to be considered to supplement the energy budget of bio-logging devices. In this work we consider how the an animal's kinetic energy might be converted to electric energy to power a biological monitoring tag. This method of energy conversion, otherwise known as vibrational energy harvesting, could be applied to various animals, but we focus here on birds. We will show that even when applied on birds, where system mass is severely constrained, there is sufficient power available to warrant their use in many cases.

Vibrational energy harvesting refers to the method of converting mechanical energy to electrical energy by some means of transduction. Recently, devices using piezoelectric materials have seen significant research due to their simple mechanical design and high voltage outputs. The size and simplicity of these devices makes them an ideal candidate for wildlife energy harvesting. A piezoelectric material develops an electric field when under stress. By connecting an electrical harvesting circuit to these materials, the energy developed by an applied stress can be used to charge batteries or capacitive elements. While work continues on advanced design and circuit concepts for these devices, a standard cantilevered piezoelectric harvester design and associated energy harvesting circuit are shown in figure 3.1. When a base acceleration is applied to this device, the strain induced in the beam from the vibration is converted to electrical energy by way of the piezoelectric material. The current that develops in the harvesting circuit is rectified, and through the use of a filtering capacitor, is converted to a nearly DC output. The circuit powered by the harvesters is often modeled as a resistive load in parallel with the filtering capacitor. It is of particular importance that these devices be excited at their resonant frequency as strain, and therefore power, is reduced when operating at off-resonant frequencies [89] [81]. In this work we will show the compatibility of the excitation requirements of vibrational energy harvesters with the accelerations seen in flight on two bird species, the Western Sandpiper (*Calidris mauri*) and Swainson's Thrush (*Catharus ustulatus*).

While the concept of vibrational energy harvesting on birds is new, it has been demonstrated on animals as small as several grams, such as Tobacco Hornworm moths (*Manduca sexta*) and Green June Beetles (*Cotinis nitida*) [67] [6]. Flying animals seem to be an ideal candidate for vibrational energy harvesting

devices, as their flapping gate is typically regular and cyclic in nature. For instance, it has been shown that over a wide range of flight speeds, the flapping frequency of cockatiels (*Nymphicus hollandicus*) does not change by more than approximately 20% [28]. Moreover, assuming a relatively sinusoidal vertical acceleration profile with no lift during wing upstroke, we should expect acceleration amplitudes on the order of 1 g for level flight and constant forward speed. The consistent frequency and high acceleration amplitude make bird flight an ideal candidate as an excitation source for vibrational energy harvesting.

To assess the viability of avian energy harvesting, we first investigate the energy available and the quantity that can be collected without adversely affecting the host. The method for this estimation, initially developed by Shafer and Garcia [77], is reviewed and refined here with updated coefficients to serve as a basis for consideration of energy harvesting on flying birds. These initial estimates serve as a safe ceiling of what the animal is capable of supplying without adverse effects. Such an understanding is critical in the assessment of the practicality of any energy harvesting application. We look at the energy output from flying birds, and using power models, develop limits on the power that might be harvested safely without negative effects on the bird's overall energy

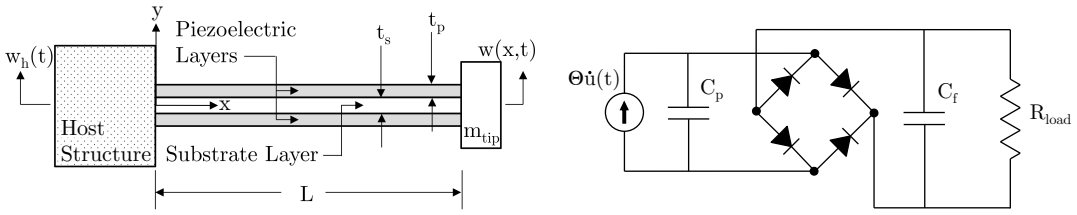

(a) Piezoelectric energy harvesting device (b) Energy harvesting circuit

Figure 3.1: (a) Fully laminated bimorph piezoelectric energy harvester. (b) Circuit diagram for the standard piezoelectric harvester signal rectification and dissipation. Piezoelectric devices are often modeled as a current source in parallel with a capacitor

budget. We then present analysis of acceleration measurements taken on two species of flying birds. Here we further analyze the testing results preliminarily presented by Shafer et al. [79] to understand the dynamics of the vertical component of acceleration. . Using spectral analysis, we are able to show consistency in flapping frequency and small effects on flapping frequency as a result of payload increases. We then use recent estimates for the power limits of piezoelectric energy harvesters to understand the amount of power that would likely be generated based on system mass and frequency. These power results are then contrasted against the power requirements of commercially available microcontrollers to show that in many cases more power can be generated than is required for microcontroller operation.

3.2 Avian Energy Harvesting Limits and Potential

The available power for harvesting from any animal is closely related to their energy expenditure. For birds, the power required for flight can be calculated from parameters such as wing aspect ratio, wing span, and mass. By first calculating the power required in flight by a laden bird, and subtracting from it the power required by an unladen bird, we can develop an estimate of the excess power available for harvest. For powered flight, two main power models exist in the literature [66, 59]. We use Pennycuick's model here due to its continued refinement [56, 61, 62]. The details of this model, including equations and constants are presented in A. In this power model, the energy expenditure is decomposed into five major categories shown in table 3.1. By calculating the power required for flight with and without a payload, we are able to make an estimate of a bird's excess energy potential, assuming this to be the power

available for harvest.

Table 3.1: Power types for bird flight

Power Type	Description
Parasitic (P_{par})	Drag from body
Induced (P_{ind})	Momentum transfer to air (lift)
Profile (P_{pro})	Driving wings forward through flow
Basal Metabolic (P_M)	Caloric overhead
Cardio/pulmonary	Cardiovascular/Breathing

The equations for each of the types of power listed in table 3.1 are shown in A. All five power contributions shown in table 3.1 depend either directly or indirectly on the mass of the bird. Of those five, only two would not be affected by an attached payload on the bird. The first of these is the parasitic power resulting from drag on the body of the bird. While a tag may increase the drag on the bird [52], in this estimate we neglect this effect since different tag designs will have varying drag coefficients and we wish to focus here on harvested mechanical power. The other parameter not affected by payload would be the metabolic power required to maintain bodily functions.

The induced power is that which is required for momentum transfer in order to create lift. This power contribution would clearly be affected by a payload. The profile power is necessary to counteract the drag over the wings as they move through the flow. While this might seem to not be dependent on payload mass, it is estimated using the minimum power flight speed of the bird, which does depend on the total flown mass of the bird and payload. Finally, the cardio/pulmonary power is taken as a 10% increase when summing the others. Thus, it too depends on the payload mass. With this power model, we now need to know the payload capabilities of the birds in flight.

Birds are capable of flying for short periods with significant payloads. Marden experimentally showed that many bird species are able to take off with a payload of up to 16% of their flight muscle mass [45], which corresponds to about 5% of total body mass assuming that flight muscles are 25-35% of total body mass. While able to fly, these birds might not survive long in the wild with such a payload. Traditionally devices attached to birds have been limited by mass. New research suggests that energy output might be an alternate metric [87]. The mass limit suggested by the US Geological survey for migratory bird tags is 3% of the bird's mass [86]. Others have proposed values in the range of 3-5% [30], but there have been notes that 5% may be conservative for small birds and excessive for large birds [27]. Naef-Daezner et al. showed that the Coal Tit and Great Tit (*Periparus ater* and *Parus major*) were able to carry payloads of between 3-5% of their mass with no effects on survivability [50]. These values suggest that using a conservative payload mass of approximately 4% of the animal's mass would be adequate for estimation, and that the animal should have sufficient energy to carry such a payload without long-term effects.

With a payload limit of 4% of the bird's mass and a model for power in flight, we are able to determine the power that could be safely harvested from the birds. The total power required for flight by an unladen bird would be [59]

$$P = 1.1\,(P_{par} + P_{ind} + P_{pro} + P_M) \tag{3.1}$$

Note that the 1.1 factor is included to account for the cardio/pulmonary power component. We denote the fraction of the bird's unladen mass (m) attributed to payload as 'q' such that

$$m_l = q\,m. \tag{3.2}$$

The laden mass term (m_l) can be summed with the unladen mass (m) and

the resulting total flow mass used in the expressions for power (A). After simplifying, the resulting power required for flight with a payload is [77]:

$$P = 1.1\left[P_{par} + (1+q)^2 P_{ind} + (1+q)^{3/2} P_{pro} + P_M\right] \tag{3.3}$$

Taking the difference between equations 3.3 and 3.1, and using the maximum allowable ($q_{max} = 4\%$) as the laden mass fraction, gives an estimate of the excess longterm power output for the bird. We designate this as the harvestable power, P_H.

$$P_H = 1.1\left[((1+q_{max})^2 - 1)P_{ind} + ((1+q_{max})^{3/2} - 1)P_{pro}\right] \tag{3.4}$$

We can see in this equation that only those power terms which depend on the payload remain in the estimate of harvestable power. Furthermore, the induced power and profile power terms are only a function of the wing span, aspect ratio, and mass (see A). With averages of these parameters readily available for a variety of species, we are able to develop a general estimate of the harvestable power from birds.

3.2.1 Harvestable power across species

With a harvestable power expression (equation 3.4) and an upper limit of payload ($q_{max} = 4\%$), we can calculate the sustainably harvestable power for any species for which we have sufficient data. Poole provides a list of wing areas and weights for 149 North American birds, only a few of which are different sexes of the same species [64]. Although Poole does not report wingspan, we can interpolate the span of these birds using the ranges of mass and span listed in a Cornell Lab of Ornithology database [15]. Sixteen birds listed in the

Poole dataset were not listed in the Cornell dataset, and thus not included in this study. In addition to this dataset, Pennycuick provides wing area and span for 36 other species for a total of 169 birds.

As shown in Appendix A, the induced power (P_{ind}) depends on the flight speed of the bird. It has been shown that birds tend to prefer to fly at that speed which minimizes total power output (V_{mp}) [58].

$$V_{mp} = \frac{0.76k^{1/4}(mg)^{1/2}}{\rho^{1/2}(S_b C_{Db} S_d)^{1/4}} \tag{3.5}$$

This flight speed depends on the mass of the bird (m), acceleration due to gravity (g), air density (ρ), frontal body area (S_b), circular area swept by the wings (S_d), and two coefficients (C_{Db} and k). The body drag coefficient (C_{Db}) is typically set to a value of 0.1 [59][60]. The empirical induced drag factor (k) has been the subject recent research. Analytic predictions for the minimum power velocity have been recently shown to match observed flight speeds for various species if k set to 0.9 [60], as compare to previous estimates of 1.2 [59]. The minimum power flight speed for each of the birds in the dataset was calculated and used in conjunction with equation 3.4 to develop a harvestable power estimate across species. The result of this analysis can be seen in figure 3.2

Figure 3.2 provides an initial estimate of the power available for harvest across a large number of species. As shown in the figure, this power has a general exponential relationship with the mass of the animal. A regression analysis provides the relationship between mass and harvestable power that is plotted as well in figure 3.2 . The equation of this relationship is [77]:

$$P_H = 0.565m^{1.043} \tag{3.6}$$

The available power resulting from this expression gives an initial estimate of the total excess power output capabilities. This would be the total amount of

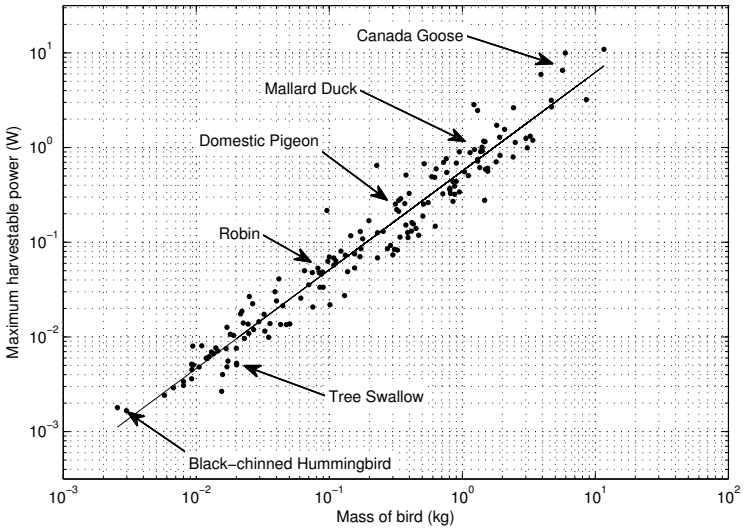

Figure 3.2: The maximum power that can be harvested (P_H) from birds across mass without causing significant fatigue assuming the 4% laden mass limit.

excess power available, and includes both the power required to carry the transducer and power to be harvested. Using the specific power of the transducer, we can account for the power required to carry the device, and obtain a better estimate of the power that could be harvested.

To account for the energy required to carry the harvester and payload, we must distinguish between the power *required* for flight (P_r) and the maximum *allowable* output power (P_a). The power required for flight is simply the result of equation 3.3, where the total flown mass is used to calculate the induced, and profile power. This total flown mass is the sum of the masses of the bird, harvester, and any additional payload such as electronics, batteries, etc. The maximum allowable power output is expressed by equation 3.3, using the 4% laden mass limit (q_{max}). The required and the allowable powers can be expressed as

follows:

$$P_r = 1.1\left(P_{par} + (1+q)^2 P_{ind} + (1+q)^{3/2} P_{pro} + P_M\right) \tag{3.7}$$

$$P_a = 1.1\left(P_{par} + (1+q_{max})^2 P_{ind} + (1+q_{max})^{3/2} P_{pro} + P_M\right) \tag{3.8}$$

The difference of these expressions is

$$P_h = 1.1\left(\left[(1+q_{max})^2 - (1+q)^2\right] P_{ind} + \left[(1+q_{max})^{3/2} - (1+q)^{3/2}\right] P_{pro}\right) \tag{3.9}$$

Notice that we distinguish this practically harvestable power (P_h), which accounts for the mass of the payload and harvester, from the theoretically harvestable power (P_H), which depends only on q_{max}. When calculating this practically harvestable power, the P_{ind} and P_{pro} terms are calculated for the unladen bird, with the q term indicating the fraction of the total flown mass beyond the unladen mass. If we assume that the energy harvester has some specific power ($\bar{P}$, power per unit mass), then the total laden mass depends on the amount of available power. Introducing this dependency insures the harvester is neither over, nor undersized for the power available for harvest. For a given harvester specific power $\bar{P}$, a transducer sized specifically to harvest power P_h would have a mass of $P_h/\bar{P}$. Including with this a mass allocation for payload components (m_p) like electronics, batteries, etc., which are not included in the harvester, the total laden mass of the system would be:

$$m_l = m_p + \frac{P_h}{\bar{P}} \tag{3.10}$$

This expression can be used with equation 3.2 to solve for the laden mass fraction (q) in terms of the specific power, the harvestable power, and the payload mass. Substituting this result into equation 3.9 and rearranging results in the

following polynomial expression:

$$At^4 + Bt^3 + Ct^2 + E = 0 \tag{3.11}$$

$$t = \sqrt{P_h/\bar{P} + m + m_p} \tag{3.12}$$

where

$$A = 1.1P_{ind}/m^2 \tag{3.13}$$

$$B = 1.1P_{pro}/m^{3/2} \tag{3.14}$$

$$C = \bar{P} \tag{3.15}$$

$$E = -1.1(1 + q_{max})^2 P_{ind} - 1.1(1 + q_{max})^{3/2} P_{pro} - \bar{P}(m + m_p) \tag{3.16}$$

This forth order expression (equation 3.11) has the following closed form solution for the practically harvestable power P_h:

$$P_h = \bar{P}\left(t^2 - m - m_p\right) \tag{3.17}$$

where

$$t = \frac{-B}{4A} + \frac{\pm_i W \mp_j \sqrt{-(3\lambda + 2y \pm_i \frac{2\beta}{W})}}{2} \tag{3.18}$$

The terms W, λ, y, and β are all components of the solution that depend on A, B, C, and E and are shown in Appendix B. The i subscripts for the '$\pm$' signs indicate that they change sign independently of the j subscript on the '$\mp$' sign. With this solution we are able to estimate the practically harvestable power from a bird.

To make the estimate of practically harvestable power using equation 3.17, we need the same set of parameters required for the estimate of P_H provided by Poole, Cornell Laboratory of Ornithology and Pennyquick. When equation 3.17 is used in conjunction with these datasets, we can develop an estimate of harvestable power across a range of species and transducer specific powers.

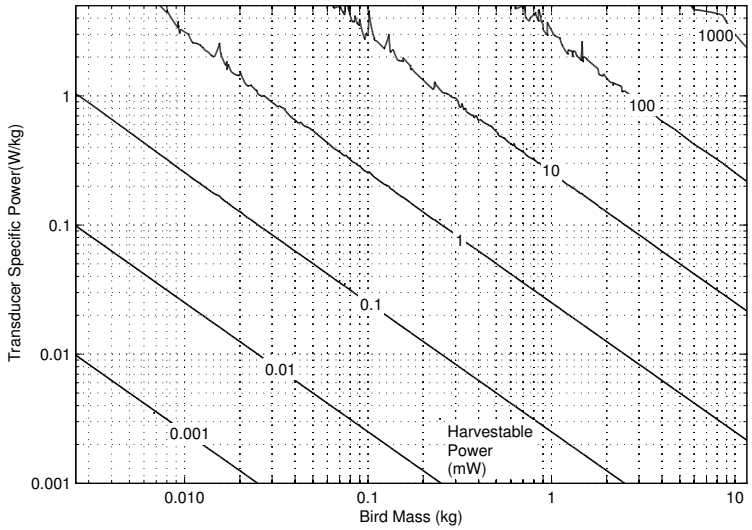

Figure 3.3: Harvestable power from birds across mass and transducer specific power using the 4% mass limit.

In figure 3.3 we see contour lines of harvestable power plotted against both transducer-specific power and bird mass. The peaks in the contour lines are a result of the fact that the analysis is based on actual bird measurements. Some birds are more efficient due to differing aspect ratios and as such we would expect the available power to not be solely a function of bird mass. These peaks appear smaller as the harvestable power decreases because of the linear scaling of the contours.

Generally, there is a dependence of the harvestable power on mass that can be seen in figure 3.3. The range of transducer specific power was selected to extend both above and below the expected specific power of a piezoelectric energy harvester. A harvester sized to weigh a few grams and operate at approximately 10 Hz would expect a specific power of less than approximately 0.5 W/kg [76]. We can see in figure 3.3 that a transducer with a specific power on the order of 0.05 to 0.5 W/kg may safely harvest power on the order of 20-200 μW for the smallest of birds on the order of 10 g, and 20-200 mW for the largest of birds on

the order of 10 kg. Even for smaller birds, these results are sufficient to power a variety of microcontrollers that might be used on a bio-logging tag. While many currently available microcontrollers operate with power requirements of a few milliwatts, some modern units employing FRAM are able to operate at speeds of 1MHz with as little as 180μW [11]. These results show us that vibrational energy harvesting is a viable option when considering the development of in-situ power generation for a bio-logging device. We have shown that there is sufficient power available without gross additional energy expenditures by the host. We must now examine the dynamics of flying birds in relation to those of vibrational energy harvesters.

3.3 Acceleration measurements on freely flying birds

3.3.1 Flight test overview

After determining the quantity of available energy from the host animal, it is important to determine the compatibility of the transducer technology with the animal's behavior. For solar or thermal electric energy harvesting, this would entail a study of time spent in the sun, or average temperature differences, respectively. For vibrational energy harvesting, the compatibility of the technology stems from the nature of the flight accelerations. There are various broadband vibration energy harvesters under development that are capable of harvesting energy from a range of input frequencies, but their size and complexity preclude their use on small animals such as birds [84]. The more practical devices rely on excitation at a single primary resonant frequency. This means that it is impor-

tant that the birds maintain a fairly uniform flapping frequency for maximum power harvesting. There is evidence that birds have a preferred flapping frequency across a range of flight speeds. As previously mentioned, Hedrick et al. have shown that there is only a 20% shift in flapping frequency across the range of flight speeds for cockatiels (*Nymphicus hollandicus*) [28]. Furthermore, there is evidence that birds consistently fly near the minimum power velocity [58]. These two pieces of information suggest that we might expect a fairly uniform fundamental flapping frequency over long periods, but we must understand frequency modulations over short time scales and the general frequency content of the bird's flight motion to better assess the viability of vibrational energy harvesting.

We conducted a series of tests on two bird species in a bird flight tunnel at the Advanced Facility for Avian Research at the University of Western Ontario. The test section of this tunnel is 2 m long, with an octagonal cross section 1 m high and 1.5 m wide [24]. The birds were outfitted with data-logging devices capable of measuring the three orthogonal components of acceleration at 200 Hz for 50 s. The data loggers consisted of a Texas Instruments MSP430F2274 microcontroller and a Bosch BMA150 3-axis digital accelerometer. The acceleration measurements were stored to local flash memory in the microcontroller until they could be offloaded to a computer after each test. The devices weighed 0.44 g and can be seen in figure 3.4(a) . The data loggers were held in place on the birds using a small plastic harness that was either temporarily glued or tied to the bird as shown in figure 3.4(b). When tied, Rappole-style leg loops were used [65]. When glued, some of the feathers beneath the loggers were clipped in order to ensure a more rigid connection. These carriages weighed 0.23 g and allowed the logging device to be easily removed from the bird after each trial so

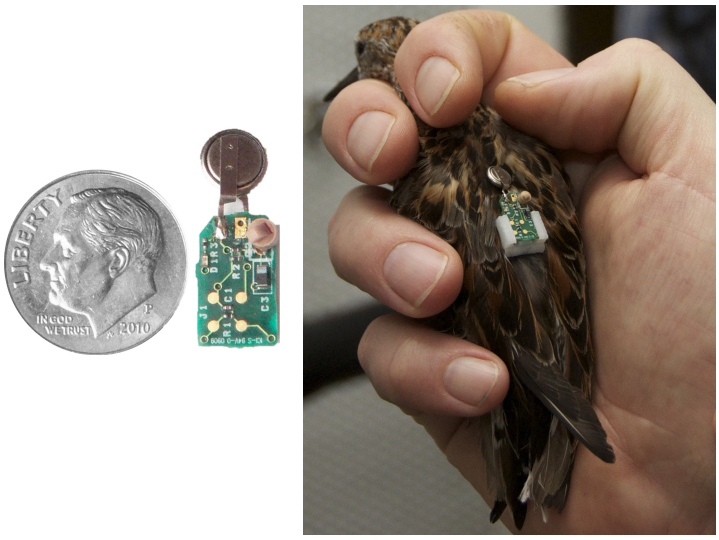

(a) (b)

Figure 3.4: (a) Accelerometer tag with U.S. dime for scale. (b) Accelerometer tag mounted to western sandpiper.

that the tag could be removed for data download and then quickly replaced for another test.

The two species of birds tested with these acceleration logging devices were the western sandpiper (*Calidris mauri*) and the swainson's thrush (*Catharus ustulatus*). One western sandpiper (WS) was flown and weighed 30.1 g. The two tested swainson's thrushes weighed 40.8 g (ST1) and 41.0 g (ST2). These birds were captured under a Canadian Wildlife Service permit (CA-0256) and the experimental procedures were approved by the University of Western Ontario Animal Use Subcommittee (Protocol 2010-216). The thrushes tended to perform better in the tunnel, thus providing more data than did the sandpiper. The procedure for the tests was as follows: prior to testing, the birds were outfitted with the previously mentioned plastic harnesses. They were returned to their enclosures and allowed to become accustomed to the apparatus. At the beginning of each trial one of the acceleration logging devices was inserted into

the harness. The tunnel was then brought up to 10 m/s equivalent wind speed, which had previously been shown to be a good speed for flight with these birds [24]. The logging device was then turned on and the bird was released into the tunnel. The bird then flew in place in the tunnel until the memory on the loggers was full (50 s) or the bird landed. There were various instances where the bird would land before the 50 s. When this happened, the bird was either prompted to fly again or recaptured to begin another test.

3.3.2 Results

The trials from this testing have been broken up into three groups to highlight different aspects of the flight acceleration spectrum. The first group of results consists of three trials from the sandpiper flights. These three trials all have similar frequency content and show the relative consistency of flapping frequency in time. The second group consists of two trials from ST1. These trials show that there can be small fluctuation in the primary flapping frequency for a given species, but there is overlap in the average power spectral density peaks to allow for a single targeted resonance. The third group consists of four trials from ST2 highlighting the relatively small effects of payload on the flapping frequency. We concentrate our analysis on the z-component of acceleration, as shown in figure 3.5. The 3-axis accelerometer results showed this direction contained the highest acceleration amplitudes, and as such is the likely candidate for energy harvester excitation. Spectrograms of the results for each of the three groups are shown in figures 3.6 - 3.8. These spectrograms are the results of dividing the acceleration signals into a series of discrete windows and performing a short-time Fourier analysis on each window. The spectrograms presented here use

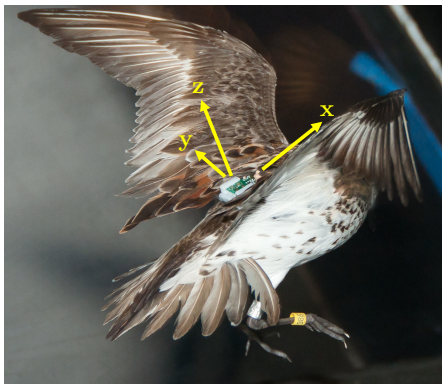

Figure 3.5: Western sandpiper in flight with acceleration logger. Accelerometer axes shown in yellow. X-direction points forward, Y-direction is toward left wing, and Z-direction is up off the back.

a 3 s Hamming window with 50% overlap. This represents approximately 36 flapping cycles per window, given the 12 Hz signal present in most of the data. In addition to these spectrograms, their time averages have been calculated to give a sense of the general longterm frequency content of the flight accelerations. These averages are plotted adjacent to the spectrograms in figures 3.6-3.8.

A spectrogram of the first group of results can be see in figure 3.6(a). In this figure the three WS trials have been stitched together to form one continuous sample for ease of presentation. In figure 3.6(a) we can see that the majority of the power in the signal, shown in a lighter shade, is focused around 12 Hz and does not seem to vary in time. In this spectrogram we can see there is some amount of frequency modulation, such as between $60 < t < 80$ s, but generally the flapping frequency is consistent. The second harmonic is visible in this figure as a lighter band near 24 Hz, indicating a higher frequency that could be used for harvester excitation. Despite the approximately 10dB reduction from the fundamental frequency, the observation is important given that designing a resonant piezoelectric energy harvester to be low mass and robust

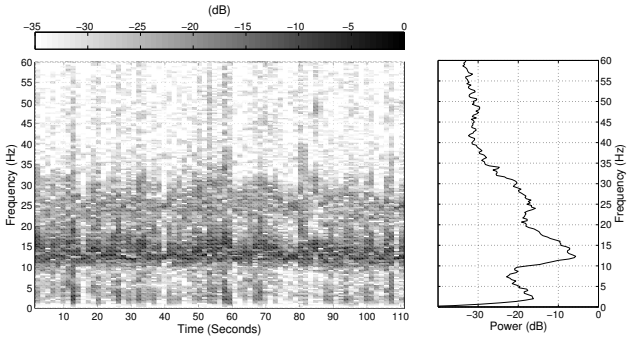

(a) Western sandpiper spectrogram (b) Average PSD

Figure 3.6: Spectral results of z-component acceleration for western sandpiper trials. Notice the relatively consistent fundamental frequency near 12Hz.

with a low resonant frequency can be challenging. The time averaged PSD for this trial shown in figure 3.6(b) shows that for this bird, there is some broadband frequency content between 12 and 14 Hz, but that there is a peak near 12 Hz.

The results of the first set of thrush trials can be seen in figures 3.7(a) and 3.7(b). These two trials are the results for the same bird, ST1, carrying the same logger and show the types of small variations we might expect in flight from a freely flying bird. Figure 3.7(a) shows a flapping frequency that starts near 15 Hz for the first 10 seconds before decreasing slightly, and then increases back to 15 Hz in the last 4 seconds of the trial. During the initial portion of this trial, the bird was moving from the rear of the tunnel to the front and thus the frequency variations seen here likely represent the extreme of what might be expected for steady flight. The variation in flapping frequency is evident in the lack of a clear peak in the average PSD for this trial shown 3.7(c). We can see in this plot that there is significant power for this trial between 12 and 16 Hz with a slight peak near 14 Hz. This can be contrasted against the results for trial two of ST1 in figure 3.7(b). In this trial, we see a spectrogram that has a series of peaks that appear more constant in time. Additionally, we see that the average PSD for this

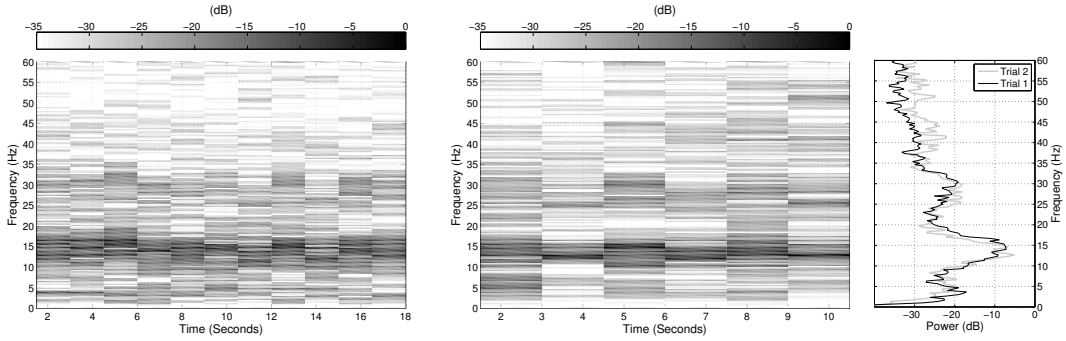

(a) Trial 1 spectrogram (b) Trial 2 spectrogram (c) Average PSD

Figure 3.7: Spectral results of z-component acceleration for swainsons thrush 1. Two trials shown highlighting small shifts in flapping frequency from 12 Hz.

trial (3.7(c)) has a peak at 12 Hz. Taken together, these trials suggest that this bird has a fundamental flapping frequency near 12 Hz but is able to up-regulate its frequency on the order of 25%. This is consistent with the measurements taken by Hedrick et al. on variation in cockatiel flapping frequencies with varying flight speeds [28].

The final set of trials comparing flights with and without a 2.052 g payload (an addition mass beyond the mass of the acceleration logger) on ST2 (figure 3.8) reveals fundamental frequencies near 12 Hz that do not vary in time. Each of these spectrograms contain data from three individual flights that have been stitched together. In the flights without payload (figure 3.8(a)), we see very consistent power at 12 Hz with a small amount of power in the second harmonic near 24 Hz. While the fundamental frequency appears nearly identical in the trial with payload (figure 3.8(b)), there is more evidence of power in the higher harmonics. These results are shown clearly in the average PSDs for these trials shown in figure 3.8(c). In this figure we see that the bird with and without the 2 g payload had a fundamental frequency of 12 Hz. There appears to be a slight increase in the fundamental frequency in the flight with the payload of approx-

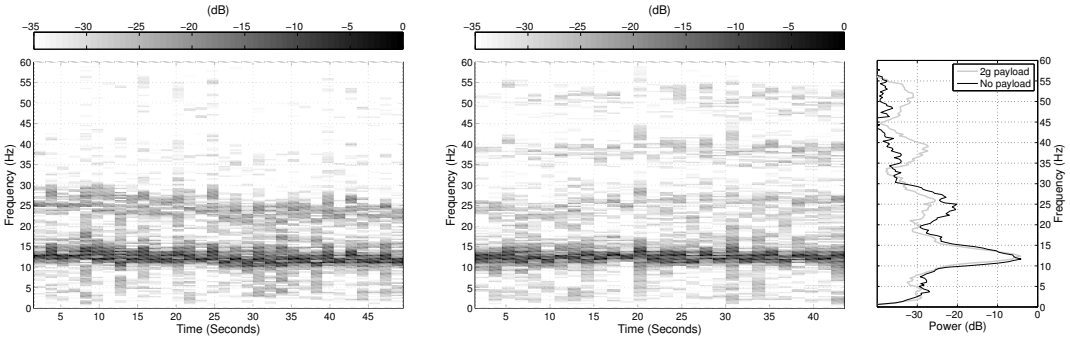

(a) No payload trial (b) 2.052 g payload trial (c) Average PSD

Figure 3.8: Spectral results of z-component acceleration for swainsons thrush 2. Two trials shown highlighting deviations in fundamental frequency for when significant payload is attached.

imately 0.7 Hz, but more trials would be needed to determine if this is a statistically significant shift. The increase in the higher harmonics for the payload case indicates that the bird maintains its fundamental flapping frequency, but adjusts its flapping in a way that changes the shape of the acceleration waveform. This may indicate a slight change in the flapping gate of the bird under load. The 2.052 g payload, along with the 0.64 g data logger mass represents almost 7% of the mass of the 41 g bird. For comparison, this is approximately double the previously mentioned 3-4% limit set by the USGS. This added mass would be considered an unacceptable payload for a bird released in the wild. The critical result though, is that there does not appear to be a significant effect on the fundamental flapping frequency even from this highly significant payload.

The results of this acceleration testing affirm that the flapping frequency is consistent, and that it is not significantly affected by substantial payloads. It is therefore reasonable to assume that knowledge of the unladen flapping frequency is sufficient when designing a resonating energy harvester. These tests indicate that if normal wingbeat frequency targeted for energy harvester design, we should expect a similar excitation frequency when the device is deployed

and significant time in flight at that frequency. Given that the nature of the bird's acceleration pairs well with the resonant nature of the transducer under consideration, the remaining consideration deals with the specific power of the transduction method.

3.4 Piezoelectric energy harvesting potential vs. power requirements

Based on the results of the previous two sections, we know that there is sufficient energy available for harvest from the motion of a flying bird, and that the nature of the acceleration waveform lends itself to resonant energy harvesting. In order to understand the amount of power that might actually be harvested by a piezoelectric device attached to a bird, we must have a better understanding of the relationship between harvester mass, frequency, and power output. The specific power from a piezoelectric energy harvester depends heavily on the design, the size, and the frequency at which the device operates. For this reason the power output of these devices has been hard to quantify generally. Recently, we proposed a baseline for these devices based on an optimization of piezoelectric material thickness ratio and the ultimate strength of the piezoelectric element that we will use here to estimate specific power [76].

The power limit estimated depends on the relationship between excitation acceleration magnitude and the maximum allowable stress in the piezoelectric transducer. Based on this, and a thickness ratio optimization [74], we developed a set of harvester designs for a variety of mass and excitation frequencies. The power outputs from each of these designs is reported in contours plotted

against harvester mass and resonant frequency. The maximum power reported depends on the material chosen, as well as two geometric parameters. These geometric parameters relate the width of the harvester to its length and the length to the mass of the system.

This power limit has been recomputed here for a range of masses and frequencies applicable to many bird species. The results of this analysis are shown in figure 3.9. This analysis was done for a beam aspect ratio (length/width) of five and a mass scaling constant (mass/length^3) of 45.6 kg/m^3. The piezoelectric material used in the analysis was Navy Type II and substrate material was assumed to be stainless steel, two standard materials in piezoelectric energy harvesters. The material properties considered are shown in table 3.2.

Table 3.2: List of material properties

	Value	**Unit**	**Name**
ρ_s	7916.5	kg/m^3	Substrate Density
ρ_p	7800	kg/m^3	Piezoelectric Material Density
E_{sx}	212	GPa	Substrate Modulus
E_{px}	67	GPa	Piezoelectric Material Modulus
e	-12.73	C/m^2	Piezoelectric Stress Constant
ϵ^s	1.59e-8	C/m^2	Piezoelectric Permittivity
σ_{max}	76	MPa	Piezoelectric Ultimate Strength

In figure 3.9, we can see that the most power we might develop from devices on the scales that could be applied to flying birds is on the order of a few milliwatts. There is a strong dependence on mass, which would need to be less than 4% of the mass of the bird. Using the known mass and flapping frequency of the tested thrushes as an example, we can use 3.9 to estimate the power that might be developed from a piezoelectric energy harvester. We saw in section 3.3 that the thrushes we tested weighed approximately 40 g and tended to flap

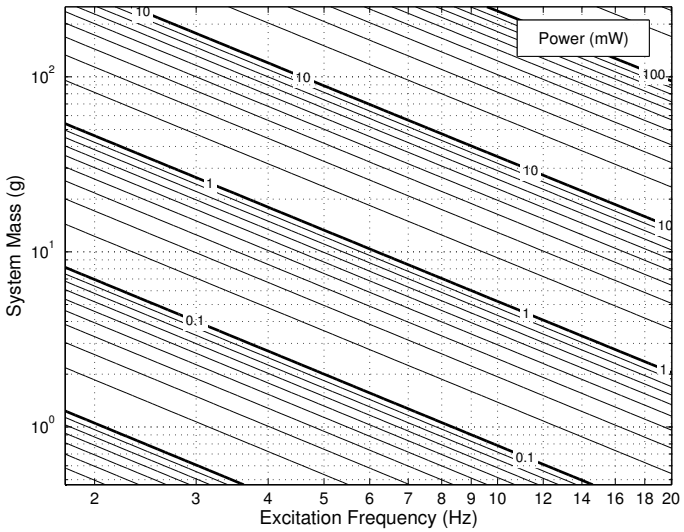

Figure 3.9: Maximum power available from a fully covered bi-morph type piezoelectric vibrational energy harvester based on maximum allowable stress with no factor of safety applied.

at 12 Hz. Using the 4% mass limit discussed in section 3.2, an energy harvester system for this bird should weigh no more than 1.6 g. According to figure 3.9, a 1.6 g harvester operating at 12 Hz could produce up to approximately 250μW. As this is the power developed immediately prior to failure, a factor of safety would need to be applied to insure survivability of the device. If we assume a factor of safety of four, we would expect no more than 62μW of power. This is a significant amount of power when compared to the power requirements of the of the microcontrollers that would be used on these bio-logging devices. Any excess power could be used to charge a capacitor that could be used during RF transmissions.

In table 3.3 we have compiled a list of the power requirements for a variety of microcontrollers that might be used on such a system. The devices all have power requirements on the order of a few hundred microwatts, with the lowest capable of operating at 1MHz as low as 180 μW. The 62 μW that we might expect

Table 3.3: Power consumption for various microcontroller devices

Manufacturer	Model	Active power @ 1MHz (mW)	Low Power Mode (μW)
Texas Instruments	MSP430F2XX	0.44	0.22
	MSP430FR5X	0.18	0.18
Atmel Corporation	ATtinyX4A	0.38	0.18
	ATtinyX61/V	0.54	0.18
	ATmega165	0.39	0.18
Microchip	PIC24F16KL402	0.63	0.054
	PIC24FV16KM204 F	0.36	0.045

from the swainson's thrush is not sufficient to directly power these devices at 1 MHz, but the current draw on most microcontrollers is linearly related to the clock frequency. For example, operating the MSP420FR5X series microcontroller at a clock frequency of 250 kHz would require 45 μW of power, and thus could be directly powered by the piezoelectric energy harvester. Furthermore, bio-logging tags operate at very low duty cycles and are often in active power mode for a total of only a few seconds per day. Power harvested when the tag is in a sleep mode would be stored on a battery or capacitor for use during periods of operation. Given these power results, it is evident that even birds as small as a thrush could use a piezoelectric energy harvester to generate sufficient power in flight to operate a bio-logging device.

3.4.1 Powering a microcontroller

If we consider larger birds on the order of 100-500 g, the potential energy harvesting capability for a piezoelectric device is far beyond the operating needs of a small microcontroller under limited-duty-cycle operation. For example, figure 3.9 suggests an average pigeon weighing 320 g [15] and flapping at 7 Hz

[55] could generate 375 μW of power, assuming the previously mention factor of safety of four on the harvester power. This would be sufficient to run a number of the microcontrollers in table 3.3 at 1 MHz, with at 100% duty cycle. For many reasons, the energy harvester would not necessarily be producing power when the tag needs to be in active mode. Thus, it is necessary to store the energy harvested over the course of each day so that it is available when device is in operation. To understand the relationship between harvester power, power consumption, and the duty cycles of each, we can investigate the energy balance of the system.

To first order, the energy consumed by the system is related to the ratio of the power consumed by the microcontroller during its low (P_{low}) and active (P_{act}) power modes. An example system with energy budgeting for wireless communication shown in section 3.4.2. For the majority of the devices shown in table 3.3 the ratio of P_{low}/P_{act} is on the order of 10^{-3}. Using this ratio, we can develop an estimate of the required ratio of power generation to power consumption based on the following estimates of energy consumption (E_c) and harvested energy (E_h) :

$$E_c = [P_{act}D_{act} + P_{low}(1 - D_{act})] \times T \tag{3.19}$$

$$E_h = P_{gen} \times D_{gen} \times \eta_{storage} \times T \tag{3.20}$$

The D term in these expressions represents duty cycle and $\eta_{storage}$ is the conversion efficiency from the harvested energy to the energy stored. The energy storage media may be devices such as batteries or capacitors. The subscripts act, low, and gen denote terms for active mode, low power mode, and power generation, respectively. We distinguish P_{gen} from the previously used P_h, because this analysis is valid for other forms of power generation besides vibration power

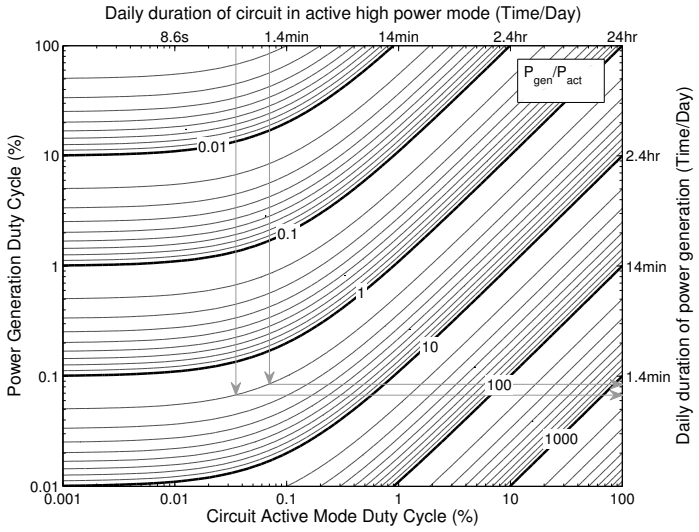

Figure 3.10: Required ratio of generated power to active microcontroller power across power generation and active mode duty cycles. Example shown for 30-60 s (0.035-0.07% duty cycle) with a $P_{gen}/P_{act} = 2$.

harvesting. The T term would be the period of time over which the analysis is considered. For extended operation, the harvested energy would need to be greater than the consumed energy, thus:

$$P_{gen} \times D_{gen} \times \eta_{storage} \times T > [P_{act} D_{act} + P_{low}(1 - D_{act})] \times T. \tag{3.21}$$

This expression can be solved for the ratio of the generated power to the power consumed in active mode.

$$\frac{P_{gen}}{P_{act}} > \frac{\left[D_{act} + \frac{P_{low}}{P_{act}}(1 - D_{act})\right]}{D_{gen} \times \eta_{storage}} \tag{3.22}$$

We see here that the ratio of generated power to active circuit power consumption depends on the duty cycles of operation and generation, as well as the ratio between the low and active power modes of the circuit. As previously discussed, this power ratio for the microcontrollers in table 3.3 is on the order of 10^{-3}. With this estimate, we can investigate the ratio of generated power to active mode power as shown in figure 3.10. The results of this figure give a way to

estimate the amount of power that needs to be generated relative to the power consumption of the bio-logger device. Using the earlier pigeon example, where the harvester power was 375 μW and the active mode power consumption of the MSP430FR5X was 180 μW, the ratio of generated power to active power would be approximately two. Based on this and the assumption that the device would be in active mode for 30-60 s/day, we can see in figure 3.10 that the harvester would need to be in operation for less than 1.4 minutes per day. This example case is shown with arrows in figure 3.10. Although we do not have an exact report on the daily activity levels of pigeons, it seems safe to assume that they fly on average for more than one minute a day. This estimate shows that piezoelectric energy harvesters can be a viable option for energy production on flying birds, given limited activity levels.

3.4.2 Energy budget for an example bio-logging system

In order to further explore the viability of vibrational energy harvesters as a power source for wildlife bio-loggers, we will show here the operational requirements necessary to maintain a positive daily energy budget for an example system. This example system will be a bio-logging device that takes one sensor measurement per minute for 12 hours a day, and wirelessly downloads the data at the end of each day. We will assume that each measurement requires 1 byte of memory and requires 10 ms to acquire. Table 3.4 contains the parameter assumptions for the example data logger explored here.

Based on the assumed power consumption and rate of sampling and transmission, we can develop an estimate of the daily energy requirements with the

Table 3.4: Example bio-logger system parameters

Parameter	Variable Name	Assumed Value	Units
Power when sensing	P_{act}	300 μA @ 3 V	mW
Power when time-keeping	P_{low}	1 μA @ 3 V	mW
Power when transmitting	P_{tx}	20 mA @ 3V	mW
Measurements per day	N_m	720	#/day
Time per measurement	t_m	10	ms/measurement
Transmissions per day	N_{tx}	1	#/day
Transmission rate	R_{tx}	250	k bits/s
Data size/measurement	D	1	bytes/measurement

following equation:

$$E_{out} = P_{act}t_{act} + P_{tx}t_{tx} + P_{low}t_{low} \tag{3.23}$$

Here t_* represents the time per day that the system is in either active/sensing, transmission, or low/time-keeping mode, as define by:

$$t_{act} = t_{\mathrm{m}}N_m \tag{3.24}$$

$$t_{tx} = R_{tx}^{-1}N_m D \tag{3.25}$$

$$t_{low} = t_{\mathrm{day}} - (t_{act} + t_{tx}) \tag{3.26}$$

Where t_{day} is one day (86400 s). Substituting these into equation 3.23 and rearranging gives

$$E_{out} = \left[(P_{act} - P_{low})\, t_{\mathrm{m}} + (P_{tx} - P_{low})\, R_{tx}^{-1} D\right] N_m + P_{low} t_{\mathrm{day}}. \tag{3.27}$$

We can compare this energy expenditure to the stored energy from the harvester, E_h:

$$E_h = P_{gen}t_{gen}\eta_{storage} \tag{3.28}$$

where t_{gen} is the amount of time per day that the harvester is generating power. Given this and equation 3.27, we can develop an estimate of the amount of active flapping time required by a bird to maintain a positive daily energy budget.

$$t_{gen} > \frac{\left[\left(P_{act} - P_{low}\right) t_{\mathrm{m}} + \left(P_{tx} - P_{low}\right) R_{tx}^{-1} D\right] N_m + P_{low} t_{\mathrm{day}}}{P_{gen} \eta_{storage}} \tag{3.29}$$

With this expression and the assumptions made in table 3.4, we can estimate the daily activity requirements to maintain positive energy budget for this example system. This calculation was carried out for a variety of species with known masses and flapping frequencies [57], as shown in table 3.5. Equation 3.29 depends on the amount of power that will be generated by each bird in flight (P_{gen}). We can use figure 3.3 to make this estimate, equating the harvester power (P_h) to generated power(P_{gen}), but we will need to know the specific power of the piezoelectric transducer used for each of the birds under consideration. The result presented in figure 3.9, can be used to estimate the specific power ($\bar{P}$) of a tuned harvester sized to approximately 4% of the mass of the bird. This specific power estimate (using a factor of safety of four) has been made for each of the birds in the dataset, and the result presented in table 3.5. With these specific power estimates and knowledge of the mass of the birds, we can use figure 3.3 to estimate the amount of safely harvestable power. This too is presented in table 3.5. With these estimates of harvestable power, we are able to use equation 3.29 to determine the amount of flapping activity required to maintain a positive energy budget. The results of this calculation are presented in table 3.5 and figure 3.11. We assume a storage efficiency ($\eta_{storage}$) of unity based on the high efficiencies of capacitors and rechargeable lithium-ion batteries [53].

In figure 3.11 we can see that generally, the minimum amount of flapping activity time required for a positive energy budget scales with the mass of the bird. As the bird mass decreases, more active time is required per day. Although

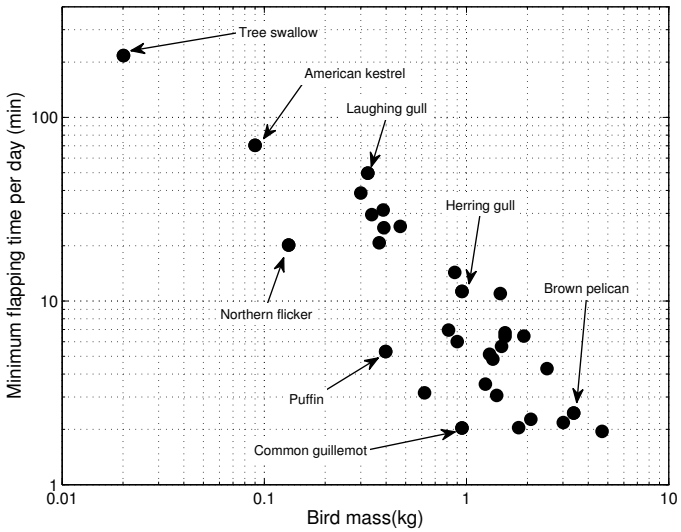

Figure 3.11: Minimum flapping time required by vibrational energy to power example bio-logger for various species

smaller birds tend to have higher flapping frequencies [63], which would tend to increase power output, figure 3.11 shows reductions in power from their smaller size dominates this increase. Although smaller birds to tend to require more activity, the requirements are still well within what would be considered reasonable. The smallest bird considered in this data set was the tree swallow (*Tachycineta bicolor*). Given this example system, this bird would need to be active (flapping) for approximately 3.6 hours per day. This required flapping time decreases quickly with increases in bird mass. For example, the American kestrel (*Falco sparverius*) would need 70 minutes of flapping and a great black-backed gull (*Larus marinus*) would require only 7 minutes. Even for this relatively capable system, with daily downlinking of data, the activity requirements of the host animals suggest that piezoelectric harvesting is a very viable option.

Table 3.5: Power generation estimates for a variety of birds. Mass and frequency data from [57].

Common Name	Latin Name	Mass (kg)	Frequency (Hz)	$\bar{P}$ (mW/kg)	P_h (mW)	Minimum t_{act} (min)
Puffin	*Fratercula arctica*	0.398	9.18	53	0.84	5
Common guillemot	*Uria aalge*	0.95	8.69	58	2.19	2
Razorbill	*Alca torda*	0.62	9.08	57	1.41	3
Great skua	*Catharacta skua*	1.35	3.93	17	0.92	5
Arctic skua	*Stercorarius parasiticus*	0.39	3.61	11	0.18	25
Kittiwake	*Rissa tridactyla*	0.387	3.18	9	0.14	31
Great black-backed gull	*Larus marinus*	1.55	2.90	11	0.66	7
Herring gull	*Larus argentatus*	0.95	3.05	10	0.39	11
Laughing gull	*Larus atricilla*	0.325	2.74	7	0.09	50
Royal tern	*Sterna maxima*	0.47	3.12	9	0.17	25
Black skimmer	*Rynchops niger*	0.3	3.36	10	0.12	39
Fulmar	*Fulmarus glacialis*	0.815	4.58	20	0.64	7
White-tailed tropicbird	*Phaethon lepturus*	0.37	4.22	15	0.21	21
Northern gannet	*Sula bassanus*	3.01	3.53	17	2.04	2
Anhinga	*Anhinga anhinga*	1.24	5.07	25	1.26	4
Double-crested cormorant	*Phalacrocorax auritus*	1.41	5.03	26	1.45	3
Shag	*Phalacrocorax aristotelis*	1.81	5.35	30	2.18	2
Brown pelican	*Pelecanus occidentalis*	3.39	3.01	13	1.81	2
Magnificent frigatebird	*Fregata magnificens*	1.47	2.24	7	0.41	11
Roseate spoonbill	*Ajaia ajaja*	1.3	3.90	17	0.87	5
White ibis	*Eudocimus albus*	0.9	4.65	21	0.74	6
Great white heron	*Ardea occidentalis*	2.5	2.68	10	1.04	4
Great blue heron	*Ardea herodias*	1.92	2.55	9	0.69	6
Great egret	*Casmerodius albus*	0.874	2.79	9	0.31	14
Little blue heron	*Egretta caerulea*	0.34	3.63	11	0.15	30
Turkey vulture	*Cathartes aura*	1.55	2.99	11	0.69	6
Black vulture	*Coragyps atratus*	2.08	4.53	24	1.96	2
Bald eagle	*Haliaeetus leucocephalus*	4.68	2.72	12	2.28	2
American kestrel	*Falco sparverius*	0.09	5.70	18	0.06	70
Osprey	*Pandion haliaetus*	1.49	3.31	13	0.79	6
Northern flicker	*Colaptes auratus*	0.132	9.19	42	0.22	20
Tree swallow	*Tachycineta bicolor*	0.0201	8.72	26	0.02	217

3.5 Conclusion

With recent reductions in the power consumption of microelectronic components and the advent of piezoelectric vibrational energy harvesting, electrical systems powered using ambient vibrations are now a reality. Although there are various applications for such systems, we have shown in this paper that the use of vibrational energy harvesting in the realm of wildlife computing is not only possible, but appears to be an advantageous method of energy production in applications involving some birds. We have shown that not only is there theoretically enough power available from most bird species to power a bio-logging device, but that there is a transduction method capable of harness-

ing that energy. The need for standard piezoelectric devices to be operated at a specific resonant frequency appears to be matched well to the accelerations expected for bird flight. Additionally, even given the mass limitations for any system mounted to a bird, piezoelectric devices could be designed to harvest a significant amount of power. We have shown that even when the harvester power is reduced by a factor of safety of four, there would still be sufficient power produced by piezoelectric devices to warrant their use. Furthermore, when operated under typical duty cycles, a piezoelectric harvester paired with a modern microcontroller could operate with positive average energy budgets with modest activity requirements for its host. This evidence suggests that vibrational energy harvesting should be considered as a potential power source for future avian bio-logging devices.

CHAPTER 4

TESTING OF VIBRATIONAL ENERGY HARVESTING ON FLYING BIRDS [1]

4.1 Introduction

The direct study of animals in their natural environment through observation can be challenging or impossible for many species. "Bio-logging" devices are systems mounted to an animal that are used to record data about the host or its environment without the need for direct observations by a human [51]. Owing their names to "biology" and "data-logging," these devices can drastically increase the amount of data available to scientists interested in animals and their habitats. Modern bio-logging devices are often composed of a suite of sensors run by a microcontroller, and typically powered by a battery. Fundamentally, the science that can be conducted directly depends on the power budget of the system, and thus is limited by battery technology. In this work we consider how vibrational energy harvesting could be used to supplement the power budget of bio-logging devices. Specifically, we focus on a device developed to conduct tests of piezoelectric energy harvesters on flying rock pigeons (*Columba livia*) and show that a significant amount of power can be harvested in flight from these birds. We also show that these devices have minimal impact on the flight accelerations of the birds.

Animal-based data collection found early applications in depth recording devices placed on a harpooned fin whale (*Balaenoptera physalus*) in the 1930's [73]

[1] Portions of this chapter were originally published in the proceedings of the 2013 ASME-SMASIS conference [78]. Reproduced here with permission.

and Weddell seals (*Leptonychotes weddellii*) in the 1960's [36]. Radio-based devices were seen as early as the 1950's for tracking woodchucks (*Marmota monax*) [40]. In the time since their initial deployment, bio-logging devices have seen drastic improvements in capabilities, both in terms of the number of sensors, and in the resolution and frequency of measurements [37][69]. In large part, these increases in capabilities have been a result of reductions in the power consumption of modern microelectronic components. Modern systems are capable of measuring anything from position to acoustics, but are still fundamentally limited by the amount of energy stored in their batteries [33][13]. If power could be generated throughout the life of the tag, smaller (or no) batteries could be used and more energy-intensive sensors could be deployed.

Vibrational energy harvesting on living animals has been demonstrated previously on moths (*Manduca sexta*) and green june beetles (*Cotinis nitida*) [67] [6]. Additionally, we have previously shown that there is a significant amount of power available for harvest from the flight of the majority of birds, even after accounting for the power required to carry the system [77]. In this work we review the testing conducted to measure the harvested power on a flying bird, and describe in detail the device developed to measure the harvester power and acceleration on the birds in flight. We also present some typical results from the more than 120 trials we have conducted, and then show through processing of the flight accelerations that there appears to be negligible effects on the bird's flight.

4.2 Methods

To address the feasibility of harvesting vibrational energy on flying birds, we had two primary objectives in testing: (1) Measure the power harvested by a piezoelectric device in flight. (2) Understand the effects of a dynamics mass on the flight of a bird. While it is known that birds can generally carry up to 2-4% of their body mass without considerable effects on long-term survivability, these numbers are based on a static mass[50][86][30][27]. In order to determine if piezoelectric energy harvesting is viable on a flying bird, we must determine if a vibrating system would adversely affect a bird's flight capabilities. To measure any effect, we developed a system that was able to measure the accelerations of the bird in flight, while carrying a piezoelectric beam that could be remotely locked down or allowed to vibrate. This allowed for a series of tests with and without a vibrating element on the back of the bird.

The test was designed to measure any effect of the vibrating system and consisted of flying a bird back and forth between two perches in a room while measuring the acceleration and harvested power. The test began by attaching a small energy harvester and data acquisition system (DAQ) to the back of one of three rock pigeons (*Columba livia*). These pigeons were given the designations B28729 (m = 433 g), B6 (m = 589 g), and BW (m = 361 g) which will be used throughout this paper to distinguish between the subjects. After turning on the on-bird DAQ, each pigeon was then placed in a room with only two perches spaced 22 ft. apart, between which they had previously been trained to fly. The energy harvester was then locked down, so as not to vibrate and the bird was prompted to fly from one perch to the other. The bird was then prompted to fly back to the original perch. Remotely, the energy harvesting beam was

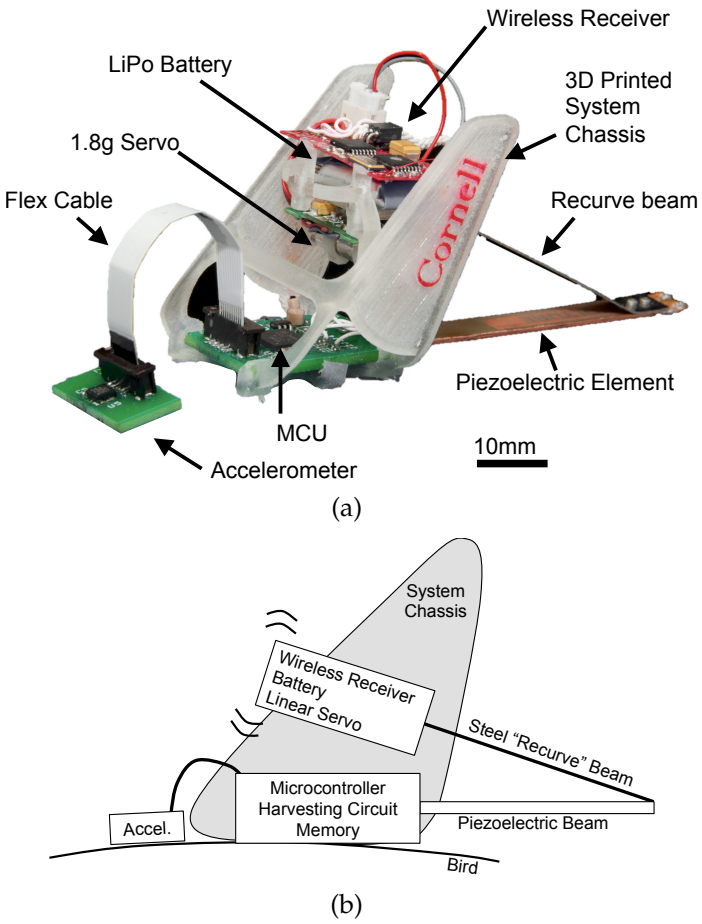

Figure 4.1: (a) Photo of testing system with critical components labeled. (b) Diagram of testing system showing layout of components.

then released and allowed to vibrate. The bird was prompted to fly back and forth between the perches again. This process of flying between perches and locking/releasing the harvester device was then repeated multiple times.

The device that was attached to the bird consisted of three integrated subsystems: the piezoelectric energy harvester device, the data-logging system, and the beam locking system. These systems worked together during the test to allow for the collection of the necessary data and can be seen in figure 4.1. In this figure we can see both a photo and a notional diagram of the system assembly. The piezoelectric energy harvester device can be seen as two beam elements in

this figure, forming a 'V' shape. The reasons for this design are explained below. The data-logging system consisted of a printed circuit board populated with a microcontroller, accelerometer, and memory unit. The tip mass assembly of the beam contained a battery and the two components necessary to lock and unlock the beam: a wireless receiver and a linear servo motor which interacted with the system chassis to lock the beam. The majority of the assembly was surrounded by a 3D printed chassis, that provided physical protection for the system, aided in the locking of the harvester assembly, and provided a location to tie the system to the bird. A Rappole-style [65] leg loop harness was used in this testing for the main assembly, while the accelerometer board was glued to trimmed feathers on the bird's back. The entire system can be seen mounted to one of the pigeons in figure 4.2. Each of these subsystems required significant design and development detailed in the following sections.

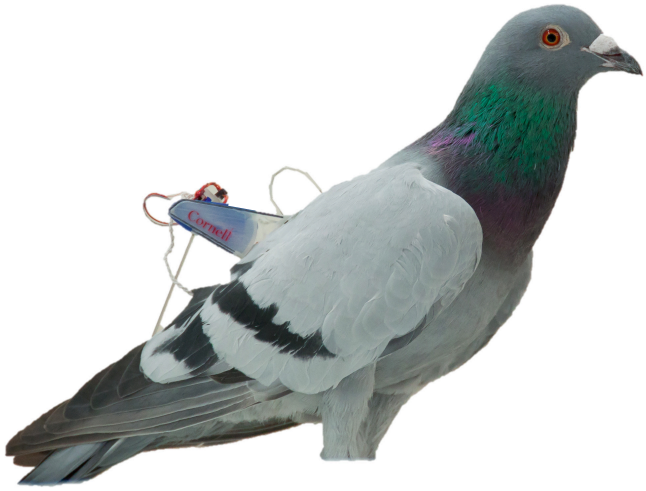

Figure 4.2: System mounted to back of pigeon

4.2.1 Piezoelectric energy harvester

The piezoelectric energy harvester beam consisted of a modified Midé Volture V22BL and an attached recurved stainless steel beam, as shown in figure 4.3(a). This "recurve" piezoelectric beam configuration is different from the typical simple cantilevered configuration and was originally developed for a similar application on flying moths [67]. It is critical that these devices be matched to the excitation frequency for maximum power harvesting. In order to use COTS piezoelectric beam elements, while matching a low excitation frequency of approximately 9 Hz [85] and maintaining a restrictive mass budget, a longer beam must be employed. The recurve configuration effectively increases the length of the beam, which allows for reductions in the resonant frequency of the system for a given mass. Additionally, the configuration allows for changes in the resonances based on the thickness of the recurve section of stainless steel. This makes the system easily reconfigurable to different excitation frequencies. The other reason for the use of a recurve configuration is that it reduces the moment loads at the root of the harvester, as shown in figure 4.3(b). A typical cantilevered beam would have highest moments at the root of the beam. This moment would act as a pitching torque on the bird in flight. Assuming the mass of the beam is small compared to the mass at the tip of the beam, the moments applied at the root of a recurved beam would be zero as shown in figure 4.3(b).

The design of such an energy harvester system for use on a bird requires consideration of the system mass and the excitation frequency target. Using the assumption that the Midé Volture V22BL beam is uniform across its length, we can predict the entire energy harvesting system natural frequency based on an estimate of the beam stiffness of each section of the recurve system. Using

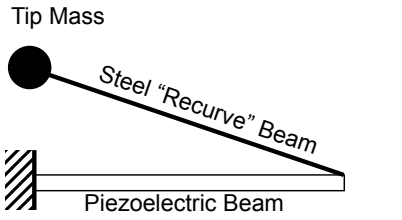

(a)

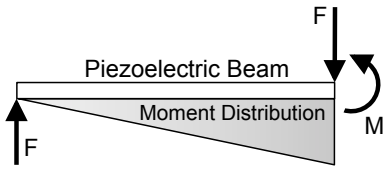

(b)

Figure 4.3: (a) Diagram of recurve beam diagram to reduce base moments and decrease natural frequency (b) Approximate free body and moment diagram of piezoelectric beam section of recurve assembly when under load. Notice area of highest bending moment at right side of beam.

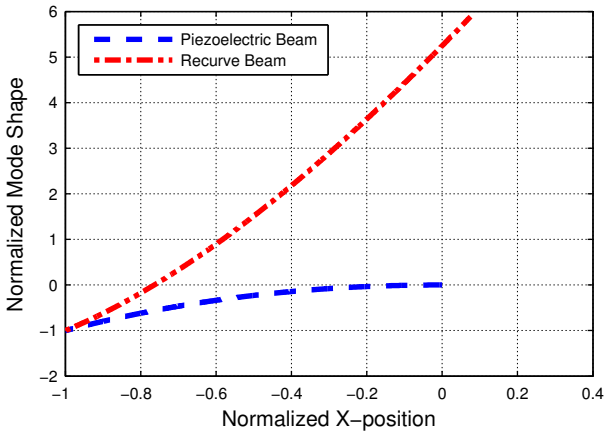

(a)

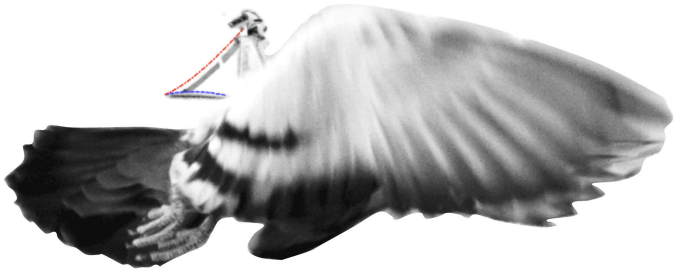

(b)

Figure 4.4: (a) Plot of modeshape of recurve piezoelectric energy harvester. Blue line dashed is piezoelectric beam. Red line dash-dot is stainless steel beam. (b) Modeshape overlaid on beam deflecting in flight.

a laser vibrometer, the natural frequency of a Midé Volture V22BL beam with no tip mass, clamped at 57.8 mm, and with shorted piezoelectric elements was found on average to be 148.3 Hz. Using this, and an estimate of the mass per unit length (12.7 g/cm), we were able to estimate the modulus times the moment of intertia, EI from the following approximation for fundamental frequency of a beam [10]:

$$f = \frac{1.875^2}{2\pi L^2}\left(\frac{EI}{m/L}\right)^{1/2} \tag{4.1}$$

Solving this expression for EI gives 9.9 mN-m^2. Knowledge of both this EI parameter and the mass per unit length of the piezoelectric beam allows us to determine the first natural frequency and mode shape of the resulting system. To design this system we used an estimate of the sum of the masses of the components used as the tip mass (4.9 g). Additionally, the EI and mass per unit length parameters for the recurved steel beam section could be calculated directly from the beam's dimension (57x6.2x0.254 mm). The resulting short circuit natural frequency for the entire recurve piezoelectric energy harvester beam would be 8.5 Hz, which is near the expected flapping frequency for the pigeons we tested. The mode shape for such a system can be seen in figure 4.4(a), with the piezoelectric portion of the beam plotted in blue and the stainless steel portion plotted in red. This mode shape can be seen to be excited in figure 4.4(b), where the modes shape plot has been scaled and overlaid on a photo of one of the birds in flight.

The charge developed by the piezoelectric energy harvesting beam during the flight of the bird was dissipated over a matched-load resistance. The optimal load resistance for an unrectified low-coupling piezoelectric energy harvester at

resonance can be calculated from the following expression [25]:

$$R_{opt} = \frac{1}{C_0 \omega} \tag{4.2}$$

Here C_0 is the capacitance of the piezoelectric device and ω is the excitation frequency. The capacitance of a Midé V22BL beam with its two piezoelectric elements connected in parallel is 18 nF [49]. We targeted a frequency of 8.5 Hz based on previous measurements of similarly sized birds [85] and the calculated natural frequency of the recurve beam assembly. The resulting optimal load resistance would thus be 1.05 MΩ. The optimality of this load resistance was validated in benchtop testing of the system. The resistance used in the final circuit was close to ideal and was 1.110 MΩ.

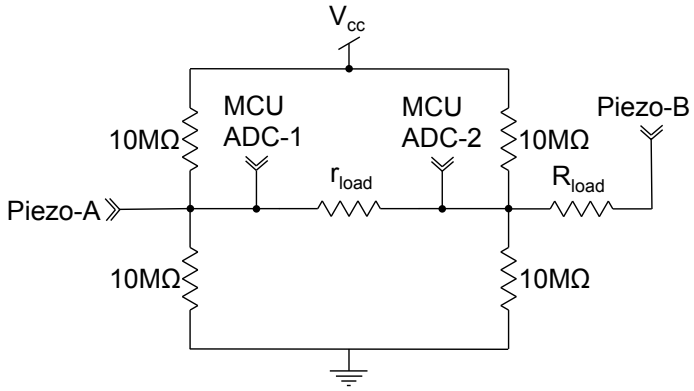

Figure 4.5: Circuit used to read voltage from the piezoelectric energy harvester. Voltage divider reduces voltage magnitude to level acceptable to microcontroller and 10MΩ resistors bias voltage.

The voltage developed by these types of piezoelectric devices are routinely on the order 20-50 V, and are thus too high for direct measurements by the microcontroller used by the DAQ system developed for this test. For this reason the circuit shown in figure 4.5 was used to measure the power dissipated by the load resistance across the piezoelectric elements. The circuit consisted of a voltage divider to reduce the measured voltage to a value within range of the

analog-to-digital converter on the microcontroller. Additionally, the measured voltage was biased to half of Vcc in order to account for the AC nature of the piezoelectric signal.

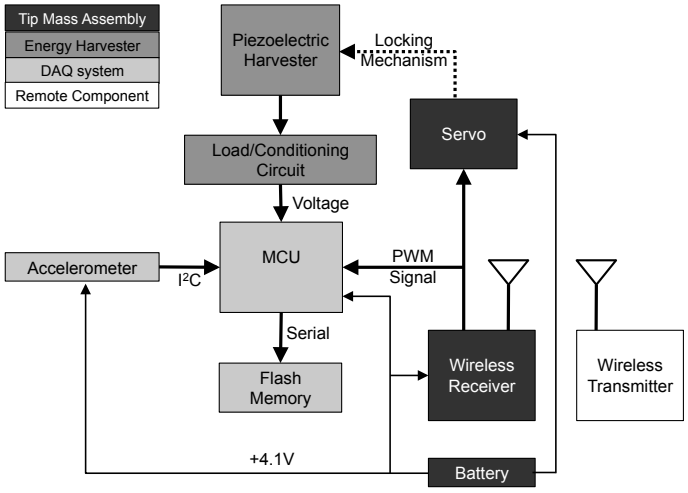

Figure 4.6: Block diagram of mini-DAQ and piezoelectric harvester. Elements in grey were installed as the tip mass of the piezoelectric beam.

4.2.2 Miniature data acquisition system

The device that monitored the power harvested by the piezoelectric device and the acceleration of the bird was a miniature data acquisition system design specifically for these tests. As seen in the system block diagram of figure 4.6, this subsystem was centered around an MSP430F2274 microcontroller unit. The microcontroller was programmed to take three measurements at 100 Hz and record the results to a 4 MByte AT25DF-321A flash memory unit from Atmel. The three measurements that were recorded were the voltage developed over the piezoelectric load resistance, the three axes of acceleration from the Bosch BMA150 accelerometer, and the pulse width modulated (PWM) voltage signal sent to the servo from servo controller of the wireless receiver.

The PWM signal was sent from the wireless receiver to the linear servo and controlled the locking and unlocking of the piezoelectric device. By taking these three measurements, we were able to correlate the accelerations of the bird in flight to the harvested power with confirmation that the harvester was either locked or unlocked for each trial. The PWM signal for the servo control had a typical pulse duration of approximately 1.5 ms, which was below the resolution of the sample rate of 100Hz. To account for this, the PWM signal was monitored by a timer with edge detection reset, which measured the duration of each pulse. For each recorded datapoint, the MCU logged the most recent pulse duration measured by the timer.

The physical configuration of this system consisted of a printed circuit board that hosted microcontroller and memory modules. This board also served as the physical mount location for the piezoelectric beam. The accelerometer was mounted to a remote board as shown in figure 4.1 and connected to the main board with a flexible ribbon cable. This was done to isolate any vibrations from the piezoelectric beam from the measurements being taken by the accelerometer. The power, ground, and PWM connections between the locking assembly on the tip of the beam and the main PCB were made by way of a braided bundle of flexible 36 AWG silicone coated multi-strand wires.

4.2.3 Energy harvester locking mechanism

The locking mechanism used in this system to arrest the motion of the harvester during flight was integrated as part of the tip mass of the recurve beam 4.7. The locking device consisted of a battery (Plantraco FR-30 bare cell lithium

polymer, 1 g), a wireless receiver (Plantraco Micro9-S-4CH, 1.1g), and a linear servo motor (Spektrum SPMSA2005, 1.8g). A chassis for mounting this hardware was printed using a Objet Connex500 3D printer using Fullcure720 resin. The operation of the mechanism was initiated by operating one of the controls of the wireless transmitter paired to the wireless receiver. When signaled, the receiver would change the duty cycle of the PWM signal sent to the linear servo mechanism. The servo in response would change position, moving the pushrod (shown in figure 4.7) in or out. When the rod was moved out it would contact the system chassis shown in figure 4.1(a). The force applied to the pushrod by the servo would then wedge the tip mass assembly between the vertical "wings" of the system chassis, effectively locking the tip mass assembly in place.

The general operation of the DAQ system, the energy harvester, and the locking tip mass assembly can be seen in a typical testing result (figure 4.8): the bird flying when the tip mass was locked had similar z-accelerations but essentially no voltage was developed by the piezoelectric system until the tip-mass was unlocked at about 145 s into this run. In the two flight after this, considerable voltage was produced.

4.3 Testing Results

In total, there were 136 flights for the three birds. Pigeon B6 flew six flights with the harvester locked and eight flights with the system unlocked; Pigeon B28729 flew 33 locked flights and 30 unlocked flights; and pigeon BW flew 30 locked flights and 29 unlocked flights. The final assembled mass of the system was 11.9 g, and thus represented 2.7%, 2.0%, and 3.3% of the mass of B2729, B6, and BW,

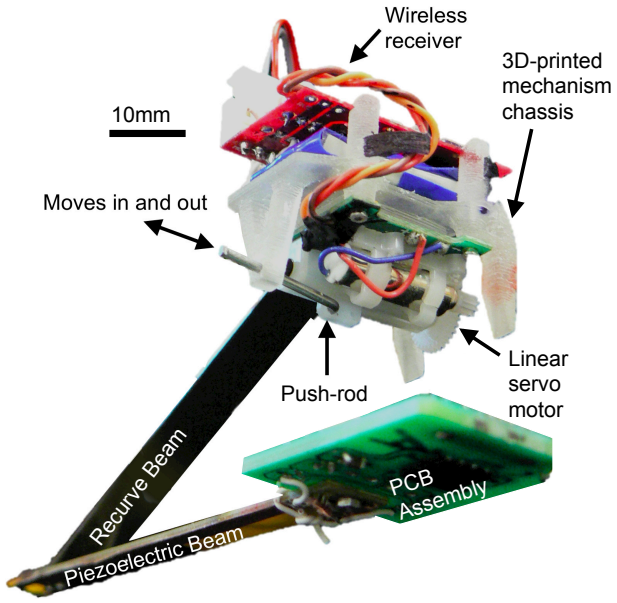

Figure 4.7: Photo of system without system chassis and accelerometer shown to highlight locking mechanism.

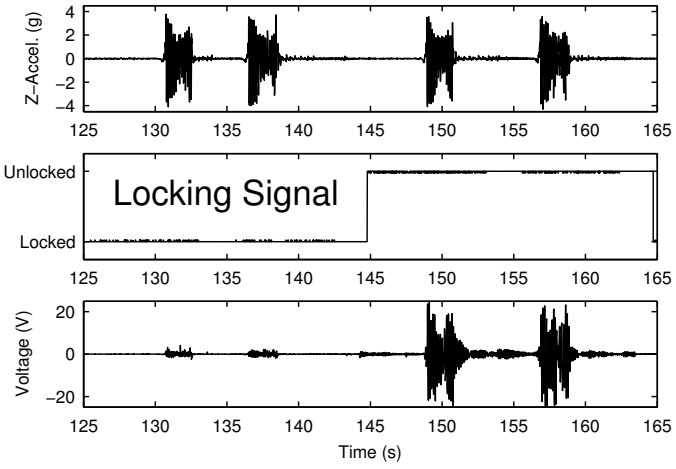

Figure 4.8: Acceleration, locking signal, and harvester voltage vs. time showing near zero harvester voltage when locked down despite motion of bird.

respectively. Thus, for all the birds tested, the assembly was at or below the 3-5% payload limit [50][86][30][27].

While there was some variability between flights and between birds, the general trend in both acceleration and harvested power was hour glass in shape, with high values at the beginning and end of the flights and lower values in the middle. An example of the acceleration profile that was recorded for one of the unlocked system flights can be seen in figure 4.9. In this figure, three graphs are shown, one for each component of acceleration using a coordinate system fixed to the bird. The x-direction was in the forward direction of flight, the y-direction was toward the bird's left wing, and the z-direction pointed up off of the bird's back. The data presented here has been high-pass filtered to remove the DC component of acceleration related to gravity. In this plot we see the highest accelerations at the beginning and end of the flight when the bird is taking off and landing. The acceleration peaks in the z-direction were nearly 4 g's, and 3 g's in the x-direction. This shows that while an energy harvesting beam could be mounted in the z-direction to harvest energy from the x-component of acceleration, the z-direction has higher acceleration magnitudes and would produce more power. Furthermore, this orientation would produce less drag on the bird than a beam mounted in the z-direction. In this figure we see very little acceleration in the y-direction. This is to be expected as the birds were flying in straight lines between perches. The mean fundamental frequency for this flight was 7.5 Hz, which while less than the targeted 8.5 Hz for the energy harvesting system, was close enough to harvest considerable energy.

The voltage, instantaneous power, and sliding windowed RMS power developed by the piezoelectric energy harvester over the flight shown in figure 4.9

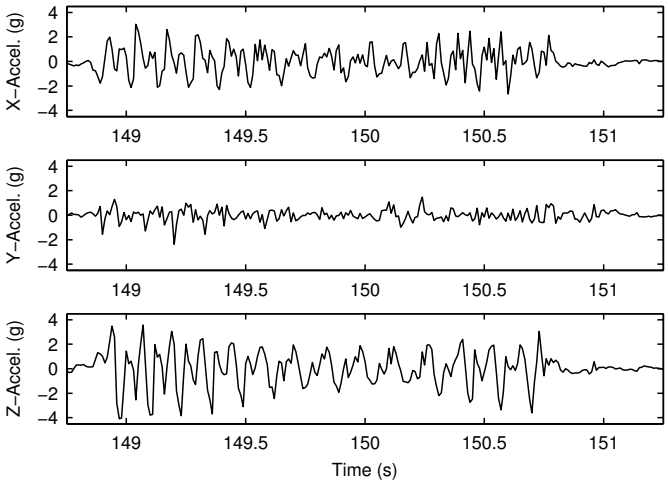

Figure 4.9: Plots of three acceleration components for typical flight.

can be seen in figure 4.10. In the first graph of this figure we see a voltage developed by the piezoelectric device matching the z-component acceleration profile, with high initial and final amplitudes. The voltage amplitude varied between approximately 9 and 25 V for this trial and was similar in other trials. The instantaneous power developed over the 1.11 MΩ load resistance can be seen in the second graph of figure 4.10. In this plot, we see instantaneous power peaks reaching as high as 0.72 mW during the landing and closer to 0.2 mW during the central portion of the flight. Overlaid on the instantaneous power plot, is a sliding window RMS result. The window size used was 0.66 s, representing approximately 5 flapping cycles. This result gives a better estimate of what the harvester would produce if the signal were rectified and used to power a circuit or charge a battery. We can see in this graph that the RMS power varies between 0.075 mW and 0.22 mW.

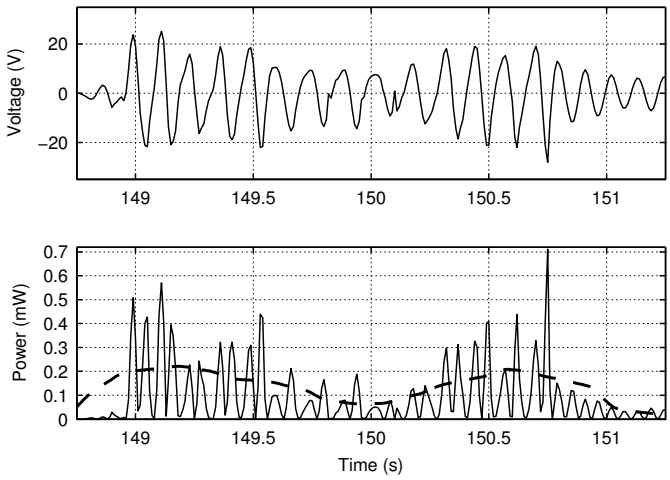

Figure 4.10: Plot of voltage over load resistance, power dissipated by load resistance, and RMS of dissipated power. RMS calculation uses a 0.66 s sliding window.

4.3.1 RMS power output

The sliding-window RMS power analysis was conducted for each flight with the harvester was unlocked and the results averaged for each of the three birds. These results (figure 4.11) all show higher power output of the system at the beginning and ending of the flights, with less power produced in the middle. Additionally, we see that the flights were fairly repeatable, with small standard deviations for B6 and BW, and slightly higher for B28729. The important result from figure 4.11 is that the average RMS harvested power ranged from 0.1 mW to 0.3 mW. These RMS power results represent a good estimate of what could be delivered to a circuit using this piezoelectric harvester as a power source.

4.3.2 Harvester effects on acceleration

Before advocating the use of these energy harvesters on flying birds, it is critical that we understand what, if any, effect they have on the flight of the animal. The

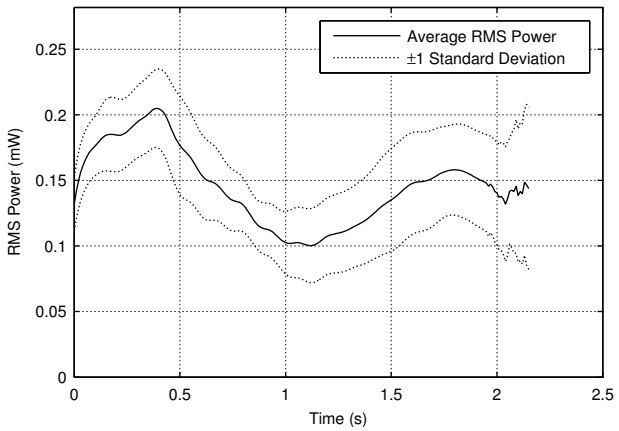

(a)

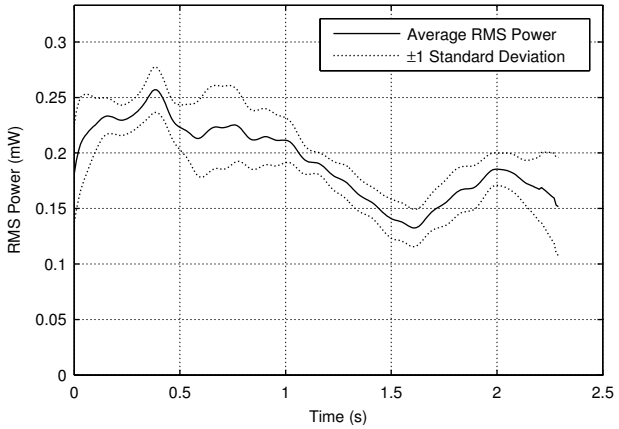

(b)

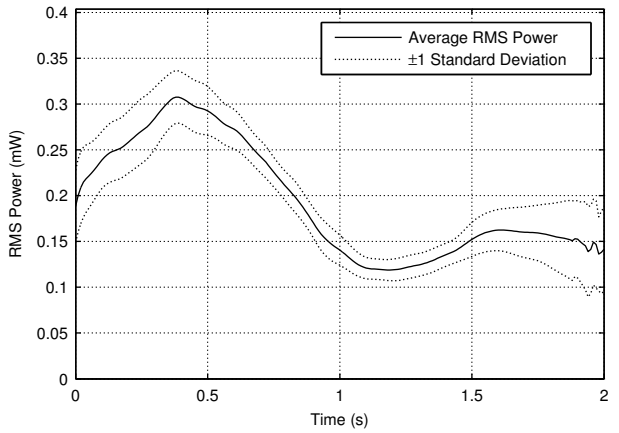

(c)

Figure 4.11: Sliding window RMS power output for B28729 (a), B6 (b), and BW (c)

acceleration measurements give us a way to quantitatively measure the changes in the motion of the bird in flight. Because these trials capture transient flight of take off, level flight, and landing, it is important that we have a way of investigating temporal shifts in flight acceleration, as well as any changes in the frequency domain. The short flight durations in combination with the sampling frequency (100 Hz) made sliding window FFT analysis (spectrograms) impractical because of reductions in the frequency resolution. In order to investigate the spectral and time-domain changes between flights where the system was locked and unlocked, we conducted two analyses. The first used polynomial curve fits to envelope the highest peaks of acceleration in time. This analysis is used to understand if the time history of the acceleration amplitude differed between the locked and unlocked flights. The second analysis used Fourier analysis to investigate the frequency domain of the locked and unlocked trials to see if particular frequencies show significant shifts in amplitude or phase.

Acceleration enveloping functions

To determine if there were significant changes in the acceleration magnitude envelope between the locked and unlocked trials, we fit polynomial curves to the peaks in the acceleration profiles. Statistical comparisons of the coefficients that defined these polynomial fits could then be made in order to determine if any changes were statistically significant. To do this, an algorithm was needed that would be able to select the highest magnitude positive and negative acceleration peaks for each flapping cycle, such as those of the z-acceleration profile of figure 4.9. In order to select these highest magnitude points, and not intermediate peaks, the data was lowpass filtered with a 10 Hz cutoff frequency. The deriva-

tive of the filtered data was then checked for zero crossings. The time stamps of these zero crossings were then used to find the peaks in the original waveform. Finally, acceleration magnitudes less than 1 g were removed to eliminate small peaks at the beginning and end of the samples. The resulting selected peaks for all trials of BW (dots in figure 4.12) show considerable consistency in the flapping periods. Although from trial to trial there is some variation in amplitude, each peak aligns almost perfectly in time for the majority of the flight. Toward the end of the flight there is more variation in the timing of each wing flap, but for this bird the periods appear consistent between trials up to approximately 1.5 s.

After selecting the acceleration magnitudes, fifth-order polynomials were fitted to the data, one for the positive peaks and one for the negative peaks, to provide a means of direct comparison between trials. (figure 4.12). The six coefficients of these fifth-order polynomials for each trial provided a way of statistically comparing the time histories. Two-tailed, two-sample t-tests were conducted for each set of coefficients, assuming unequal variances, and with an α-value of 0.1. This was done for both the positive and negative peak profiles. For example, if the polynomials took on the form $a_{mag}(t) = At^5 + Bt^4 + Ct^3 + Dt^2 + Et + F$, then all the A coefficients for the positive profiles of all the unlocked trials would be compared against the A coefficients of the positive profiles for all the locked trials. This was done for each of the coefficients $A - F$, for both the positive and negative acceleration profiles, and for each bird. The results showed very little statistically significant difference between the compared profiles for each bird. The only statistically different locked and unlock profile set was for the negative peaks for B28729. The resulting p-values from the hypothesis tests can be seen in table 4.1. In this table we

see relatively high p-values for the majority of the coefficients, indicating a that for most cases, the null hypothesis cannot be rejected and any differences in the coefficients may be simply caused by chance.

Table 4.1: Hypothesis test results for the acceleration envelope polynomial fits. A value of 1 indicates the rejection of the null hypotheses, meaning coefficients for the unlocked and locked cases are statistical unequal.

		B28729		B6		BW	
	Coefficient	Reject Null?	p-value	Reject Null?	p-value	Reject Null?	p-value
Positive Envelope	A	0	0.8988	0	0.1894	0	0.7245
	B	0	0.9974	0	0.1738	0	0.8111
	C	0	0.8512	0	0.1802	0	0.9269
	D	0	0.6422	0	0.2181	0	0.9424
	E	0	0.4163	0	0.3049	0	0.8645
	F	0	0.276	0	0.4231	0	0.9114
Negative Envelope	A	1	0.0387	0	0.1816	0	0.3931
	B	1	0.0409	0	0.1434	0	0.4348
	C	1	0.0464	0	0.1265	0	0.5006
	D	1	0.0532	0	0.1337	0	0.5973
	E	1	0.0505	0	0.1734	0	0.7334
	F	1	0.0389	0	0.2545	0	0.8495

The enveloping profiles for each of the birds (Figures 4.13 (a)-(c)) showed very few, if any, differences between locked and unlocked trials. Furthermore, we can see that even in the case where there were statistically significant differences between the locked and unlock profile polynomial coefficients (negative curve for B28729, figure 4.13(a)), these differences manifest themselves as very small differences between the actual curves.

Fourier analysis comparisons

The effects of the dynamic vibrational energy harvester on the flight of the bird was further investigated using a discrete Fourier transform (DFT). Using the locked flight trials as the control, we compared the spectra of the unlocked trials in an attempt to find significant changes in magnitude or phase. The frequency resolution of the results depended on the sample rate and the number of points

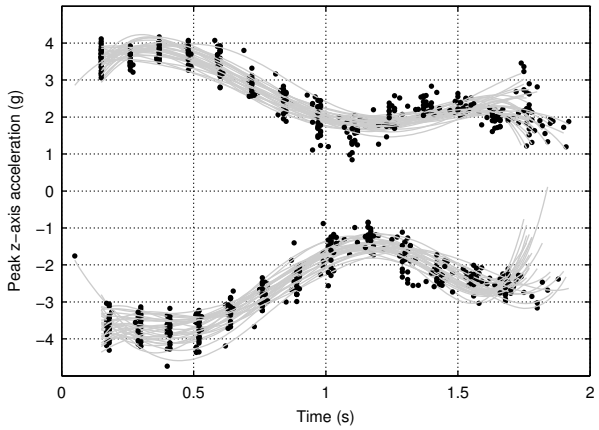

Figure 4.12: Example envelopes of acceleration magnitude for all unlocked trials of BW. Selected peaks shown as black dots. Polynomial curve fits shown as gray lines.

in the sample. At a sample rate of 100 Hz and typical flight time of 2 s, the frequency resolution of the Fourier analysis was near 0.5 Hz. A tapered cosine (Tukey) window was applied to each trial with the tapering occurring on the first and last 5% of the trial data.

After performing the DFT for each trial, for each bird, the locked magnitudes and phase results were compared to the locked cases at each frequency. For example, the dataset of the magnitudes of the locked trials of BW at 7 Hz was compared with the unlocked magnitude results for that frequency. Two tailed t-tests with $\alpha = 0.1$ were performed on these two data sets to determine if there was significant difference. This α value is higher than the typical 0.05, as we would like to reduce the probability of a false negative (type-II error). This hypothesis testing was repeated for all frequency magnitudes up to 50 Hz (Nyquist), and for phase as well.

The mean DFT amplitude results for the locked and unlocked case for each bird can be seen in figure 4.14. In this figure, the mean of the locked cases is plotted with a solid line, while the mean of the unlocked cases is plotted with

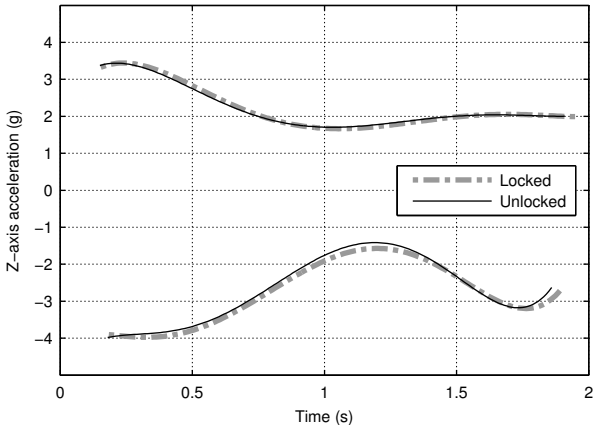

(a)

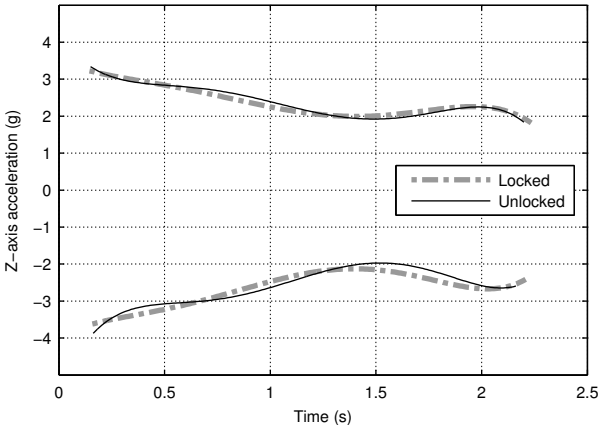

(b)

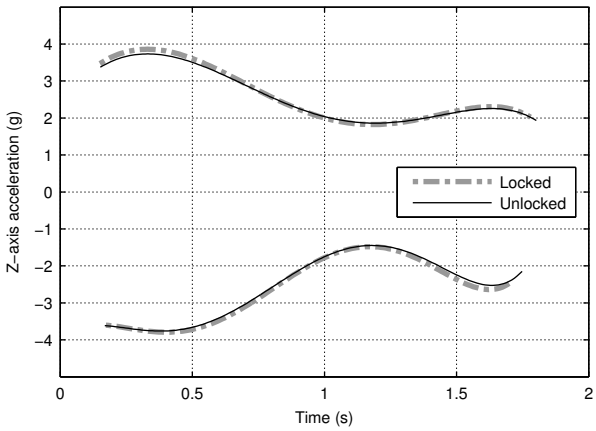

(c)

Figure 4.13: Average locked and unlocked case acceleration envelope polynomial fits for B28279 (a), B6 (b), and BW (c)

a dotted line. The area between these two lines is filled to show any areas of significant difference. Additionally plotted in these figures are a series of vertical gray bands. These bands highlight which frequencies show a statistically significant difference between the locked and unlocked trials. A similar set of plots for phase is shown in figure 4.15.

The magnitude results shown in figure 4.14 indicate that relatively little changed in the z-acceleration spectrum between the locked and unlocked trials. We do not see wide bands of significance at either of the first two harmonics. Figure 4.14(a) shows some difference at 8 and 9 Hz, but these changes appear relatively small. Similarly, figure 4.14(c) shows some slight changes on either side of the fundamental frequency, but the changes do not deviate largely from the locked cases. More bands of rejection of the null hypothesis are seen above the second harmonic in all three cases but the amplitudes in these regions are so small, these changes are not likely to have significant effects on the flight of the bird.

The phase results shown in figure 4.15 are similar to those of the magnitude in that there are not wide bands of phase changes in either of the first two harmonics. We do see in 4.15(a) and 4.15(c) that there appears to be a statistically significant phase shift within the band of the fundamental frequency, but in neither case is this associated with a significant change in the magnitude results at the same frequency.

The second harmonic for both B28729 and B6 show increases in the amplitude, although occurring with sufficient variance as to not allow for rejection of the null hypothesis. These results may suggests some slight effect on the flapping gait that could be illuminated through further testing. Despite this ob-

servation, neither the magnitude, nor phase result suggest a significant change in the z-acceleration profile. The relative paucity of significant differences between the locked and unlocked trials would grow small if any correction for multiple comparisons were made.

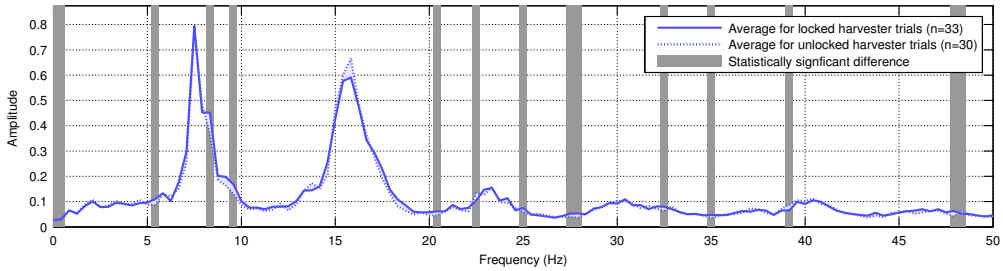

(a) Mean DFT magnitude results for B28729

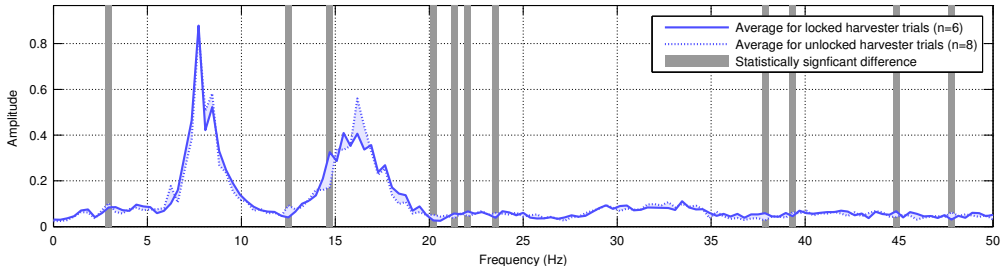

(b) Mean DFT magnitude results for B6

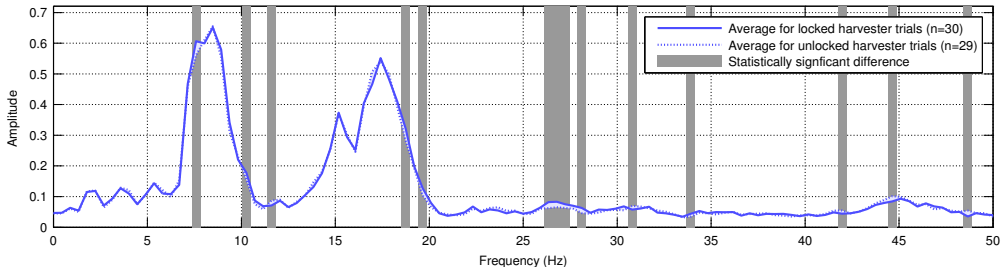

(c) Mean DFT magnitude results for BW

Figure 4.14: Mean DFT magnitude result for locked and unlocked cases. Both results are plotted and the space between the two curves is filled. Frequencies with statistically significant ($p < 0.1$) mean differences are banded in gray.

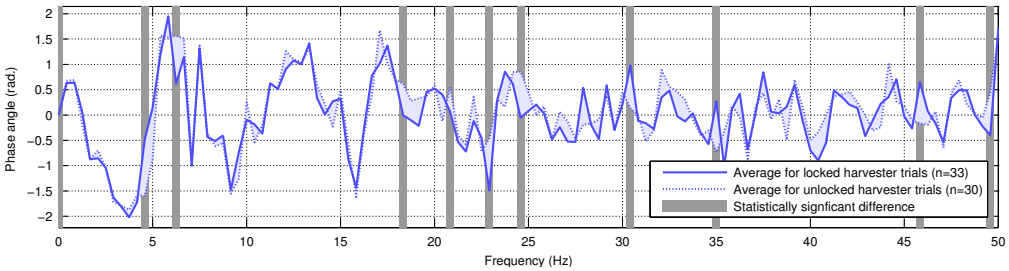

(a) Mean DFT phase results for B28729

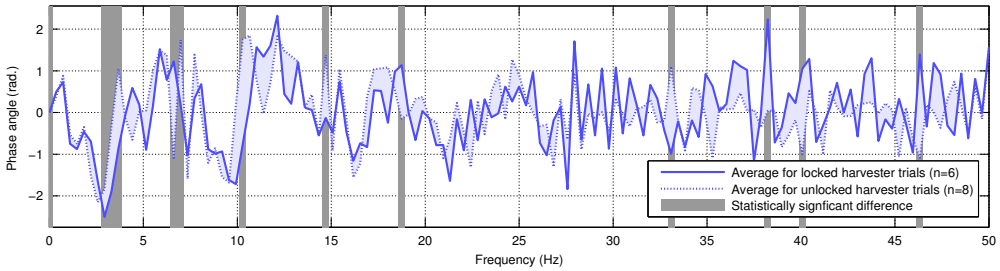

(b) Mean DFT phase results for B6

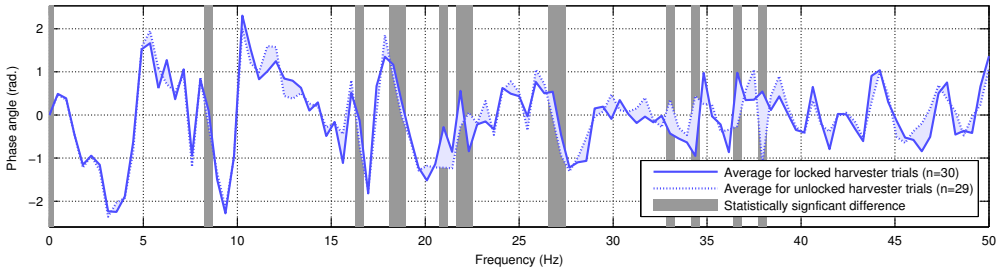

(c) Mean DFT phase results for BW

Figure 4.15: Mean DFT phase result for lock and unlock cases. Both results are plotted and the space between is filled. Frequencies with statistically significant ($p < 0.10$) differences are banded in gray.

4.4 Conclusions

This work has demonstrated the feasibility of harvesting energy using piezoelectric devices on flying birds. We have developed a system that is capable of harvesting the energy generated in the piezoelectric device and is capable of measuring the accelerations of the birds in flight at the same time. We have shown that a significant amount of power can be generated in flight, and that

this power can be harvested without significant effects on the acceleration of the bird. While we were able to measure statistically significant differences in the z-accelerations of the birds in flight, these differences were small and would disappear under any correct for multiple comparisons. It seems safe to conclude that our device in unlocked oscillating mode did not negatively affect the acceleration amplitude profiles or the fundamental flapping frequencies of flying pigeons.

The RMS power that was developed in flight was on the order of 0.1-0.3 mW. This amount of power is significant considering that the piezoelectric element was not optimized for this application(i.e., the device's fundamental frequency was not precisely tuned and the physical dimensions were not optimized), yet the amount of power produced would be sufficient to power a microcontroller. The piezoelectric element employed was fabricated from an off-the-shelf component. These devices are not optimized for power production at these frequencies, and we could expect more power if a piezoelectric device were optimized and fabricated specifically for the mass and frequency targets of the bird of choice. Other work has shown that the piezoelectric material thickness and aspect ratio of these harvesters are critical design considerations when developing systems for fixed mass, frequency, and excitation acceleration constraints [74] [76]. Despite this fact, the amount of power harvested would still be capable of powering a microcontroller-based circuit.

There are a significant number of microcontrollers on the market, but many contain features not necessary for a bio-logging device. Table 4.2 provides basic power requirements of some low-power devices that could be used on an avian bio-logger. In this table, we see that the power consumption of these devices is

Table 4.2: Power consumption for example microcontroller devices

Manufacturer	Model	Power@1MHz (mW)
Texas Instruments	MSP430F2XX	0.44
	MSP430FR5X	0.18
Atmel Corporation	ATtinyX4A	0.38
	ATtinyX61/V	0.54
	ATmega165	0.39

on the order of tenths of milliwatts. When comparing these power requirements with the 0.1-0.3 mW produced by the piezoelectric energy harvester, it becomes apparent that these energy harvesters are a viable power source. Furthermore, these bio-logging devices are typically duty cycle managed, spending only a short portion of the day in active mode. For reference the low-power "sleep" mode of the microcontrollers listed in table 4.2 is on average 190 nW, or approximately three orders of magnitude less than what was produced in testing. This further shows that there is sufficient power produced by these piezoelectric energy harvesters to warrant their use on bio-logging devices.

APPENDIX A

AVIAN POWER MODEL

Table A.1: Power types and equations for bird flight [59]

Power Type	Description	Equation
Parasitic (P_{par})	Drag from body	$1/2\rho V^3 S_b C_{Db}$
Induced (P_{ind})	Momentum transfer to air (lift)	$\frac{km^2g^2}{2S_d V\rho}$
Profile (P_{pro})	Driving wings forward through flow	$\frac{C_{pro}}{A_R}\frac{1.05k^{3/4}m^{3/2}g^{3/2}S_b^{1/4}C_{Db}^{1/4}}{\rho^{1/2}B^{3/2}}$
Basal Metabolic (P_M)	Caloric overhead	$\eta\alpha m^{\delta}$
Cardio/pulmonary	Cardiovascular/Breathing	$0.1(P_{par}+P_{ind}+P_{pro}+P_M)$

Table A.2: Bird flight power model nomenclature and constants [59] [60]

Name	Variable	Constants
Wing aspect ratio	A_R	
Wingspan	B	
Profile power constant-empirical	C_{pro}	8.4
Body drag coefficient	C_{Db}	0.1
Harvester specific power	$\bar{P}$	
Maximum harvestable power	P_H	
Harvestable power	P_h	
Induced power	P_{ind}	
Laden power output	P_l	
Metabolic power output	P_M	
Parasitic drag power	P_{par}	
Profile power	P_{pro}	
Body frontal area	S_b	$8.13\times10^{-3}m^{0.666}$
Circular area swept by wings	S_d	
Forward flight velocity	V	
Acceleration due to gravity	g	
Induced drag factor-empirical	k	0.9
Mass of bird (unladen)	m	
Mass of the payload (other the energy harvester)	m_e	
Payload mass (other than energy harvester)	m_p	
Allowable fraction of laden mass (3-4%)	q	
Metabolic mass constant	α	6.25 for passerines 3.79 for non-passerines
Metabolic Conversion efficiency	η	
Metabolic mass exponent	δ	0.724 for passerines 0.723 for non-passerines
Air density	ρ	

APPENDIX B

QUARTIC SOLUTION VARIABLES

The solution to the quartic polynomial

$$Ax^4 + Bx^3 + Cx^2 + Dx + E = 0 \tag{B.1}$$

has the following solution

$$x = \frac{-B}{4A} + \frac{\pm_i W \mp_j \sqrt{-(3\lambda + 2y \pm_i \frac{2\beta}{W})}}{2} \tag{B.2}$$

where

$$\begin{aligned}
\lambda &= \frac{-3B^2}{8A^2} + \frac{C}{A} \\
\beta &= \frac{B^3}{8A^3} - \frac{BC}{2A^2} + \frac{D}{A} \\
\gamma &= \frac{-3B^4}{256A^4} + \frac{CB^2}{16A^3} - \frac{BD}{4A^2} + \frac{E}{A} \\
P &= \frac{-\lambda^2}{12} - \gamma \\
Q &= \frac{-\lambda^3}{108} + \frac{\lambda\gamma}{3} - \frac{\beta^2}{8} \\
R &= \frac{-Q}{2} + \sqrt{Q^2/4 + P^3/27} \\
U &= R^{1/3} \\
y &= \begin{cases} -\frac{5}{6}\lambda - Q^{1/3} & \text{if } U = 0 \\ -\frac{5}{6}\lambda + U - \frac{P}{3U} & \text{if } U \neq 0 \end{cases} \\
W &= \sqrt{\lambda + 2y}
\end{aligned}$$

BIBLIOGRAPHY

[1] Standards of piezoelectric crystals, 1949. *Proceedings of the IRE*, 37(12):1378–1395, December 1949.

[2] Physical and piezoelectric properties of apc materials. Technical report, APC International, Ltd., `http://www.americanpiezo.com/apc-materials/piezoelectric-properties.html`, 2012.

[3] Piezoceramic materials and properties. Technical report, Piezo Systems, Inc., `http://www.piezo.com/prodmaterialprop.html`, 2012.

[4] Piezoelectric ceramics catalog. Technical report, Channel Industries Inc., `http://www.channelindustries.com/_includes/chan_cat.pdf`, 2012.

[5] B. C. Abbott, B. Bigland, and J. M. Ritchie. The physiological cost of negative work. *The Journal of physiology*, 117(3):380–390, 1952.

[6] E. E. Aktakka, H. Kim, and K. Najafi. Energy scavenging from insect flight. *J. Micromech. Microeng.*, 21(095016), 2011.

[7] S. Anton and H. A. Sodano. A review of power harvesting using piezoelectric materials (2003–2006). *Smart Mater. Struct.*, 16, 2007.

[8] O Aura and PV Komi. Mechanical efficiency of pure positive and pure negative work with special reference to the work intensity. *International journal of sports medicine*, 7(01):44–49, 1986.

[9] F. P. Beer, E. R. Johnston Jr., and J. T. DeWolf. *Mechanics of Material*. McGraw Hill, 3rd edition, 2002.

[10] R. D. Blevins. *Formulas for Natural Frequency and Mode Shape*. Krieger Publishing Company, 1979.

[11] J. Borgeson. Ultra-low-power pioneers: Ti slashes total mcu power by 50 percent with new "wolverine" mcu platform. White paper, Texas Instruments, Post Office Box 655303, Dallas, Texas 75265, 2012.

[12] J. Brufau-Penella and M. Puig-Vidal. Piezoelectric energy harvesting improvement with complex conjugate impedance matching. *J. Intel. Mat. Syst. Str.*, 20:597–608, March 2009.

[13] W. C. Burgess, P. L. Tyack, B. J. Le Boeuf, and D. P. Costa. A programmable acoustic recording tag and first results from free-ranging northern elephant seals. *Deep-Sea Res. Pt. II*, 45(7):1327–1351, 1998.

[14] J. Cho, M. Anderson, R. Richards, D. Bahr, and C Richards. Optimization of electromechanical coupling for a thin-film pzt membrane: I. modeling. *J. Micromech. Microeng.*, 15:1797–1803, 2005.

[15] Cornell Lab of Ornithology. All about birds. http://www.allaboutbirds.org/Page.aspx?pid=1189, 2011. [Online; various search results].

[16] C. T. M. Davies and C. Baknes. Negative (eccentric) work. ii. physiological responses to walking uphill and downhill on a motor-driven treadmill. *Ergonomics*, 15(2):121–131, 1972.

[17] J. M. Dietl and E. Garcia. Beam shape optimization for power harvesting. *J. Intel. Mat. Syst. Str.*, 21(5):633–646, April 2010.

[18] A. Donoso and O. Sigmund. Optimization of piezoelectric bimorph actuators with active damping for static and dynamic loads. *Struct. Multidiscip. O.*, 38:171–183, 2009.

[19] A. Erturk and D. J. Inman. A distributed parameter electromechanical model for cantilevered piezoelectric energy harvesters. *J. Vib. Acoust.*, 130(4):041002–1 through 041002–15, August 2008.

[20] A. Erturk and D. J. Inman. An experimentally validated bimorph cantilever model for piezoelectric energy harvesting from base excitations. *Smart Mater. Struct.*, 18, January 2009.

[21] A. Erturk and D.J. Inman. Issues in mathematical modeling of piezoelectric energy harvesters. *Smart Mater. Struct.*, 17(6):065016 (14pp), 2008.

[22] J. Feenstra, J. Granstrom, and H. Sodano. Energy harvesting through a backpack employing a mechanically amplified piezoelectric stack. *Mech. Syst. Signal Pr.*, 22(3):742–734, April 2008.

[23] R. Fu and T.Y. Zhang. Influences of temperature and electric field on the bending strength of lead zirconate titanate ceramics. *Acta Mater.*, 48:1729–1740, 2000.

[24] A. R. Gerson and C. G. Guglielmo. Flight at low ambient humidity increases protein catabolism in migratory birds. *Science*, 333(6048):1434–1436, 2011.

[25] D. Guyomar, A. Badel, E. Lefeuvre, and C. Richard. Toward energy harvesting using active materials and conversion improvement by nonlinear processing. *IEEE T. Ultrason. Ferr.*, 52(4):584–595, April 2005.

[26] N. W. Hagood, W. H. Chung, and A. von Flotow. Modelling of piezoelectric actuator dynamics for active structural control. *J. Intel. Mat. Syst. Str.*, 1:327–354, July 1990.

[27] R. S. Hedin and D. F. Caccamise. A method for selecting transmitter weights based on energetic cost of flight. In *Trans. of the NE Fish and Wildlife Conf.*, volume 39, page 115, 1982.

[28] T. L. Hedrick, B. W. Tobalske, and A. A. Biewener. How cockatiels (nymphicus hollandicus) modulate pectoralis power output across flight speeds. *J. Exp. Biol.*, 206:1363–1378, 2003.

[29] A. V. Hill. Production and absorption of work by muscle. *Science*, 131(3404):897–903, 1960.

[30] D. A. Hill and P. A. Robertson. The role of radio-telemetry in the study of galliformes. *World Pheasant Assoc. J.*, 12:81–92, 1987.

[31] D. J. Inman. *Engineering Vibration*. Pearson Prentice Hall, Upper Saddle River, New Jersey, 07458, third edition, 2008.

[32] M. P. Johnson and P. L. Tyack. A digital acoustic recording tag for measuring the response of wild marine mammals to sound. *IEEE J. Oceanic Eng.*, 28:3–12, January 2003.

[33] P. Jouventin and H. Weimerskirch. Satellite tracking of wandering albatrosses. *Nature*, 343:746–748, 1990.

[34] N. Kong, D.S. Ha, A. Erturk, and D.J. Inman. Resistive impedance matching circuit for piezoelectric energy harvesting. *J. Intel. Mat. Syst. Str.*, 21:1293–1302, September 2010.

[35] N. Konow, E. Azizi, and T. J. Roberts. Muscle power attenuation by ten-

don during energy dissipation. *Proceedings of the Royal Society B: Biological Sciences*, 279(1731):1108–1113, 2012.

[36] G. L. Kooyman. Techniques used in measuring diving capacities of weddell seals. *The Polar Record*, 12(79):391–394, 1965.

[37] G. L. Kooyman. Genesis and evolution of bio-logging devices: 1963–2002. *Mem. Natl. Inst. Polar. Res.*, 58:15–22, 2004.

[38] R. Kornbluh, R. Pelrine, Q. Pei, R. Heydt, S. Stanford, S. Oh, and J. Eckerle. Electroelastomers: Applications of dielectric elastomer transducers for actuation, generation and smart structures. In *SPIE's 9th Annual International Symposium on Smart Structures and Materials*, pages 254–270. International Society for Optics and Photonics, 2002.

[39] E. Lefeuvre, A. Badel, C. Richard, and D. Guyomar. Piezoelectric energy harvesting device optimization by synchronous electric charge extraction. *J. Intel. Mat. Syst. Str.*, 16:865–876, October 2005.

[40] C. D. LeMunyan, W. White, E. Nyberg, and J. J. Christrian. Design of a miniature radio transmitter for use in animal studies. *J. Wildlife Manage.*, 23(1):107–110, January 1959.

[41] Y. Liao and H. A. Sodano. Structural effects and energy conversion efficiency of power harvesting. *J. Intel. Mat. Syst. Str.*, 20:505–514, March 2009.

[42] S. L. Lindstedt, P. C. LaStayo, and T. E. Reich. When active muscles lengthen: properties and consequences of eccentric contractions. *Physiology*, 16(6):256–261, 2001.

[43] J. A. Main, E. Garcia, and D. Howard. Optimal placement and sizing of paired piezoactuators in beams and plates. *Smart Mater. Struct.*, 3:373–381, 1994.

[44] H. Makino and N. Kamiya. Effects of dc electric field on mechanical properties of piezoelectric ceramics. *Jpn. J. Appl. Phys.*, 33(9B):5323–5327, September 1994.

[45] J. H. Marden. Maximum lift production during takeoff in flying animals. *J. Exp. Biol.*, 130:235–258, 1987.

[46] Microwave Telemetry Inc. *Battery Powered Argos/GPS LC4^{TM} PTT-100s*,

2013 (accessed May 8, 2013). http://www.microwavetelemetry.com/bird/batteryArgosGPS.cfm.

[47] Microwave Telemetry Inc. *Fish Tracking*, 2013 (accessed May 8, 2013). http://www.microwavetelemetry.com/fish/.

[48] Microwave Telemetry Inc. *PTT-100 5 gram Solar PTT*, 2013 (accessed May 8, 2013). http://www.microwavetelemetry.com/bird/solarPTT_5g.cfm.

[49] Midé. Volture piezoelectric energy harvesters datasheet, January 2013.

[50] B. Naef-Daenzer, F. Widmer, and M. Nuber. A test for effects of radio-tagging on survival and movements of small birds. *Avian Sci.*, 1(1):15–23, 2001.

[51] Y. Naito. New steps in bio-logging science. *Mem. Natl. Inst. Polar. Res.*, (58):50–57, 2004.

[52] H. H. Obrecht, C. J. Pennycuick, and M. R. Fuller. Wind tunnel experiments to assess the effect of back-mounted radio transmitters on bird body drag. *J. Exp. Biol.*, 135(1):265–273, 1988.

[53] T. Ohzuku, A. Ueda, N. Yamamoto, and Y. Iwakoshi. Factor affecting the capacity retention of lithium-ion cells. *Journal of power sources*, 54(1):99–102, 1995.

[54] D. R. Patton, D. W. Beaty, and R. H. Smith. Solar panels: An energy source for radio transmitters on wildlife. *J. Wildlife Manage.*, 37(2):236–238, April 1973.

[55] C. J. Pennycuick. Power requirements for horizontal flight in the pigeon, columba livia. *J. Exp. Biol.*, 49:527–555, 1968.

[56] C. J. Pennycuick. The mechanics of bird migration. *Ibis*, 111:525–556, 1969.

[57] C. J. Pennycuick. Predicting wingbeat frequency and wavelength of birds. *J. Exp. Biol.*, 150:171–185, 1990.

[58] C. J. Pennycuick. Actual and 'optimum' flight speeds - field data re-assessed. *J. Exp. Biol.*, 200:2355–2361, 1997.

[59] C. J. Pennycuick. *Modeling the Flying Bird*. Academic Press, 2008.

[60] C. J. Pennycuick, S. Åkesson, and A. Hedenström. Air speeds of migrating birds observed by ornithodolite and compared with predictions from flight theory. *J. R. Soc. Interface*, 10(86), 2013.

[61] C. J. Pennycuick, D. S. Farner, J. R. King, and K. C. Parkes. *Avian Biology: Mechanics of Flight*, volume 5. Academic Press, 1975.

[62] C. J. Pennycuick, H. H. Obrecht III, and M. R. Fuller. Empirical estimates of body drag of large waterfowl and raptors. *J. Exp. Biol.*, 135:253–264, October 1988.

[63] C. J. Pennycuick, M. Klaassen, A. Kvist, and A. Lindstrom. Wingbeat frequency and the body drag anomaly: Wind-tunnel observations on a thrush nightingale (luscinia luscinia) and a teal (anas crecca). *J. Exp. Biol.*, 199:2757–2765, September 1996.

[64] E. L. Poole. Weights and wing areas in north american birds. *Auk*, 55(3):511–517, July 1938.

[65] J. H. Rappole and A. R. Tipton. New harness design for attachment of radio transmitters to small passerines. *J. Field Ornithol.*, 62(3):335–337, 1991.

[66] J. M. V. Rayner. A new approach to animal flight mechanics. *J. Exp. Biol.*, 80(1):17–54, 1979.

[67] T. Reissman, R. B. MacCurdy, and E. Garcia. Electrical power generation from insect flight. In *SPIE Smart Structures and Materials+ Nondestructive Evaluation and Health Monitoring*, pages 797702–797702. International Society for Optics and Photonics, April 2011.

[68] M. Renaud, P. Fiorini, and C. van Hoof. Optimization of a piezoelectric unimorph for shock and impact energy harvesting. *Smart Mater. Struct.*, 16:1125–1135, 2007.

[69] Y. Ropert-Coudert and R. P. Wilson. Trends and perspectives in animal-attached remote sensing. *Front. Ecol. Environ.*, 3:437–444, 2005.

[70] S. Roundy. On the effectiveness of vibration-based energy harvesting. *J. Intel. Mat. Syst. Str.*, 16:809–823, October 2005.

[71] S. Roundy, P. K. Wright, and J. M. Rabaey. *Energy Scavenging for Wireless Sensor Networks*. Kluwer Academic Publishers, Norwll, MA, 2004.

[72] C. J. Rupp, A. Evgrafov, K. Maute, and M. L. Dunn. Design of piezoelectric energy harvesting systems: A topology optimization approach based on multilayer plates and shells. *J. Intel. Mat. Syst. Str.*, 20:1923–1939, November 2009.

[73] P. F. Scholander. *Experimental investigations on the respiratory function in diving mammals and birds*. Hvalradets skrifter, Scientific results of marine biological research; nr. 22. Oslo : I Kommisjon hos Jacob Dybwad, 1940.

[74] M. W. Shafer, M. Bryant, and E. Garcia. Designing maximum power output into piezoelectric energy harvesters. *Smart Mater. Struct.*, 21(8), 2012.

[75] M. W. Shafer, M. Bryant, and E. Garcia. A practical power maximization design guide for piezoelectric energy harvesters inspired by avian biologgers. In *Proc. ASME 2012 Conf. Smart Mater. Adap. Struct. Intel. Syst.*, number 8071. ASME, Sept. 19-21, Stone Mountain, GA 2012.

[76] M. W. Shafer and E. Garcia. The power and efficiency limits of piezoelectric energy harvesting. *J. Vib. Acoust.*, (in review).

[77] M. W. Shafer and E. Garcia. Maximum and practical sustainably harvestable vibrational power from avian subjects. In *Proc. ASME 2011 Conf. Smart Mater. Adap. Struct. Intel. Syst.*, number 54723, pages 353–359. ASME, 2011.

[78] M. W. Shafer, R. MacCurdy, and E. Garcia. Testing of vibrational energy harvesting on flying birds. In *Proc. ASME 2013 Conf. Smart Mater. Adap. Struct. Intel. Syst.*, number 3036. ASME, Sept. 16-18, Snowbird, UT 2013.

[79] M. W. Shafer, R. MacCurdy, E. Garcia, and D. Winkler. Harvestable vibrational energy from avian sources: theoretical predictions vs. measured values. In *SPIE Smart Struct. and Mater. and Nondestructive Eval. and Health Monitor.*, number 834103. International Society for Optics and Photonics, March 11-15 2012.

[80] N. S. Shenck and J. A. Paradiso. Energy scavenging with shoe-mounted piezoelectrics. *IEEE Micro*, 21(3):30 –42, 2001.

[81] Y. C. Shu and I. C. Lien. Analysis of power output for piezoelectric energy harvesting systems. *Smart Mater. Struct.*, 15:1499–1512, September 2006.

[82] Y. C. Shu and I. C. Lien. Efficiency of energy conversion for a piezoelectric power harvesting system. *J. Micromech. Microeng.*, 16:2429–2438, 2006.

[83] H. A. Sodano, G. Park, and D. J. Inman. Estimation of electric charge output for piezoelectric energy harvesting. *Strain*, 40:49–58, 2004.

[84] L. Tang, Y. Yang, and C. K. Soh. Toward broadband vibration-based energy harvesting. *J. Intel. Mat. Syst. Str.*, 21:1867–1897, December 2010.

[85] B. W. Tobalske, T. L. Hedrick, and A. A. Biewener. Wing kinematics of avian flight across speeds. *J. Avian Biol.*, 34:177–184, 2003.

[86] USGS. How to request auxiliary marking permission. http://www.pwrc.usgs.gov/bbl/manual/aarequs.cfm, 2011. [Online; accessed February 28, 2012].

[87] S. P. Vandenabeele, E. L. Shepard, A. Grogan, and R. P. Wilson. When three per cent may not be three per cent; device-equipped seabirds experience variable flight constraints. *Mar. Biol.*, 159(1):1–14, 2012.

[88] A. Wickenheiser. Design optimization of linear and non-linear cantilevered energy harvesters for broadband vibrations. *J. Intel. Mat. Syst. Str.*, 22:1213–1225, July 2011.

[89] A. Wickenheiser and E. Garcia. Power optimization of vibration energy harvesters utilizing passive and active circuits. *J. Intel. Mat. Syst. Str.*, 21:1343–1361, September 2010.

[90] Wildlife Computers. *Innovative Tags for Innovative Research*, 2013 (accessed May 8, 2013). `http://www.wildlifecomputers.com/default.aspx`.

[91] H. Yoon, G. Washington, and A. Danak. Modeling, optimization, and design of efficient initially curved piezoceramic unimorphs for energy harvesting application. *J. Intel. Mat. Syst. Str.*, 16:877–888, October 2005.